Ultra-Small Silver Nanoparticles - Dynamic Behavior in Aqueous and Biological Environments

Inaugural Dissertation

to obtain the academic degree

Doctor rerum naturalium (Dr. rer. nat.)

submitted to

the Department of Biology, Chemistry and Pharmacy

of Freie Universität Berlin

by

Claudia Kästner

from Ludwigsfelde

Berlin

2018

The research presented in this thesis was carried out under supervision of Andreas F. Thünemann between October 2014 and May 2018 at the Department of Materials Protection and Surface Technology of Bundesanstalt für Materialforschung und -prüfung (BAM).

1st Reviewer:	Dr. habil. Andreas F. Thünemann
	Bundesanstalt für Materialforschung und –prüfung (BAM)
2nd Reviewer:	Prof. Dr. Christina Roth
	Freie Universität Berlin
Date of Defense:	03.07.2018

Acknowledgements

Many people have supported me in the development of this work. Above all, I would like to express my deepest gratitude to Andreas F. Thünemann for his excellent supervision throughout my time as doctoral candidate. I thank him for encouraging me and guiding me through all of the challenges of a doctoral thesis. He has provided me with a high level of freedom and responsibility, while always taking time to offer helpful advice during our inspiring discussions. I am grateful for the trust he has placed in me from the start.

I would also like to express my gratitude to Christina Roth, who co-supervised this thesis. I would like to thank her not only for being my second reviewer, but also for the stimulating discussions and her helpful advice during the preparation of this dissertation.

I am deeply grateful to all my collaboration partners. Alfonso Lampen's group at the Bundesinstitut für Risikobewertung (BfR), and in particular Holger Sieg, Linda Böhmert, Dajana Lichtenstein, Albrecht Braeuning and Alfonso Lampen himself, were always willing to provide experiments and answer questions regarding biological purposes. This thesis greatly benefited from the interplay of our knowledge during our lively discussions.

I would like to express my gratitude to the whole Thünemann group. Without you and the exceptional environment of a productive and constructive atmosphere, I would not have had enjoyed this time as much as I did. Thank you for great discussions, lunch times and coffee breaks. In particular, I would like to acknowledge Brian R. Pauw, from whom I learned what a good presentation should really look like, and what it means to be enthusiastic about setting up a network for sharing scientific measuring devices. Additionally, I would like to thank Patrick E. J. Saloga for inspiring discussions on microwave reactions and helping me with my thesis as a master student. I gratefully acknowledge Petra Fengler for her wise advice regarding DLS measurements and our countless helpful discussions. Thank you for always being by my side with advice and support. I am also greatly indebted to Maximilian Ebisch for supporting me in so many experiments, and for untiredly reproducing my results over and over again. I also thank Dana Ziegel for always providing answers to the formal questions that occur in such an institution and for her unconventional solutions.

I would like to acknowledge my financial support from a Menschen-Ideen-Strukturen (MIS) project of the Bundesanstalt für Materialforschung und –prüfung, which provided me with the opportunity to visit national and international conferences.

Finally, I would like to express my gratitude to my friends and my family. The continual support from my parents enabled me to face all challenges. Thank you for all the years you have listened to me, even though it was always about chemistry. Thanks are due to all of my friends; in particular Julia Theuer, Vivien Osinski, Rebecca Hilt, Linda Leiendecker and Sophia Schneider, who always made me feel like I could achieve anything. I am greatly indebted to Hendrik V. Schröder, who has given me incredible empathy and support throughout the last six years. I am very grateful to have you in my life.

Abstract

The utilization of silver nanoparticles in consumer related products has significantly increased over the last decade, especially due to their antimicrobial properties. Today they are used in a plethora of products ranging from cosmetics and textiles to medical instruments. Thus, investigations on nanoscale silver are attracting increasing interest in many fields, such as biomedicine or catalysis. Unfortunately, the results of these studies are diverse and do not lead to a consistent evaluation of the toxicity of silver nanoparticles. A major flaw is the usage of non-uniform and inadequate characterized particles with broad size distributions.

To elucidate this problem this thesis deals with the synthesis and thorough characterization of a versatile silver nanoparticle system in a size at the lower end of the nanoscale. Poly(acrylic acid) (PAA)-stabilized silver nanoparticles with a nominal radius of 3 nm are synthesized using two methods. Firstly, they are produced in a classical batch synthesis and secondly in a microwave-assisted synthesis. The comparison of these two routes applying the same reaction conditions provides the opportunity to reveal whether non-thermal microwave effects, which are still under debate in literature, are present.

The synthesized particles exhibit a high stability and are used in an inter-laboratory comparison proving their suitability for application in nanometrology, such as determination of nanoparticle sizes, size distribution widths, and particle concentrations. Furthermore, the high versatility of the silver nanoparticle system enables an easy ligand exchange to tune the surface of the particles on demand and improve their biocompatibility. Exemplarily, transfunctionalizations with albumin, glutathione, and tyrosine are performed and characterized by small-angle X-ray scattering (SAXS), dynamic light scattering (DLS), UV/Vis and IR spectroscopy. These differently coated silver nanoparticles are used firstly in a catalytic application: the reduction of 4-nitrophenol. Therein, a dependence of the catalytic activity on the corresponding coating is observed and reveals that the PAA-stabilized silver nanoparticles exhibit an exceptionally high activity.

As a preliminary study for future biological applications the binding behavior, especially the adsorption and desorption, of biocompatible, fluorescent ligands is investigated.

It is demonstrated that a fluorescent labelling with appropriate binding properties can be provided, which is subsequently used in an initial investigation on lung and intestinal cells regarding particle transport.

Subsequently, the PAA-stabilized particles are employed in an artificial digestion. The monitoring of the size and size distribution throughout the three steps of digestion (saliva, stomach, intestine) shows that the silver nanoparticles pass the digestion under transformation in size, but still remain nano-sized. Since silver is known for the continuous release of silver ions, the digestion of silver nanoparticles leads naturally to the question of the behavior of ionic silver in an artificial digestion. The investigation of this topic with the help of small and wide-angle X-ray scattering and IR spectroscopy reveals that silver thiocyanate nanoparticles are formed during *in vitro* digestion.

The release of silver ions from the surface of silver nanoparticles is a crucial point in the risk assessment of silver nanoparticles, since the ions can undergo complex transformations in biological environments. In this work, enhanced ion release was observed for the interaction of PAA-stabilized silver nanoparticles with glutathione. New small silver clusters were formed during this process.

The diverse applications of the silver nanoparticle system in this work demonstrate the high versatility and stability of the system, which is a promising candidate for further comparable biological and catalytic applications.

Kurzfassung

Die Verwendung von Silbernanopartikeln in Konsumgütern des täglichen Lebens hat in den letzten zehn Jahren deutlich zugenommen, insbesondere aufgrund ihrer antimikrobiellen Eigenschaften. Heute werden sie in einer Vielzahl von Produkten eingesetzt, die von Kosmetika und Textilien bis hin zu medizinischen Instrumenten reichen. So stoßen Untersuchungen an Nanosilber in vielen Bereichen wie der Biomedizin oder der Katalyse auf zunehmendes Interesse. Leider sind die Ergebnisse dieser Studien divers und führen nicht zu einer konsistenten Bewertung der Toxizität von Silbernanopartikeln. Eine große Schwachstelle ist die Verwendung von uneinheitlichen und unzureichend charakterisierten Partikeln mit breiten Größenverteilungen.

Um dieses Problem zu beleuchten, beschäftigt sich diese Arbeit mit der Synthese und umfassenden Charakterisierung eines vielseitigen Silbernanopartikelsystems mit einer Größe am unteren Ende der Nanoskala. Poly(acrylsäure) (PAA)-stabilisierte Silbernanopartikel mit einem nominalen Radius von 3 nm werden mit zwei Methoden synthetisiert. Zum einen werden sie in einer klassischen Batch-Synthese und zum anderen in einer mikrowellengestützten Synthese hergestellt. Der Vergleich dieser beiden Verfahren bei gleichen Reaktionsbedingungen ermöglicht die Aufklärung, ob nicht-thermische Mikrowelleneffekte, die in der Literatur noch diskutiert werden, in diesem Fall vorhanden sind.

Die synthetisierten Partikel weisen eine hohe Stabilität auf und werden in einem Ringversuch eingesetzt, um ihre Eignung für den Einsatz in der Nanometrologie, wie zum Beispiel der Bestimmung von Nanopartikelgrößen, Größenverteilungsbreiten und Partikelkonzentrationen, nachzuweisen. Darüber hinaus ermöglicht die hohe Vielseitigkeit des Silbernanopartikelsystems einen einfachen Ligandenaustausch, um die Oberfläche der Partikel nach Bedarf anzupassen und ihre Biokompatibilität zu verbessern. Beispielhaft werden Umfunktionalisierungen mit Albumin, Glutathion und Tyrosin durchgeführt und durch Röntgenkleinwinkelstreuung (SAXS), dynamische Lichtstreuung (DLS), UV/Vis- und IR-Spektroskopie charakterisiert. Diese unterschiedlich beschichteten Silbernanopartikel

werden zunächst in einer katalytischen Anwendung eingesetzt: Der Reduktion von 4-Nitrophenol. Dabei wird die Abhängigkeit der katalytischen Aktivität von der entsprechenden Beschichtung beobachtet und es zeigt sich, dass die PAA-stabilisierten Silbernanopartikel eine außergewöhnlich hohe Aktivität aufweisen.

Als Vorbetrachtung für zukünftige Anwendungen der Silbernanopartikel in biologischen Fragestellungen wird das Bindungsverhalten, insbesondere die Adsorption und Desorption, von biokompatiblen, fluoreszierenden Liganden untersucht. Es zeigt sich, dass eine Fluoreszenzmarkierung mit geeigneter Bindungswirkung bereitgestellt werden kann. Die fluoreszenzmarkierten Partikel werden anschließend in einer ersten Untersuchung hinsichtlich des Partikeltransports auf Lungen- und Darmzellen eingesetzt.

Anschließend werden die PAA-stabilisierten Partikel in einem künstlichen Verdau untersucht. Die Verfolgung der Größe und Größenverteilung in den drei Verdaustufen (Speichel, Magen, Darm) zeigt, dass die Silbernanopartikel den Verdau unter Größenveränderungen passieren, aber dennoch nanoskalig bleiben. Da Silber für die kontinuierliche Freisetzung von Silberionen bekannt ist, führt der Verdau von Silbernanopartikeln zu der Frage nach dem Verhalten von ionischem Silber in einem künstlichen Verdau. Die Untersuchung dieses Themas mit Hilfe von Röntgenklein- und Röntgenweitwinkelstreuung, sowie IR-Spektroskopie zeigt, dass bei dem *in vitro* Verdau Silberthiocyanatnanopartikel entstehen.

Die Freisetzung von Silberionen von der Oberfläche von Silbernanopartikeln ist ein entscheidender Punkt bei der Risikobewertung von Silbernanopartikeln, da die Ionen in biologischen Umgebungen komplexe Transformationen durchlaufen können. In dieser Arbeit wurde eine erhöhte Ionenfreisetzung für die Interaktion von PAA-stabilisierten Silbernanopartikeln mit Glutathion beobachtet. Dabei entstanden neue kleine Silbercluster.

Die vielfältigen Anwendungen des Silbernanopartikelsystems in dieser Arbeit zeigen die hohe Vielseitigkeit und Stabilität des Systems, das ein vielversprechender Kandidat für weitere vergleichbare biologische und katalytische Anwendungen ist.

Publication List

Publications included in this thesis:

Claudia Kästner, Andreas F. Thünemann. **Catalytic Reduction of 4-Nitrophenol Using Silver Nanoparticles with Adjustable Activity.** *Langmuir* 2016, 32, 7383–7391, DOI: 10.1021/acs.langmuir.6b01477

Claudia Kästner, Dajana Lichtenstein, Alfonso Lampen, Andreas F. Thünemann. **Monitoring the fate of small silver nanoparticles during artificial digestion.** *Colloids and Surfaces A: Physicochemical and Engineering Aspects* 2017, 526, 76–81, DOI: 10.1016/j.colsurfa.2016.08.013

Brian R. Pauw, Claudia Kästner, Andreas F. Thünemann. **Nanoparticle size distribution quantification: results of a small-angle X-ray scattering inter-laboratory comparison.** *Journal of Applied Crystallography* 2017, 50, 1280–1288, DOI: 10.1107/S160057671701010X

Patrick E. J. Saloga, Claudia Kästner, Andreas F. Thünemann. **High-Speed but Not Magic: Microwave-Assisted Synthesis of Ultra-Small Silver Nanoparticles.** *Langmuir* 2018, 34, 147−153, DOI: 10.1021/acs.langmuir.7b01541

Claudia Kästner, Alfonso Lampen, Andreas F. Thünemann. **What happens to the silver ions? – Silver thiocyanate nanoparticle formation in an artificial digestion.** *Nanoscale* 2018, 10, 3650–3653, DOI: 10.1039/c7nr08851e

Claudia Kästner, Patrick Saloga, Andreas F. Thünemann. **Kinetic monitoring of glutathione-induced silver nanoparticle disintegration.** *Nanoscale* 2018, DOI: 10.1039/c8nr02369g (accepted on 07.05.2018)

Claudia Kästner, Linda Böhmert, Albert Braeuning, Alfonso Lampen, Andreas F. Thünemann. **Fate of Fluorescence Labels – Their Adsorption and Desorption Kinetics to Silver Nanoparticles.** *Langmuir* (in review, submitted on 20.04.2018)

Publications not included in this thesis:

Dajana Lichtenstein, Johanna Ebmeyer, Thomas Meyer, Anne-Cathrin Behr, Claudia Kästner, Linda Böhmert, Sabine Juling, Birgit Niemann, Christoph Fahrenson, Sören Selve, Andreas F. Thünemann, Jan Meijer, Irina Estrela-Lopis, Albert Braeuning, Alfonso Lampen. **It takes more than a coating to get nanoparticles through the intestinal barrier *in vitro*.** *European Journal of Pharmaceutics and Biopharmaceutics* 2017, 118, 21–29, DOI: 10.1016/j.ejpb.2016.12.004

Holger Sieg, Claudia Kästner, Benjamin Krause, Thomas Meyer, Agnès Burel, Linda Böhmert, Dajana Lichtenstein, Harald Jungnickel, Jutta Tentschert, Peter Laux, Albert Braeuning, Irina Estrela-Lopis, Fabienne Gauffre, Valérie Fessard, Jan Meijer, Andreas Luch, Andreas F. Thünemann, Alfonso Lampen. **Impact of an Artificial Digestion Procedure on Aluminum-Containing Nanomaterials.** *Langmuir* 2017, 33, 10726−10735, DOI: 10.1021/acs.langmuir.7b02729

Benjamin Krause, Thomas Meyer, Holger Sieg, Claudia Kästner, Philipp Reichardt, Jutta Tentschert, Harald Jungnickel, Irina Estrela-Lopis, Agnes Burel, Soizic Chevance, Fabienne Gauffre, Pégah Jalili, Jan Meijer, Linda Böhmert, Albert Braeuning, Andreas F. Thünemann, Valerie Fessard, Peter Laux, Alfonso Lampen, Andreas Luch. **Characterization of aluminum, aluminum oxide and titanium dioxide nanomaterials using a combination of methods for particle surface and size analysis.** *RSC Advances* 2018, 8, 14377–14388, DOI: 10.1039/c8ra00205c

Holger Sieg, Caroline Braeuning, Birgitta Maria Kunz, Claudia Kästner, Benjamin Krause, Thomas Meyer, Pégah Jalili, Kevin Hogeveen, Linda Böhmert, Dajana Lichtenstein, Agnès Burel, Soizic Chevance, Harald Jungnickel, Jutta Tentschert, Peter Laux, Albert Braeuning, Fabienne Gauffre, Valérie Fessard, Jan Meijer, Irina Estrela-Lopis, Andreas F. Thünemann, Andreas Luch, and Alfonso Lampen. **Uptake and molecular impact of aluminum-containing nanomaterials on intestinal human Caco-2 cells.** *Nanotoxicology* (in review, submitted on 01.05.2018)

Abbreviations

AAS	Atomic absorption spectroscopy
ANOVA	Analysis of variance
BSA	Bovine serum albumin
CDF	Cumulative differential function
CTAB	Cetyltrimethylammonium bromide
DLS	Dynamic light scattering
EDX	Energy dispersive X-ray spectroscopy
FITC	Fluorescein isothiocyanate
FTIR	Fourier-transform infrared spectroscopy
FWHM	Full width at half-maximum
GSH	Glutathione
ICP-MS	Inductively coupled plasma mass spectrometry
IFT	Indirect Fourier transformation
NP_{BSA}	Bovine serum albumin-stabilized-silver nanoparticles
NP_{GSH}	Glutathione-stabilized-silver nanoparticles
NP_{Hu}	Poly(acrylic acid) stabilized-silver nanoparticles produced according to the procedure of Hu et al.[1]
NP_{large}	Population of larger particles (details see chapter 5.2.5)
NP_{PAA}	Poly(acrylic acid) stabilized-silver nanoparticles
NP_{small}	Population of smaller particles (details see chapter 5.2.5)
PAA	Poly(acrylic acid)
PDF	Partial differential function
PDI	Polydispersity index
SANS	Small-angle neutron scattering
SAXS	Small-angle X-ray scattering
SD	Standard deviation
SiC	Silicon carbide

SP-ICP-MS	Single-particle inductively coupled plasma mass spectrometry
STEM	Scanning transmission electron microscopy
TGA	Thermogravimetric analysis
TEM	Transmission electron microscopy
WAXS	Wide-angle X-ray scattering

Contents

1 Introduction

Humanity has always striven to explore and expand the limits of its knowledge. In modern society, we are faced with probably two fundamental limits of our knowledge, which are largely determined by the end of the spatial size scale. Within these borders it is possible for us to gain scientific knowledge. On the side of large dimensions, astronomy dominates. It deals with the evolution, propagation and interaction between macroscopic objects of unimaginable size. This world of inconceivable size can be described by equations like the theory of relativity, which allows us to predict the evolution and fate of planets, stars and galaxies. At the other end of size scale, we have the world of the smallest – the quantum world. In this region, the successful macroscopic models seem to fail and the movement of energy and matter is defined by literally "spooky" quantum mechanics, which even do not allow an exact location of electrons. As far apart as these two concepts seem to be, it is even more astonishing that neither world can be explained without the other. The apparent contrast between the two worlds at the ends of the spatial scale is well described by Werner Heisenberg:

"In the experiments on atomic processes we deal with things and facts, with phenomena that are as real as any phenomena in daily life. But the atoms or the elementary particles are not equally real. They are more a world of tendencies and possibilities than of things and facts."

An example of the interplay of both worlds is the nuclear fusion in our stars, which is the fuel of life and cannot be understood without quantum mechanical effects such as the tunnel effect. Now the question arises: Where does our macroscopic world end and where does the quantum world begin? Often it is not a clear border, but a blurred transition. In the region of this transition, nanometer-sized objects offer unexpected possibilities. On the one hand,

macroscopic effects like the growth of particles can be observed. Interestingly, the growth of nano-sized particles proceeds in a similar mechanism as larger particles, for example in an explosive eruption of a volcano. There, small fragments of a few millimeters form when fine ash coalesces around small nuclei of rock fragments (Figure 1). On the other hand, there are also various phenomena which can only be explained by quantum effects, for example the different color of gold nanoparticles in comparison to bulk gold. This phenomenon can be explained by the absorption of the surface plasmon resonance band, which results in a reddish color of the gold nanoparticles (Figure 1). Since both worlds unite on the nanometer scale, nanoparticles offer an incredible potential in the fields of biological applications, catalysis and material applications.

In this thesis, silver nanoparticles are used to set up a versatile particle system for the investigation of their structure-activity relationship in various applications, ranging from catalysis to biological purposes. The particles are synthesized by classical and microwave-assisted heating and thoroughly characterized by small-angle X-ray scattering (SAXS). This enables the monitoring of changes in size and size distribution widths, which is of significant importance to activation, de-activation and growth.

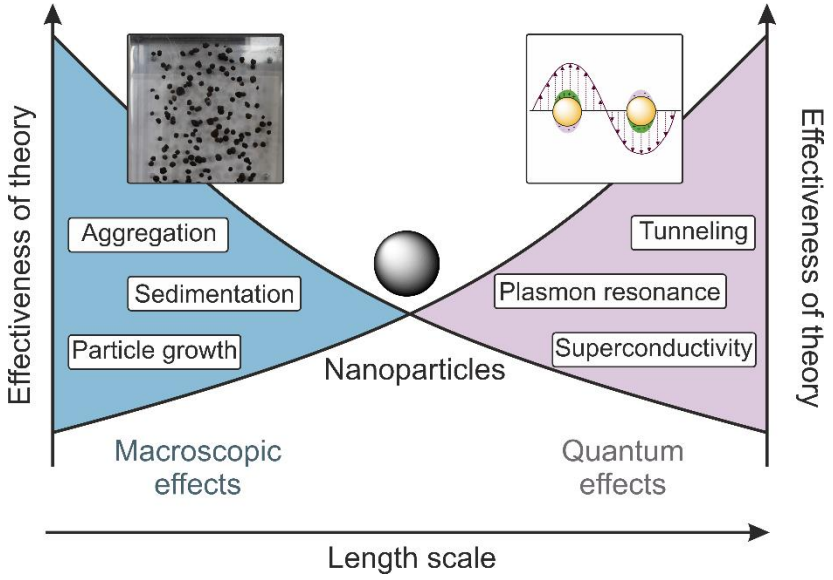

Figure 1. Scheme of the interplay of macroscopic effects and quantum effects in nanoparticles. The left inset shows small-sized fragments formed of fine ash, which coalesces around small nuclei of rock fragments during the eruption of the Kilauea volcano. The right inset shows schematically the emergence of a surface plasmon resonance.

2. Motivation and Scope

In the past five years there has been a rapid rise in the use of nanomaterials in consumer products. According to the Nanodatabase, an European research project, the amount of products which contained nanomaterials increased in the past five years from 1215 to 3037 products.[2] In particular, silver nanoparticles are frequently utilized because of their well-known antimicrobial and optical properties.[3] They are one of the most widespread types of nanoparticles in consumer products, ranging from children's toys and medical instruments to textiles and coatings for food containers.[4-7] However, the assessment of the toxicological potential of silver nanoparticles remains challenging. Studies in this field show highly controversial results: There are studies which suggest that silver nanoparticles could cause specific "nano-effects". For example, a study of Haase et al.[8] showed that silver nanoparticles might have a stronger effect on neural signal transduction processes than silver ions. On the contrary, other investigations claim that the toxicity of silver nanoparticles is solely caused by the release of silver ions.[9] In general, the diversity of results shows that a consistent evaluation of the toxicological potential of silver nanoparticles is not yet possible. A major drawback for the comparison of these different studies is the utilization of diverse, partly inhomogeneous silver nanoparticle systems. Often, the used particles lack thorough characterization because this would require sophisticated and complementary methods, which often involve a lot of effort. Therefore, the development of a standard system which is versatile enough to provide the possibility for different biological and chemical investigations could provide substantial help.

In this thesis, such a versatile system of silver nanoparticles is synthesized and thoroughly characterized. It was the aim to synthesize rather small particles since the exceptional properties of nanoparticles especially arise in the sub-20 nm region. The particles

are extensively characterized (chapter 5.1.1) and used in an international inter-laboratory comparison (chapter 5.1.3), showing their high stability and eligibility as calibration standards for the lower end of the nanoscale. The classical synthesis was systematically compared to the modern route of a microwave-assisted production of silver nanoparticles. This comparison provides the possibility to investigate whether the discussed non-thermal microwave effects are present (chapter 5.1.2).

The versatility of the silver nanoparticle system is shown by the facile ligand exchange with proteins and biomolecules, namely albumin, glutathione and tyrosine. The surface coating can be exchanged completely (chapter 5.1.1). These differently coated silver nanoparticles are characterized and used firstly in a catalytic application for the reduction of 4-nitrophenol (chapter 5.2.1). Within this work, the dependence of the reactivity on the corresponding coating is demonstrated.

As a preliminary consideration for future biological applications, chapter 5.2.2 includes an investigation of the binding behavior of fluorescent ligands to the silver nanoparticles. Two different possible fluorescent markers are investigated regarding their adsorption and also desorption performance. This enables an estimation of the stability of the nanoparticle-marker complex and also provides a realistic time-span for the co-location of fluorescent marker and nanoparticle in biological applications.

The initial particle system is subsequently used in an artificial digestion to monitor the changes in size distribution and reveal whether the particles could pass the human digestion system preserving their nano-scaled size (chapter 5.2.3). The model of human digestion was chosen since the oral ingestion is the major uptake route for silver nanoparticles.[10] The digestion of silver nanoparticles automatically raises the question of the behavior of ionic silver in an artificial digestion since silver is known to continuously release silver ions from its surface. This topic is in the focus of chapter 5.2.4, wherein the formation of nanoparticles is investigated as well as their composition.

The release of silver ions from silver nanoparticles is a central issue for the assessment of the toxicological potential. The released ions can show complex transformations in biological environments.[11] Therefore, the silver particle system used in this work was further investigated with respect to enhanced ion release and subsequent transformations through the contact with biologically relevant molecules, namely glutathione, in chapter 5.2.5.

In summary, this work demonstrates the synthesis, characterization and versatile application of a silver nanoparticle system. The utilization of small-angle X-ray scattering (SAXS) for these purposes plays a crucial role since it enables investigation of the particles *ex situ* as well as *in situ*, and also provides the advantage to measure directly in complex media like the digestive juices.

3 Theoretical Background

3.1 Nanomaterials

It was 1959 when the physicist Richard Feynman held his famous talk "There's plenty of room at the bottom", which firstly introduced the concept of nanotechnology.[12] It included pioneering ideas about manipulating materials at the scale of a few nanometers or even atoms. His vision of writing the whole Encyclopaedia Britannica on the head of a pin is considered as the starting point of research into controlling and investigating matter at the nanoscale. The term "nano" is derived from the Greek word "nános", which means dwarf. Nanomaterials are defined by having at least one dimension in the order of 1 – 100 nm (Figure 2). For comparison: A human hair has approximately a thickness of 80 000 nm.[13]

The investigation of nanoparticles with regard to their toxicity and also for the development of new materials is becoming increasingly important, as more and more nano-products are used in our daily life to improve product properties. According to statistics from the Danish ecological council and Danish consumer council the number of products which contain nanoparticles has increased from 1215 to 3037 in the last five years.[2] The reason for the high interest in nanomaterials is that the properties of these materials at the nanoscale can be very different from their macroscopic analogs. These differences originate from two factors: First, nanomaterials have a specific surface-to-volume ratio, which means that the surface area of a nanomaterial is comparably larger than for the same mass of material in bulk form. For example, a sphere consisting of 1 g silver has a surface area more than a hundred thousand times smaller than the same mass of silver nanoparticles with a size of approximately 2 nm.

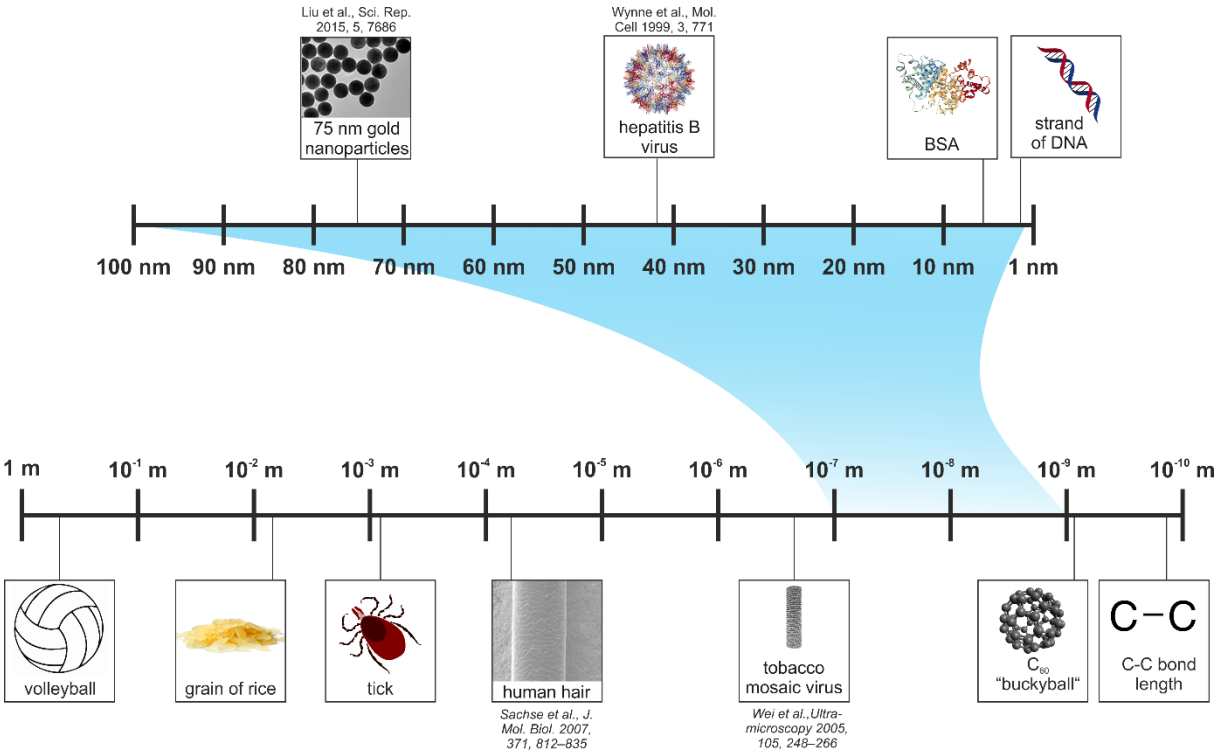

Figure 2. Length scale ranging from 1 m to 10^{-10} m for the illustration of the nanometer range with examples. The region defined for nanomaterials, from 10^{-7} m (100 nm) to 10^{-9} m (1 nm), is expanded.[13]

The high surface area of nanomaterials results often in higher chemical reactivity, which is used for catalytic applications. It can also affect their optical and electrical properties, as well as their mechanical strength. The second factor is quantum effects, which are present at the lower end of the nanoscale. These effects are responsible for optical, magnetic and electrical changes in the behavior of nanomaterials.[13] These specific features lead to the utilization of nanomaterials in almost every aspect of our daily life. They are used in common household products such as tooth paste and sunscreen, but also for solar cells, as catalysts and in medicine.[4, 6, 14]

The classification of nanomaterials can be done by differentiating between materials that are nanoscale in one dimension, two dimensions, and three dimensions (Figure 3), i.e. for one dimensional nanomaterials the other two dimensions are extended and not in the nano-scaled region. One dimensional nanomaterials comprise layers like thin films and surface coatings which are, for example, used for the production of electronic devices. Two dimensional nanomaterials are nanowires, nanotubes, and biopolymers. The most famous example is carbon nanotubes, which show a high mechanical strength and high electrical conductivity. Three dimensional nanomaterials include nanoparticles, fullerenes, dendrimers,

and quantum dots. Quantum dots were first synthesized in the 1980s and are semiconductor particles.[15] The specific feature of these particles is that the color can be exactly tuned by controlling the size of the particles. Quantum dots are small enough that quantum effects dominate which results in a limitation of the energies at which electron and electron holes can exist in the particle. These energies correspond to a specific wavelength and also color. Therefore, smaller quantum dots appear in green and blue colors, whereas larger quantum dots show reddish colors. The specific color is also influenced by the exact composition of the particles.

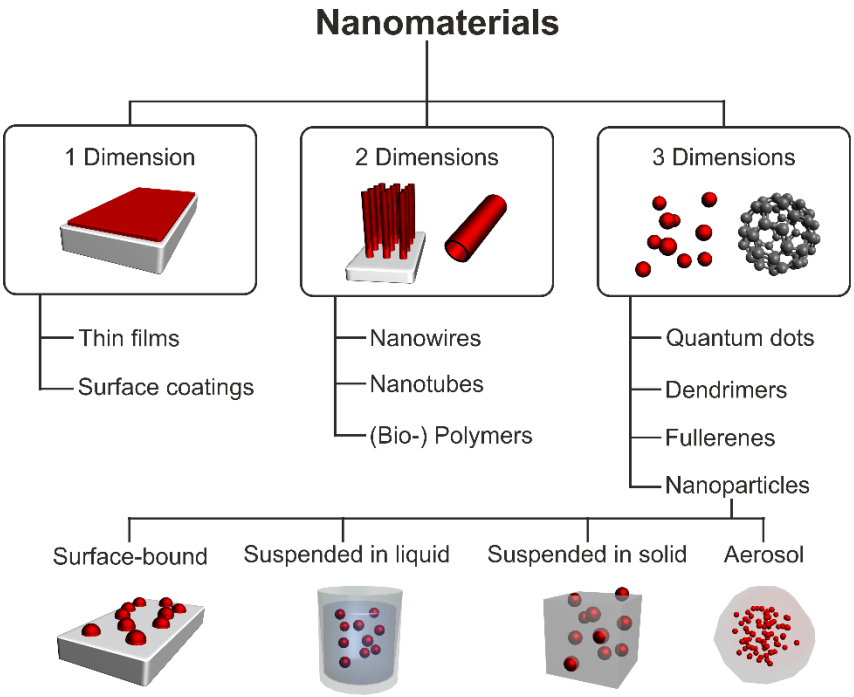

Figure 3. Classification of nanomaterials according to the dimensions of nano-scaled size. Nanoparticles are subdivided into their prevalence in different matrices.

Nanoparticles can be available in different matrices (Figure 3): They can be present as an aerosol which corresponds to a solid in a gas phase, e.g. cigarette smoke.[16] The particles can be surface-bound or suspended in solids, such as the so-called black diamond, which is an impure diamond consisting of diamond, graphite and amorphous carbon. The most common appearance of nanoparticles are in suspensions in liquids.[13]

Although Feynman was the first person to directly mention nanotechnology, nanomaterials have been already used for centuries. For example, gold and silver nanoparticles were used as coloring pigments for glassware and ceramics since the

4th century AD.[17] The color of gold ranges from red over blue to metallic gold, depending on the size of the particles. The challenge was and is still today to produce monodisperse particles – particles of the same size and, therefore, also color and other properties. Today we know that there are two fundamental routes for the production of nanomaterials:[18] The first one is the "top-down" approach, where small structures from larger pieces of material were gained. The disadvantages of this approach are that it requires a high energy contribution, is usually very expensive and produces materials with a high polydispersity.[19-20] The second pathway to produce nanomaterials is the "bottom-up" approach. It corresponds to chemical-physical synthesis, whereby principles like self-organization are used to synthesize nanoparticles starting from atoms and molecules.[21] For the synthesis of monodisperse particles according to the "bottom-up" approach, the LaMer principle plays an essential role. In 1950 LaMer first presented the theory of nucleation and growth for the synthesis of colloidal sulfur.[22] According to this theory, different synthesis pathways for the synthesis of colloidal nanoparticles were developed. It becomes clear that the synthesis of monodisperse particles requires fast and discontinuous nucleation and slow growth.[22] Central to this theory is the LaMer diagram, which represents the monomer concentration as a function of time (Figure 4).

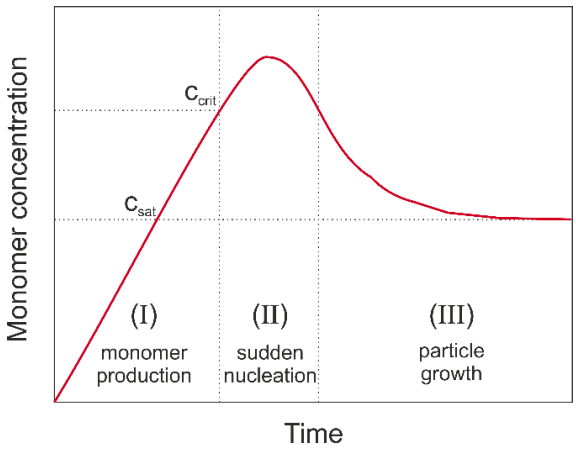

Figure 4. LaMer diagram: Evolution of monomer concentration over time (based on LaMer et al.[22]).

The diagram shows the three phases which are of crucial importance in the synthesis of nanoparticles. In phase I, the concentration of monomers continuously increases. This results from the reaction of the precursor to monomers. In the production of metal nanoparticles, this is usually a metal salt that is reduced to monomers. Silver nitrate is commonly used as a metal precursor in the preparation of silver nanoparticles. Nucleation is

not initiated in this phase because the critical concentration of monomers has not yet been reached, and the energy barrier for nucleation is therefore too high. The monomer has a much lower solubility in the solvent than the precursor. This means that if a saturation concentration c_{sat} is exceeded, the solution is supersaturated. If the monomer concentration achieves the critical concentration c_{crit}, phase II starts. This is where the sudden nucleation takes place. Due to the rapid nucleation process, in which particles are formed which have exceeded the critical size, the monomer concentration drops below the critical value again. Thus phase III is initiated, in which the growth of the particles takes place. No further nucleation occurs in this phase. The particles grow through further consumption of monomers until they fall below the saturation concentration again. The particles are growing through Ostwald ripening, where smaller particles dissolve in favor of larger ones.[23] An important factor for the production of nanoparticles is that nucleation and growth are separated, and thus enable the formation of monodisperse nanoparticles. This separation can be achieved either temporally, locally or by the occurrence at different temperatures.[24]

There are also alternative approaches to explain the formation of particles. For example, Polte et al.[25] dealt with the growth of particles by coalescence. They assumed that growth does not occur through the addition of monomers, but only through the aggregation of the formed small nuclei.

3.2 Silver Nanoparticles

3.2.1 Properties

The utilization of silver in its bulk form goes back to the 10th century BC.[26] Over the millennia it has been primarily used for medical applications due to its antimicrobial properties (see chapter 3.2.3). The first mentioned synthesis of silver in its nano-scaled form was in 1889, when M. C. Lea described the production of citrate-stabilized silver colloids.[3, 27] Today, silver nanoparticles are produced on a large scale, corresponding to an average industrial production of 500 t per year. It is predicted that the global production of silver nanoparticles will further grow to 800 t per year in 2025.[28] The reason for the frequent use of silver nanoparticles in consumer products and products of our daily life are their specific optical and antibacterial properties. These properties are a consequence of the specific surface-to-volume ratio of the small particles, which results in a higher chemical reactivity, and of the emerging quantum effects, which mainly influence the optical properties.

In its nano-sized form, silver shows substantially different properties than in bulk material. Alshehri et al.[29] reported a high electrical and thermal conductivity of silver nanoparticles with a diameter of 18 nm. Furthermore, silver nanoparticles show a reduced melting point. Bulk silver has a melting point of 960 °C, whereas Yeschenko et al.[30] described silver nanoparticles embedded in a silica matrix where the melting point varied between 350 °C and 160 °C depending on the particle size (15 nm and 4 nm radius, respectively). Silver nanoparticles exhibit an enhanced catalytic activity depending on their size and adsorbed ligands. This activity strongly depends on the accessibility of the catalytic active surface and, therefore, on the adsorbed ligands on the silver nanoparticles. A recent study by Zheng et al.[31] showed that silver nanoparticles embedded in an exopolysaccharide show a comparably low catalytic activity despite their small size of 2.5 nm. Probably, the catalytically active particles are not easily accessible through the matrix of the polysaccharide.[32] This elucidates that the catalytic process is complex, and it is not only the size of the particles that is crucial for a high catalytic activity.

As mentioned above, the specific optical properties of silver nanoparticles enable their utilization in various applications. The occurrence of different colors of silver nanoparticles in

comparison with bulk silver can be explained by the surface plasmon resonance. A plasmon is the collective oscillation of the electron gas of a metal. When a light pulse reaches a metallic surface, collective oscillations of the electrons are excited. These propagate in form of waves on the surface. The surface plasmon resonance corresponds to the frequency at which the conducting electrons oscillate at the surface when exposed to a field excited by electromagnetic radiation.[17] In general, according to the free electron model, a metal is composed of positively charged atoms and valence electrons, which are delocalized via the atomic lattice. By interaction with electromagnetic radiation, polarization of the electron density at the surface induces a dipole with areas of higher and lower electron density (Figure 5). This dipole generates an electric field within the nanoparticles, which is opposite to that of electromagnetic radiation and forces electrons to return to their state of equilibrium. This repelling force causes a continuous change in the electron density. A resonance emerges, which is also called surface plasmon resonance. This occurs at a characteristic wavelength of the incident light. It is usually not in the range of visible light. Silver is one of the few exceptions, which means that the dispersions are strongly colored, even at low concentrations of particles.[33]

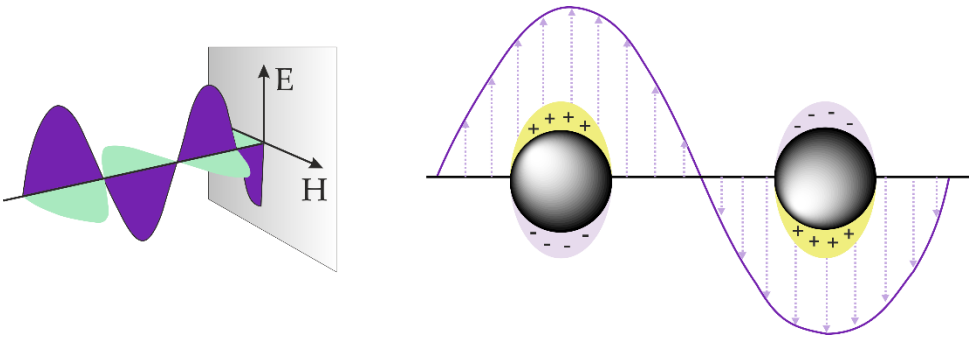

Figure 5. Schematic illustration of surface plasmon resonance of spherical silver nanoparticles.[17]

A direct observation of the movement of electrons in order to conclude the amplitude of the oscillation is not possible. However, an indirect determination is feasible: electronic oscillation causes an increase in the kinetic and electrostatic energy of the electrons. Due to the law of conservation of energy, this energy must be provided by the irradiated light. Thus, a stimulation of the surface plasmons results in a partial weakening of the light. This can be caused by scattering as well as absorption. The sum of both is called extinction. The resonant frequency for excitation of the vibrations is usually in the range of UV/Vis light, which enables detection by UV/Vis spectroscopy.[34]

The frequency of the oscillation depends on the size and shape of the particle as well as on the dielectric constant of the metal and the surrounding medium.[35] Isotropic nanoparticles show only one surface plasmon resonance band, whereas for anisotropic nanoparticles the orientation of the particles in space also plays a decisive role and exemplarily results in two surface plasmon bands for rod-shaped particles.

The adsorption of a ligand shifts the plasmon band, since the surface and thus the local environment of the particles are changed. This results in a change of the dielectric constant, as the charge distribution at the surface is influenced by adsorption of a ligand.[35] The dielectric constant is related to the refractive index *n*:

$$\varepsilon = n^2 \tag{1}$$

Therefore, changing the local refractive index by modifying the surface of the particles causes a shift to higher wavelengths with increasing local refractive index.[36]

3.2.2 Synthesis

For the synthesis of silver nanoparticles various methods have been developed, ranging from reduction of silver salts[37-38] and high temperature syntheses over laser ablation[39] to photoreduction[40] of silver ions. The first methods were the Lee-Meisel method and the Creighton method. Both deal with the reduction of silver salts, whereby the Lee-Meisel method is an adapted version of the common Turkevich synthesis which was used for the production of gold nanoparticles.[37] But unlike the Turkevich method, the Lee-Meisel synthesis produces particles with a broad size distribution. In contrast, with the Creighton method, where silver nitrate is reduced by sodium borohydride, particles with a narrow size distribution are synthesized.[38, 41]

The most common method among the high temperature syntheses is the so-called polyol process. Firstly reported by Fievet, Lagier and Figlarz in 1989,[42] where only micron-sized particles were produced, the synthesis method has improved to yield nano-sized particles with narrow size distributions. Polyols such as ethylene glycol can be considered as water-equivalent but high boiling solvents. Therefore, polyols exhibit solubilities similar to water, and simple, low-cost metal salts like silver nitrate can be used as educts.[43] Polyols as solvents provide the possibility to conduct syntheses at high temperatures of 200 – 320 °C. Furthermore, polyols exhibit another benefit: they show reductive properties which allow the direct preparation of elemental metal nanoparticles.

The synthesis of the silver nanoparticles in this thesis was performed in accordance to a polyol process using ethylene glycol. It is a modified version of the synthesis of Hu et al.[1] Silver nitrate is used as starting material and poly(acrylic acid) acts as a stabilizer. The formation of silver nanoparticles occurs through oxidative disintegration of ethylene glycol. Possible intermediates of the reaction are shown in Figure 6. Starting from ethylene glycol **1**, it can be decomposed into glycol aldehyde **2**, to oxaldehyde **3**, glycolic acid **4**, oxalic acid **5**, and finally into carbon dioxide.[44] With the released electrons the silver ions can be reduced to elemental silver, which is insoluble in ethylene glycol. According to LaMer's principle the nucleation and growth phase is separated. The injection of the silver salt into the boiling ethylene glycol results in a sudden nucleation followed by a continuous growth phase.

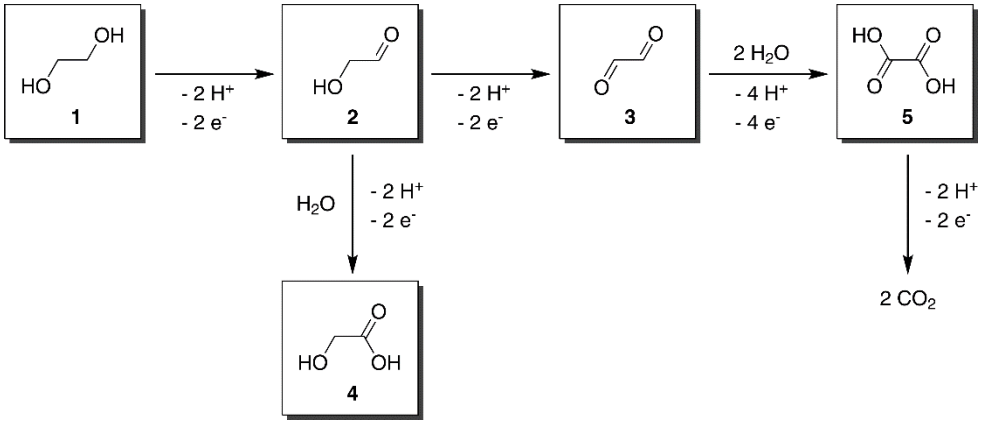

Figure 6. Oxidation pathway of ethylene glycol **1** to glycol aldehyde **2**, oxaldehyde **3**, glycolic acid **4**, oxalic acid **5** and CO_2 (based on Holade et al.[44]).

Depending on the molecular weight of the used poly(acrylic acid), silver nanoparticles of different sizes can be synthesized. Hu et al. described the synthesis of PAA-stabilized silver nanoparticles which exhibit larger radii for the utilization of PAA with a molecular weight of 50000 g mol^{-1} than PAA with a molecular weight of 1800 g mol^{-1}. Due to its bulkier chain the PAA with high molecular weight shows a lower availability of possible binding groups. Therefore, the lower surfactant concentration results in larger particles.[1]

During the last centuries the utilization of microwave radiation to produce silver nanoparticles has generated considerable interest. It is regarded as an alternative to the classical batch synthesis due to the possibility of shorter reaction times, higher yields, and better control over temperature and pressure in the reaction vessel. The heating of the reaction compartment is mainly induced by two mechanisms: dipolar polarization and ionic conduction. Dipoles, namely polar solvents and reactants, are affected by the dipolar polarization and align in the direction of an external electric field. By oscillation of the field, the dipoles re-align themselves according to the field and release energy in form of heat through molecular friction and dielectric loss. An important factor for this heating mechanism is the frequency of the oscillation. If the frequency is too high or too low, no heating will occur because the reorientation of dipoles is not fast enough or too fast, respectively. Hence, a value between these two extremes has to be chosen. In commercial systems (kitchen microwaves) the optimal frequency lies at 2.45 GHz. The second heating mechanism of ionic conduction applies for charged species like ions. They collide under oscillation, according to the electric field, with their neighboring molecules, whereby heat is generated.[45]

The acceleration of reactions through microwave heating is enabled by the use of temperatures even above the boiling temperature of a solvent. Furthermore, in contrast to the classical synthesis using an oil bath, no significant temperature gradients are present. The heat conduction is generated directly in the reaction medium and not directed by external heating of the reaction vessel. The acceleration by using high temperatures is described by the Arrhenius law (equation (2)), in which k corresponds to the reaction constant, T to the temperature, A to a pre-exponential factor, E_A to the activation energy, and R to the gas constant.[45]

$$k = A\, e^{-\frac{E_A}{RT}} \tag{2}$$

During microwave-assisted synthesis, not only accelerated reactions, but also modified products and product distributions have been found. This led to speculations about different microwave effects: first, the thermal and kinetic effects in which an increase of the reaction rate determines the reaction outcome. Herein, the literature distinguishes between effects which can be achieved with conventional heating (purely "thermal" effects) and effects which require microwave-assisted heating ("specific" microwave effects). For the latter, typical examples are selective heating of strongly microwave-absorbing reagents[46] and the reduction of wall effects.[47] The third category of microwave-induced effects is the so called "non-thermal" effects. They are claimed to result from direct interaction of the electric field with molecules in the reaction system, which could alter the pre-exponential factor or the activation energy.[46, 48] These effects are under controversial discussion because it is uncertain whether these effects are a result of misinterpretation influenced by artifacts of temperature measurements.[45] The utilization of silicon carbide vessels could assist in the differentiation of thermal and non-thermal microwave effects. This material strongly absorbs microwave irradiation and has the potential to mimic conventional heating.[49] To investigate how microwave effects influence the reaction pathway and outcome, experiments under the same conditions should be performed in glass and silicon carbide as reaction vessel materials in comparison with reactions conducted via classical batch synthesis.

3.2.3 Interactions with Biological Systems

Silver nanoparticles are among the most widely used and produced nanoparticles. Their application in consumer products has dramatically increased over the last five years. The plethora of commercial products ranges from textiles, cosmetics, food containers to water treatment agents and dietary supplements.[5-6, 50-51] Since silver shows antimicrobial behavior, its modification and synthesis as small nanoparticles for their application in medicine is constantly developed.[52-53] Due to their frequent application, the assessment of their toxicological potential has seen a renewed importance. This includes investigations concerning uptake, transport, excretion and subsequent effects of silver nanoparticles on the human body and the environment. Although an estimation of silver nanoparticle concentrations in surface waters remains challenging,[54] an intake of $70 - 90$ μg silver nanoparticles per day is assumed.[10]

The toxicity of silver nanoparticles is still under debate. There are controversial studies which claim on the one hand that silver nanoparticles cause specific "nano-effects" which are dangerous, like the interference with calcium-mediated signaling processes of neural cells. On the other hand, there are investigations which suggest that the toxicity of silver nanoparticles is solely a result of the released silver ions.[9, 50] Nevertheless, many studies agree that mainly released silver ions are responsible for their antibacterial properties.[4, 28, 50] As early as the first century BC, silver ions were used for disinfection.[26] Today, silver coatings are crucial for medical instruments, whereby a release of high concentrations of silver ions has to be avoided.[55] The group of Carter[56] found reactive oxygen species concurrently with the oxidative dissolution of silver nanoparticles. The release of silver ions is strongly dependent on the particles' characteristics, especially on the size. For example, Kim et al.[57] observed a decreased cell viability of MC3T3-E1 cells with decreasing size of silver nanoparticles. A recent study of Panáček et al.[58] reports of bacteria which exhibit resistance against the antibacterial effect of silver nanoparticles after repeated exposure.

In general, the diversity of results shows that a consistent evaluation of the toxicological potential of silver nanoparticles is not yet possible. The main problem hindering the comparison of the different studies might be the utilization of a wide range of different silver nanoparticles. Mostly, the particles are synthesized in-house or purchased from different

sources, and the physicochemical characterization of the particles is often limited. Hence, nanoscale reference materials could provide substantial help for the improvement of environmental, health, and safety studies of silver nanoparticles.[28]

The characteristics of silver nanoparticles strongly depend on their interaction with biological media and molecules.[59] These interactions can lead to alteration of the particles, including aggregation, agglomeration, dissolution and subsequent new particle formation. Changes in the particle characteristics are also dependent on the surrounding conditions like temperature, pH and salt concentrations.[60-61] Changes in surrounding conditions particularly vary when particles are ingested orally. For example, a pH shift from 6.4 to 2 to 7.5 only occurs during digestion. In this process, the particles pass different digestion steps where physicochemical parameters like pH are shifted over a wide range. Additionally, high salt concentrations are present. The steps of an *in vivo* digestion contain saliva, which is followed by the gastric and intestinal tract. In this thesis, this process is mimicked by an *in vitro* digestion which simulates the three steps, including enzymes, salt concentrations, pH shifts, transit times and a temperature of 37 °C. An artificial digestion provides the possibility to monitor possible alterations in the particle characteristics, such as changes in size distribution, aggregation and dissolution of the particles (described in detail in chapter 5.2.3 and 5.2.4).

Instabilities of the particle systems are mostly attributed to the breakdown of protective coatings. To avoid an aggregation or agglomeration of nanoparticles, two types of stabilization can be used: steric and electrostatic stabilization.[62] Steric stabilization includes the adsorption of polymers, surfactants or other bulky organic molecules on the particle surface. The molecules consist of a metal coordinating group and a sterically demanding residue. Since the nanoparticle surface is electron-poor, a metal-coordinating group with an electron donor function like a carbonyl group is particularly suitable for stabilization. The second option of electrostatic stabilization is a crucial factor for the stabilization of nanoparticles in aqueous media. Hereby, stabilization is achieved by adsorption of charged species on the surface of the particle forming an electrostatic double layer. This results in an electrostatic repulsion between the particles and thus prevents their aggregation. Often both types of stabilization are combined to achieve a preferably stable system.[62]

The use of ligands for the stabilization of silver nanoparticles provides another advantage - it enables the modification of the surface of the particles. Especially, the aspect of

biocompatibility plays a crucial role for their biological application. There are two possibilities to functionalize the particles: firstly, the ligand can be adsorbed to the particle surface *in situ* during synthesis. The second variant is a ligand exchange. A requirement for this is that the ligand, which is used in the synthesis, exhibits a weaker binding to the particle than the exchanging ligand.[63] The particles synthesized and used in this thesis are stabilized by PAA which binds to the silver surface by carbonyl groups. To ensure biocompatibility for biological applications, this ligand is exchanged by different molecules and proteins (Figure 7): glutathione (GSH), tyrosine, and bovine serum albumin (BSA). GSH is a tripeptide composed of glutamate, cysteine and glycine. Tyrosine is a non-essential amino acid and BSA is a globular protein. These three ligands were chosen to enhance the biocompatibility of the silver nanoparticles and to monitor the interactions of the particles with relevant biomolecules.

The binding of BSA and GSH is described by the HSAB principle (principle of hard and soft acids and bases):[64] Lewis bases are electron donors with a free electron pair and Lewis acids are electron acceptors. In the case of silver nanoparticles, the silver is the Lewis acid and the corresponding ligand is the Lewis base. This is in accordance with the classification into hard and soft acids and bases: silver is a soft acid because it contains a large acceptor atom, a low electronegativity and high polarizability. According to the HSAB principle, the most stable complexes are a combination of soft acid and soft base or hard acid and hard base.[64] Therefore, the ligand must be a soft base. Bases with a thiol function are classified as soft bases, whereas ligands with a COOH function are more likely to be considered hard. Therefore, the exchange for a thiol ligand is favored.

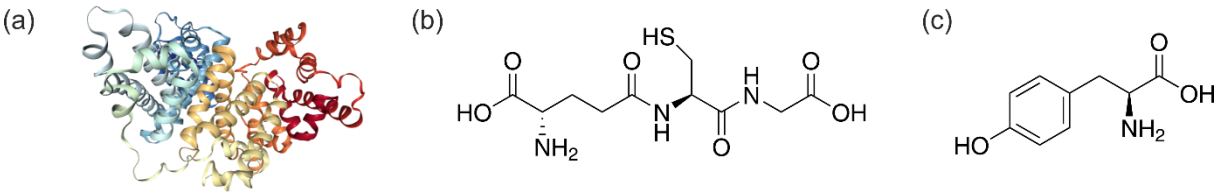

Figure 7. Structures of molecules used for the ligand exchange of the PAA-stabilized silver nanoparticles: (a) BSA, (b) GSH, and (c) tyrosine.

3.3 Methods and Techniques

3.3.1 Dynamic Light Scattering

Dynamic light scattering (DLS) enables the determination of the diffusion coefficient of nanoparticles in suspension. The advantages of this technique are the fast data acquisition, its applicability for a wide range of particle materials and sizes up to the submicron region and its ability of providing a statistically relevant average of the size of nanoparticles. An incident laser beam with a wavelength λ is scattered by a defined scattering angle Θ and registered by a detector. The intensity of the scattered light depends on the scattering angle and the observation time. Since nanoparticles in suspension diffuse according to the Brownian motion in a random walk fashion, a time-dependent fluctuation of the intensity occurs. The fluctuations are influenced by the diffusion coefficient of the particles: small particles diffuse faster which results in a rapid fluctuation of the intensity signal, whereas larger particles diffuse more slowly. To quantify these differences, the method of autocorrelation was introduced. It considers the time-dependent signal monitored at different time intervals. If the scattered intensity at an arbitrary time is presented as $I(t)$ and those after a subsequent delay time τ are represented by $I(t + \tau)$, the normalized autocorrelation function $g^2(\tau)$ can be defined as:[65]

$$g^2(\tau) = \langle I(t)\, I(t+\tau) \rangle \tag{3}$$

The decay of this function is associated with the diffusion coefficient of the scattering objects. The autocorrelation function $g^2(\tau)$ is related to the first-order correlation function of the electric field $g^1(\tau)$ (also known as field autocorrelation function) according to equation (4). This is also known as the Siegert relation. Here, B corresponds to the baseline, whereas A is the amplitude of the correlation function and depends on the geometry and alignment of the instrument.[65]

$$g^2(\tau) = B[1 + A\, g^1(\tau)^2] \tag{4}$$

For a monodisperse particle system, the autocorrelation function $g^2(\tau)$ can be approximated by an exponential decay with the delay time τ, as given in equation (5). Here, D is the translational diffusion coefficient of the scattering particles, and q corresponds to the scattering vector as defined in equation (6). Here, n is the refractive index of the medium.[66]

$$g^2(\tau) = B\left(1 + A\, e^{-2Dq^2\tau}\right) \tag{5}$$

$$q = \frac{4\pi n}{\lambda} \sin\frac{\Theta}{2} \tag{6}$$

For the approximation of spherical particles, the hydrodynamic radius R_h can be determined from the diffusion coefficient according to the Stokes-Einstein relationship:

$$D = \frac{kT}{6\pi\eta R_h} \tag{7}$$

Here, k is the Boltzmann's constant, T is the absolute temperature, and η corresponds to the solvent's viscosity. However, the Stokes-Einstein equation can only be applied for non-interacting, spherical particles. It is therefore not suitable for determining sizes of particles with different geometries.[66]

In practical application of DLS for the determination of particle sizes, perfectly monodisperse systems are rather rare. Indeed, polydisperse systems in which the determination of size distributions is of high interest are common. Polydisperse populations lead to a deviation from the mono-exponential decay of the correlation function. Therefore, the field autocorrelation function is adapted by a sum of exponentials, weighted by their amplitudes (equation (8)). According to equation (9), Γ is the decay constant for a specific size. The distribution $G(\Gamma)$ depends on the size and volume fraction of the scattering particles.[66]

$$g^1(\tau) = \int_0^\infty G(\Gamma)\, e^{-\Gamma\tau}\, d\Gamma \qquad \text{with} \int_0^\infty G(\Gamma)\, d\Gamma = 1 \tag{8}$$

$$\Gamma = D\, q^2 \tag{9}$$

For data evaluation in this thesis, the method of cumulants was used. Therein, equation (4) is approximated and expanded by a polynomial (equation (10)). The polynomial is truncated at the second-order term, and contains $\langle\Gamma\rangle$ the average decay rate, and μ_2 which corresponds to the variance of the decay rates.[65]

$$g^2(\tau) = B[1 + A\, e^{-2\langle\Gamma\rangle\tau + \mu_2\tau^2}] \tag{10}$$

The polydispersity index PDI as a measure of the distribution width can be calculated with the help of $\langle\Gamma\rangle$ and μ_2 as given in equation (11). It can be correlated with the standard deviation of the decay rates σ.[65]

$$PDI = \frac{\mu_2}{\langle\Gamma\rangle^2} = \frac{\sigma^2}{2\langle\Gamma\rangle^2} \tag{11}$$

For determination of aggregation in a particle system, the use of a multi-angle set up is beneficial. Since the scattering intensity is proportional to the sixth power of particle size ($I \sim R^6$), the detection of small particles at small angles is hindered in the presence of larger

ones. Therefore, the determination of the diffusion coefficient as a function of the scattering vector q^2 provides the opportunity to compare the resulting values for the hydrodynamic radius at different angles. If the values are similar over the range of scattering angles, no aggregation is present. From the plot of the inverse hydrodynamic radius R_h^{-1} versus the scattering angle q^2, conclusions about the degree of aggregation can be drawn. If the R_h^{-1} increases with q^2, aggregates are present in the particle system.[67]

3.3.2 Small-Angle X-Ray Scattering

Small-angle X-ray scattering (SAXS) provides the possibility of investigating structures and particles in the nano-sized region. It is a non-destructive method which requires a minimum of sample preparation. Particle dispersions can be measured directly in solution or other complex media like digestive juices. Furthermore, SAXS enables the determination of particle sizes and structures over an average of a statistically representative particle ensemble. In this aspect it differs from electron microscopy, where only a comparably small number of particles are monitored.

The basis of a SAXS measurement is the differences in electron density between a particle or structure and its surrounding medium, which determine the contrast.[68] With this, different structure parameters can be investigated ranging from the particle size and shape to the surface and internal structure (Figure 8).

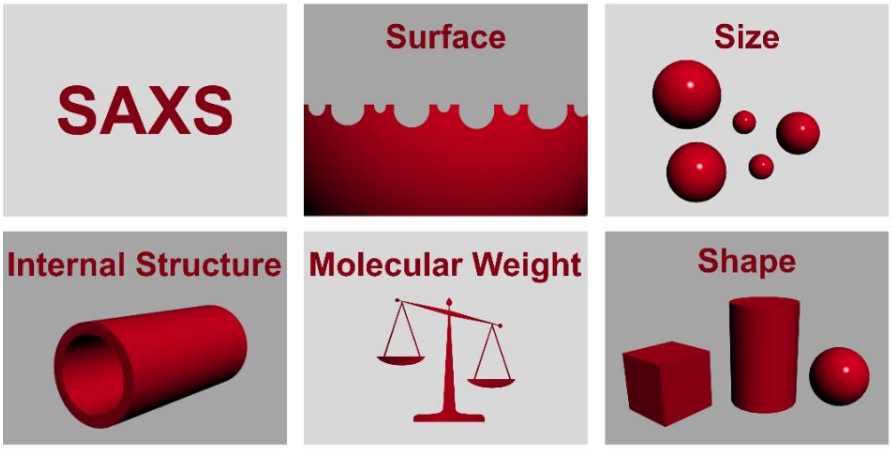

Figure 8. Overview of parameters which can be investigated with SAXS.

For SAXS measurements, two different types of collimation can be used – point or slit collimation. In this thesis, a slit collimation system was used, which provides the advantages of a high beam intensity and a short sample-detector distance. This system is ideal for the investigation of isotropic particles.[69]

A SAXS instrument typically consists of an X-ray tube, a collimation system, a sample holder, a beam stop, and a detector (Figure 9). An X-ray beam is generated by the source and passes through the slits of the collimation system which narrows the beam. Then the sample gets irradiated by the X-rays and scatters the radiation depending on its structure, which is

measured by the detector in dependence of the scattering angle. The beam stop prevents damage of the detector by the high intensity of the incident/primary beam.[70]

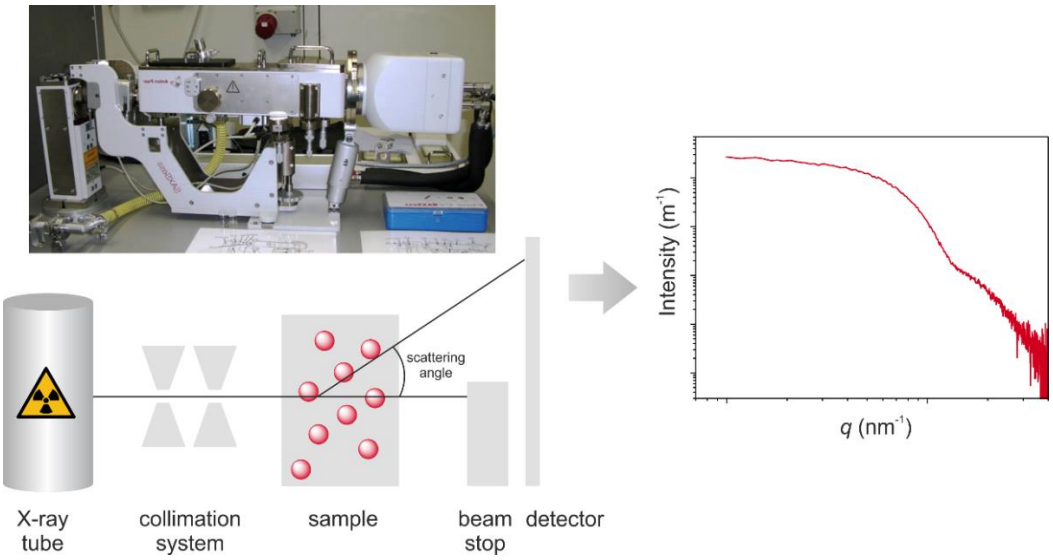

Figure 9. Setup of a SAXS instrument including X-ray tube, collimation system, sample, beam stop, detector and resulting scattering curve of small silver nanoparticles. The photograph shows the SAXSess from Anton Paar used in this thesis.

When X-rays are scattered at electrons, elementary waves are emitted. These waves are emitted at different positions in the sample compartment, and result in constructive and destructive interference at the detector position. The interference patterns are dependent on the observation angle Θ, the orientation, and the distance of the scattering objects. Constructive interference results in bright and destructive interference in dark spots at the detector, which creates a characteristic interference pattern.[70]

The intensity of the scattered X-ray radiation is typically plotted against the scattering vector q. The scattering vector is correlated to the scattering angle Θ of the beam according to equation (12). Therein, λ corresponds to the wavelength of the applied radiation.

$$q = \frac{4\pi}{\lambda} sin\theta \tag{12}$$

From the available q-range, the resolution of a SAXS instrument can be estimated. Depending on the alignment of the instrument, especially the collimation system, a range of $q_{min} < q < q_{max}$ is accessible. According to equations (13) and (14), the system used in this thesis provides the investigation of particles in the range of sizes D_{min} of 0.5 nm to sizes D_{max} of 60 nm corresponding to q-values of 6 nm^{-1} and 0.05 nm^{-1}, respectively. For the investigation of smaller

structures like crystal structures wide-angle X-ray (WAXS) scattering was applied. There, larger scattering angles are accessible.[70]

$$D_{min} \approx \frac{\pi}{q_{max}} \tag{13}$$

$$D_{max} \approx \frac{\pi}{q_{min}} \tag{14}$$

For the particle system used in this thesis – silver nanoparticles in water – the resulting intensity can be described as:

$$\Delta I(q) = N\, I_0\, V_1^2\, (\rho_1 - \rho_2)^2\, P(q)\, S(q) \tag{15}$$

Hence, the measured intensity depends on the particle number N, the intensity of the primary beam I_0, the volume V_1, the electron density difference of the particles ρ_1 and the surrounding medium ρ_2, the form factor P(q), and the structure factor S(q). The latter is a measure for the particle distances and amounts to 1 for diluted systems. The term $\rho_1 - \rho_2$ is equivalent to $\Delta\rho$, the contrast or scattering length density difference.[70] For silver particles dispersed in water, the scattering length density difference amounts to $6.8 \cdot 10^{-3}$ nm^{-2}.

The resulting scattering curves exhibit – in the example of spherical particles – sharp minima if a monodisperse system is investigated. In contrast, if polydispersity is present, these minima vanish and correlate with the averaged sum of the form factor (Figure 10a). Therefore, this is a first indicator by eye for the dispersity of a system.[68]

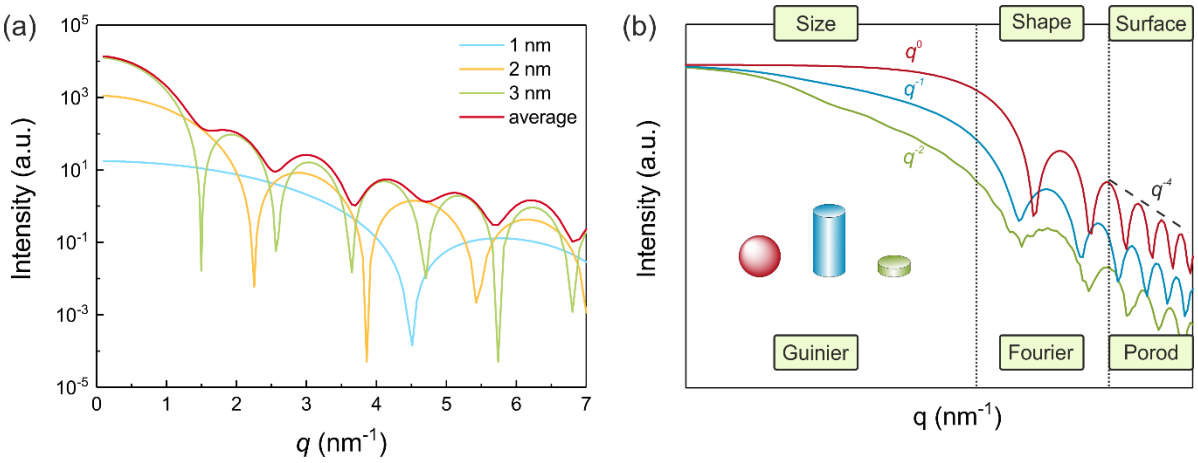

Figure 10. (a) Simulated scattering curves of spherical particles with a radius of 1 nm, 2 nm, and 3 nm. The red curve corresponds to the sum of these particle sizes where the sharp minima are reduced. (b) Simulated scattering curves of a sphere, a cylinder, and a disc (red, blue, and green curves, respectively). Highlighted are the three regions of the form factor, where conclusions about size, shape and surface structure can be drawn (based on Schnablegger et al.[70]).

Furthermore, every particle has a form factor which is characteristic for its structure. As depicted in Figure 10b, the slope of the form factor is mainly influenced by the size of the particles in the region of low q-values, also called Guinier region. At large q-values, in the Porod region, conclusions about the surface structure can be drawn. The middle section, the Fourier region, includes information about the shape and internal density distributions. In a double logarithmic presentation, the slope of the scattering curve in the Fourier region is indicative for different shapes: a slope of q^0, q^{-1}, or q^{-2} implies a spherical, cylindrical or lamellar structure, respectively. For steeper slopes of q^{-3} and q^{-4}, only the Porod region is visible for SAXS, and the structure is probably larger than the resolution of the present instrument.[70-71]

For data evaluation of scattering curves derived by SAXS, different software is available. To evaluate whether the determination of measurands like size, size distribution width and particle concentration are biased by the chosen data analysis method, three different SAXS programs were used and compared in this thesis: SASfit[72], McSAS[73] and IFT.[74] The latter is the abbreviation for indirect Fourier transformation method, developed by Otto Glatter in the 1980s and based on regularization. With SASfit the scattering curve is approximated by a previously chosen mathematical model, whereas McSAS uses a Monte Carlo approach, in which no mathematical model has to be chosen as a prerequisite. Therefore, these three data evaluation procedures are fundamentally different and are chosen for comparison. Other methods like the IRENA package of Ilavsky et al.[75] would also be suitable, but a comparison of all available methods is beyond the scope of this thesis.

4 Experimental

4.1 Materials

Water used for all preparations was Milli-Q grade (18.2 MΩ at 25 °C). All chemicals were used as received and without further purification. The used chemicals are listed in Table 1. Chemicals for the artificial digestion were purchased in the highest available purity (Table 2). The used food components are available supermarket products: native olive oil from Pietro Coricelli Spa, Sucofin skimmed milk powder from Tsi GmbH & Co. KG and Mondamin starch (corn starch) from Unilever.

Table 1. Chemicals used for this thesis.

Chemicals	CAS-No.	Manufacturer	Purity
Silver nitrate	7761-88-8	AppliChem	> 99 %
Ethylene glycol	107-21-1	Acros	> 99 %
Poly(acrylic acid)	9003-01-4	Sigma-Aldrich	-
Sodium hydroxide	1310-73-2	Merck	> 99 %
BSA	9048-46-8	Sigma-Aldrich	≥ 96 %
BSA-FITC	-	Sigma-Aldrich	≥ 7 mol FITC/mol albumin; prepared from crystallized and lyophilized albumin (A 4378)
Glutathione	70-18-8	Merck	≥ 99.9 %
(S)-(-)-Tyrosine	60-18-4	Merck	-
4-Nitrophenol	100-02-7	Fluka	> 99 %

Sodium borohydride	16940-66-2	Sigma-Aldrich	≥ 96%
Hydrochloric acid	7647-01-0	Chemsolute	≥ 37 %
Sodium hydrogen carbonate	144-55-8	NeoLab	-

Table 2. Composition of the artificial digestion juices for saliva, stomach and intestine.

Compound	Supplier	Amount
	Saliva	
NaCl	NeoLab	12.5 mg
NaSCN	Carl Roth	3.8 mg
$Na_2SO_4 \times 10H_2O$	AppliChem	13.7 mg
$NaHCO_3$	NeoLab	3.8 mg
KCl	NeoLab	11.3 mg
KH_2PO_4	AppliChem	15 mg
$CaCl_2 \times 2H_2O$	NeoLab	3.8 mg
Uric acid	AppliChem	2.5 mg
Urea	AppliChem	0.3 mg
Mucin	Sigma-Aldrich	18.8 mg
α-Amylase	Sigma-Aldrich	6.3 mg
	Gastric juice	
NaCl	NeoLab	72.5 mg
KCl	NeoLab	17.5 mg
KH_2PO_4	AppliChem	6.7 mg
Mucin	Sigma-Aldrich	75 mg
Pepsin	AppliChem	25 mg
	Intestinal juice	
NaCl	NeoLab	7.5 mg
$CaCl_2 \times 2H_2O$	NeoLab	12.5 mg
$MgCl_2 \times 6H_2O$	NeoLab	5 mg
$NaHCO_3$	NeoLab	25 mg
Bile extract porcine	Sigma-Aldrich	225 mg

Pancreatin	Sigma-Aldrich	225 mg
Trypsin	AppliChem	7.5 mg
Urea	AppliChem	7.5 mg

4.2 Methods

Small-Angle X-ray Scattering. SAXS measurements were performed in a flow through capillary with a Kratky-type instrument (SAXSess from Anton Paar, Austria) at 21 ± 1 °C. Samples analyzed with SAXS were used as prepared and measured for typically 20 minutes (120 measurement frames averaged over 10 s). The measured scattering data was corrected by subtracting the data of a capillary filled with pure water. The measured intensity was converted to absolute scale according to Orthaber et al.[76] The scattering vector q depends on the wavelength λ of the radiation (λ = 0.154 nm), thus, $q = 4\pi/\lambda \sin \theta$. Deconvolution (slit length desmearing) of the SAXS curves was performed with the SAXS-Quant software (Anton Paar, Austria). Curve fitting was conducted with the software McSAS[77] (version 1.3), SASfit[72] (version 0.94.10) and IFT[74].

Dynamic Light Scattering. The DLS measurements were performed using a multi-angle ALV Instrument (ALV 7004, ALV Langen) equipped with a He-Ne laser (λ = 632.8 nm). Data was recorded at 23 ± 1 °C at scattering angles of 2θ = 26°-146° (8°-steps). Six measurement cycles were conducted with 60 s for each angle. For measurement, the samples were diluted 1:100 with water or NaOH solution (0.1 M) and filtrated using a Millex-LCR syringe filter (450 nm pores, hydrophilic polytetrafluoroethylene). Curve fitting was conducted with the software McDLS (version 1.0.1) and with the method of cumulants according to standard ISO 22412:2017[65] was used for the determination of the hydrodynamic radii at different angles.

IR Spectroscopy (DRIFTS). IR measurements were performed on a Nicolet 6700 from Thermo Scientific with a Praying Mantis™ diffuse reflection accessory from Harrick. NP_{PAA}, NP_{BSA}, and NP_{GSH} were dried and pestled with KBr and filled in the diffuse reflection accessory. The digestive samples were centrifuged for 5 min (6000 rpm, rotor diameter = 19.8 cm). The supernatant was removed and the residue was washed with 10 mL water. This washing procedure was repeated three times. Afterwards the residue was dried at 40 °C for 24 h. The dried samples were pestled with KBr and filled in the diffuse reflection accessory.

UV/Vis Spectroscopy. UV/Vis absorbance spectra were measured using a Cary 300 Scan double-beam spectrometer from Varian. The dispersions were diluted 1:100 with water (NP_{BSA}, NP_{GSH}) and sodium hydroxide solution with a pH of 10 (NP_{PAA}). For the measurements 2.5 mL disposable cuvettes (PMMA) with a path length of 1 cm from Brand were used. The background correction was done with deionized water as reference.

Fluorescence Spectroscopy. The fluorescence measurements were performed using a Fluorolog spectrofluorometer from Horiba and a spectrofluorometer FB-6500 from Jasco. The emission spectra of tyrosine and tyrosine-stabilized particles were recorded using an excitation wavelength of 276 nm. The emission spectra of BSA-FITC and BSA-FITC-stabilized nanoparticles were recorded using an excitation wavelength of 487 nm. The dispersions were diluted with water (tyrosine), or PBS (BSA-FITC) in a ratio of 1:100. Experimental details of the titration and desorption experiments are described in chapter 4.3.

STEM Imaging. The STEM images of tyrosine- and BSA-FITC-stabilized silver nanoparticles were obtained by a Zeiss Gemini Supra 40 scanning electron microscope operating at transmission mode at 10-20 kV. The TEM grids were prepared by placing 2 µL of the particle dispersion on a carbon grid and drying at room temperature.

TEM Imaging. The TEM images were obtained from a FEI Tecnai TF 20 X-TWIN transmission electron microscope equipped with field emission gun and operating at 200 kV.

Wide-Angle X-ray Scattering. WAXS measurements of the digestive samples (chapter 5.2.4) were performed on a Nano-inXider from Xenocs with a solid sample holder unit. The digestive samples were purified by washing them three times with water, followed by centrifugation (6000 rpm, rotor diameter = 19.8 cm, 5 min). The resulting residue was dried at 40 °C. The digestive samples and silver salts were measured for 20 min at medium resolution. The measurements are background corrected with the respective empty sample holder position.

4.3 Experimental Procedures

Classical Synthesis of PAA-Stabilized Silver Nanoparticles

The synthesis of silver nanoparticles was adapted from Hu et al.[1] The synthesis was repeated several times to ensure reproducibility. A solution of 1.9 g (11.4 mmol) silver nitrate in 58.5 mL ethylene glycol was prepared at room temperature. In a 500 mL-three-necked flask, 15.7 g (217.9 mmol with respect to the monomer units) poly(acrylic acid) with an average molecular weight of M_w = 1800 g mol^{-1} was added to 291.5 mL ethylene glycol and heated under stirring to 200 °C. Afterwards, the silver nitrate solution was added within 3 s to the boiling solution while stirring. The mixture was refluxed for 15 min and then cooled to room temperature. The processing of the particles started by adding 800 mL of water with a pH value of 5 and storing the mixture for 24 h. Then, the reddish-brown supernatant was decanted. This procedure was repeated three times. Then, the residue was suspended with 150 mL of water, and a 1% (w/v) sodium hydroxide solution was added dropwise until the pH of the dispersion was adjusted to 10. The color was initially reddish-brown, which turned into olive-green and then into brownish-black. The amount of PAA in the final dispersion was 13% (w/w) as determined with TGA measurements. Note that the samples were dried at 80 °C before TGA measurement to remove water.

Ligand Exchange with BSA, BSA-FITC GSH and Tyrosine

For the ligand exchange with BSA and BSA-FITC, 1 mL of the initial particle dispersion NP_{PAA} was placed in a glass vial, and 1.5 mL of 10^{-4} M BSA or BSA-FITC solution was added. The mixture was stirred for 3 days.

For the transfunctionalization with GSH, a solution of 6×10^{-3} M glutathione in 1% (w/v) sodium hydroxide solution was prepared. 1.075 mL of the GSH solution was added to 2.5 mL of the initial particle dispersion (NP_{PAA}) and stirred for 5 days.

For the ligand exchange with tyrosine, 2.5 mL of the initial particle dispersion (NP_{PAA}) was placed in a vial and 1.2 mL tyrosine (24.3 mg, 0.13 mmol) in NaOH solution (1 wt%) was added while stirring.

Microwave-Assisted Synthesis of PAA-Stabilized Silver Nanoparticles

Silver nanoparticles were produced by modifying the classical batch synthesis of NP_{PAA}. It was necessary to simplify that procedure to a one-pot synthesis for direct comparison of the conventional method with microwave heating. Silver nitrate (c = 32.4 g L^{-1}, solution 1) and PAA (c = 54 g L^{-1}, solution 2) were dissolved in ethylene glycol. A volume of 833 µL of solution 1 was added to 4.167 mL of solution 2 under stirring. Then, the reaction mixture was heated for particle formation, typically to 200 °C for 15 min. The particles were washed by adding 11.4 mL of water and allowing the particles to settle down. The supernatant was then removed after 24 h. This procedure was repeated twice. Thereafter, the residue was filled with water to 5 mL, and an aqueous sodium hydroxide solution (1 w/v %) was added dropwise to disperse the nanoparticles. We used microwave glass vessels and glass flasks with a volume of 10 mL for synthesis. The conventional syntheses were also carried out as a one-pot synthesis in an oil bath. Each vessel was inserted quickly into the hot oil bath to imitate the rapid heating rates available in microwave synthesis.

Catalysis with PAA-Stabilized Silver Nanoparticles

A standard catalytic test reaction as used by Fenger et al.[78] was carried out in 4.5 mL quartz cuvettes with a path length of 1 cm. A volume of 2 mL aqueous solution of 10^{-4} M 4-nitrophenol was mixed with 1 mL of 10^{-1} M sodium borohydride solution. The reaction was started with the addition of 50 µL of nanoparticle dispersion. For clarification, the addition 1 nmol silver (atoms) corresponds to a silver concentration of 3.5377×10^{-5} g L^{-1} in the volume of the reaction mixture. Immediately after particle addition, time-dependent absorption spectra were collected at a temperature of 22 °C. The background correction was done with deionized water as reference.

Fluorescence Titration Experiments

Since the ligand exchange with BSA-FITC takes three days, 12 ligand exchange reactions were prepared with different amounts of BSA-FITC, ranging from 0.03 g L^{-1} to 5 g L^{-1}. After three days of stirring, the emission spectra were recorded with an excitation wavelength of 487 nm. For measurement, 20 µL of the transfunctionalized particles were diluted with 2 mL of NaOH (0.1 M). For the corresponding reference spectra, samples without nanoparticles were

prepared. For the tyrosine-stabilized particles, a different procedure was chosen: the initial PAA-stabilized particles were diluted to a concentration of 0.72 g L^{-1}. In a cuvette, the nanoparticle dispersion was added in 5 µL and later in 10 µL steps to 3 mL tyrosine solution (0.048 g L^{-1}, 0.8 µmol). The solution was mixed and measured by fluorescence spectroscopy (λ_{ex} = 290 nm) after every step. For the corresponding reference spectra, the procedure was conducted without nanoparticles. Instead of the particle dispersion, 0.1 M NaOH was used.

Desorption Experiments

A solution of BSA (0.3 mM) was prepared. The dispersion of the BSA-FITC-stabilized particles was diluted with water by a ratio of 1:150. In a cuvette, 1.25 mL BSA were mixed with 1.25 mL of the diluted dispersion and stirred. As a reference sample, 1.25 mL PBS was mixed with 1.25 ml of the diluted dispersion. The mixtures were measured by fluorescence spectroscopy (λ_{ex} = 495 nm) directly after mixing (t=0) and after 3, 5, 7, 10, and 12 days. Additionally, a 1:1500-dilution of the nanoparticles was used in a similar desorption experiment. The mixture was measured by fluorescence spectroscopy directly after mixing (t=0) and after 2, 5, 7, 9, and 12 days.

Artificial Digestion of Silver Nanoparticles

The *in vitro* digestion was applied as described previously by Lichtenstein et al.[79] and according to an adaptation of DIN19738.[80] Firstly, 1 mL of nanoparticle dispersion (3 g L^{-1}) was added to 7.5 mL artificial saliva with a pH of 6.4. The mixture was incubated while stirring for 5 min in a water bath at a temperature of 37 °C. After adding 17.5 mL of artificial gastric juice, the pH was adjusted to a value of 2 with a solution of 10 wt% HCl, and the suspension was incubated at 37 °C for 2 h. In the last step, the addition of 25 mL of artificial intestinal juice was followed by adjusting the pH to 7.5 by adding $NaHCO_3$. The suspension was incubated while stirring at a temperature of 37 °C for 2 h. The ingredients of the artificial digestion juices are listed in Table 2 (see chapter 4.1). The *in vitro* digestion was additionally conducted in presence of the food components starch, oil, skimmed milk powder (50 mg of each) and a mixture of those (50 mg of each resulting in 150 mg food).

Artificial Digestion of Silver Nitrate

The three steps of the *in vitro* digestion are identical to the digestion of silver nanoparticles. Instead of 1 mL particle dispersion, a solution of silver nitrate (4.7 mg, 0.028 mmol) in water was added to saliva. As a control experiment, water without $AgNO_3$ underwent a separate artificial digestion.

GSH-Induced Disintegration Experiments

The glutathione-induced etching process was studied in an aqueous solution containing 0.7 g L^{-1} silver nanoparticles, 10 g L^{-1} glutathione and 0.25 w/v% sodium hydroxide. This corresponds to a molar ratio of 5 glutathione molecules per silver atom.

5 Results and Discussion

5.1 Synthesis and Characterization of Silver Nanoparticles

5.1.1 Classical Synthesis and Ligand Exchange

This chapter is based on the paper "Catalytic Reduction of 4 -Nitrophenol Using Silver Nanoparticles with Adjustable Activity", which has been partially modified and is reprinted in its original form in Appendix A.1.

In strong contrast to gold nanoparticles, reports on long-term stable silver nanoparticles are rare because the synthesis of silver nanoparticles with reproducible properties is more difficult than expected.[50] Only in a few cases the synthesis requires purely benign chemicals and produces stable particles of uniform size. In this regard, the polyol-based procedure is outstanding, which has been improved by Hu et al. by replacing poly(vinylpyrrolidone) with poly(acrylic acid) (PAA).[1]

In this work, an upscaled variant of the synthesis to produce PAA-stabilized silver nanoparticles (NP_{PAA}) was developed. In contrast to using only 0.1 g of silver nitrate as reported in the original protocol,[1] we attained reproducible results when using up to 2.0 g of silver nitrate in a single batch synthesis with volumes of 350 mL instead of 15 mL. In a second step, a ligand exchange[81] was performed by replacing PAA on the silver core surface of the initial particles with GSH and BSA, resulting in NP_{GSH} and NP_{BSA} particles. The NP_{PAA} are stable for at least 2 years when stored at ambient conditions in the dark at pH values ≥10. In contrast, when using Hu's method for purification of the particles, we found that these NP_{Hu} particles coat the vessel walls (Figure 11a). An amount of approximately 50% of NP_{Hu} was

found as a gray deposit after 6 months. On the contrary, no deposit was found for NP_{PAA}. Therefore, we classify NP_{Hu} and NP_{PAA} as short-term and long-term stable, respectively. The reason for the difference in stability is likely a result of differences in their purification process. Purification of NP_{Hu} includes a centrifugation step, while no centrifugation was used for NP_{PAA}. This could alter the amount of stabilizer, which strongly affects the dispersion stability. Thermogravimetric analysis (TGA) measurements were performed to test this hypothesis. The TGA curve of NP_{PAA} shows its mass as a function of temperature (Figure 11b). The weight reduction occurs in two steps, positioned at 260 and 430 °C for a total of 13 wt%. The remaining silver amounts to 87%. The two steps of PAA decomposition are in agreement with the literature: Lu et al.[82] found two broad degradation steps at 220−280 °C and at approximately 430 °C for PAA with a molar mass of 5000 g mol^{-1}. The TGA curve of NP_{Hu} displays a similar trace but with a much lower total weight reduction of 3−4 %. We interpret that the higher amount of stabilizer found for NP_{PAA} in comparison to NP_{Hu} is the reason for their difference in stability.

The stability of silver nanoparticle dispersions is also affected by pH. When lowering the pH to 7, both NP_{PAA} and NP_{Hu} sediment within an hour. This is expected, since the carboxylic acid groups of PAA provide colloidal stability of silver nanoparticle dispersions when they are negatively charged at basic pH. At pH 7, the carboxylic acid groups of PAA are protonated and can form intermolecular hydrogen bonds.

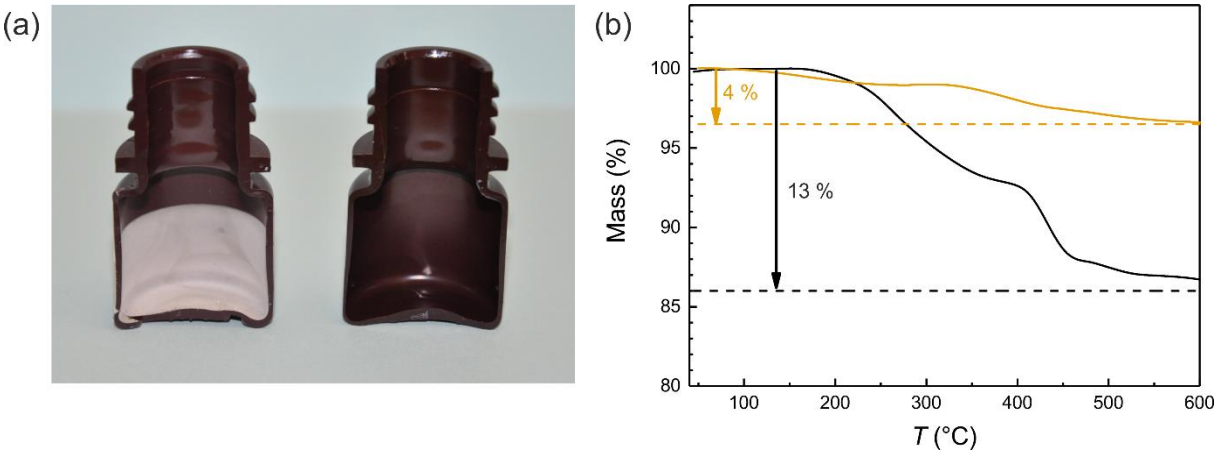

Figure 11. (a) Photograph of longitudinal cuts of vials containing short-term stable NP_{Hu} and long-term stable NP_{PAA} are shown (left and right hand side, respectively). NP_{Hu} and NP_{PAA} were both stored at ambient conditions for 6 months. Deposition of particles at vessel walls is found only for NP_{Hu}. (b) TGA curves of silver nanoparticles showing its mass as a function of temperature. NP_{Hu} (solid orange line) and NP_{PAA} (solid black line) differ in loss of PAA ligand, which amounts to 4% and 13%, respectively. Remaining silver is indicated by dashed lines.

In this state, they cannot provide electrostatic colloidal stabilization. In contrast to NP_{PAA}, NP_{GSH} and NP_{BSA} are stable at pH 7, which coincidentally is a clear indication for a successful ligand exchange.

TEM investigations show that NP_{Hu} comprises a core–shell structure, whereby spherical silver cores are surrounded by a shell of water-swollen PAA.[1] We assume that NP_{PAA} conforms to this structure with uniform core sizes and different shell thicknesses. Sketches of the structures are shown in Figure 12. We employed multi-angle DLS and SAXS as complementary methods to reveal the core–shell structure in detail.

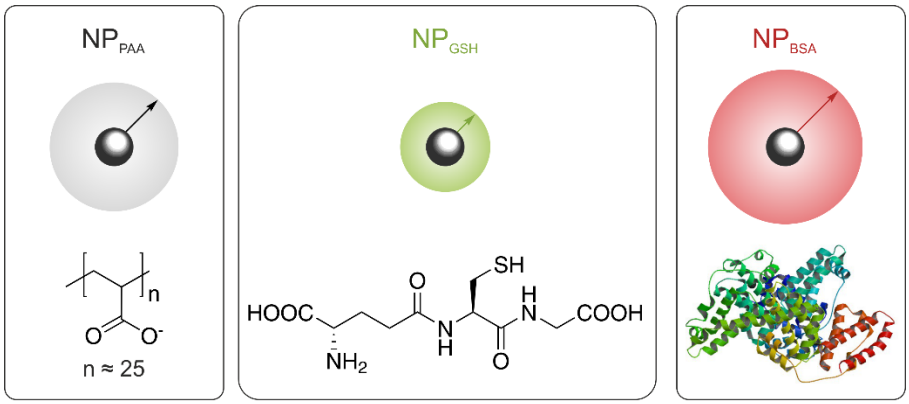

Figure 12. Chemical structures of the molecules that form a shell around the silver cores and provide long-term stability in dispersion. Shell thicknesses are indicated by arrows. Initial particles NP_{PAA} are stabilized with poly(acrylic acid), M_W = 1800 g mol^{-1} (left). The NP_{GSH} are stabilized with glutathione, M_W = 307 g mol^{-1} (middle). The NP_{BSA} are stabilized with bovine serum albumin; M_W = 66463 g mol^{-1} (right).

Multi-angle DLS was used to characterize the hydrodynamic radius of the particles, as well as aggregation and particle–particle interactions. The reciprocal values of the hydrodynamic radius as a function of the square of the scattering vector are shown in Figure 13a. The $1/R_h$ data of NP_{Hu}, NP_{PAA}, and NP_{GSH} are independent of q^2, indicating that no aggregation occurs. Data of NP_{BSA} displays a slight linear increase with q^2 showing that the size distribution is slightly broader. This indicates that all particles undergo solely translational diffusion, and neither aggregate nor significant particle–particle interactions are present. In contrast, polydisperse particles or interacting particles display strongly angle-dependent apparent $1/R_h$ values.[67] Linear fits result in hydrodynamic radii of R_h = 5.9 ± 0.1 nm (NP_{Hu}), 10.0 ± 0.1 nm (NP_{PAA}), 6.8 ± 0.1 nm (NP_{GSH}), and 11.9 ± 0.5 nm (NP_{BSA}) from the extrapolated

values of $1/R_h$ at $q^2 = 0$. Without this interpolation, we found a continuous increase of the apparent R_h values of NP_{BSA} from 10 to 13 nm for 6.4×10^{-4} nm^{-2} > q^2 >3.5×10^{-4} nm^{-2}.

Mean values of the polydispersity index over all angles are PDI = 0.04 ± 0.01 (NP_{Hu}), 0.09 ± 0.01 (NP_{PAA}), 0.13 ± 0.02 (NP_{GSH}), and 0.13 ± 0.02 (NP_{BSA}). For angles larger than 150°, the PDI values of all particles were in the range of 0.01–0.04, which lead us to the conclusion that the particles' size distribution is extremely narrow. However, these values can be considered unrealistic, and we therefore averaged PDI values from angles between 40° and 170°.

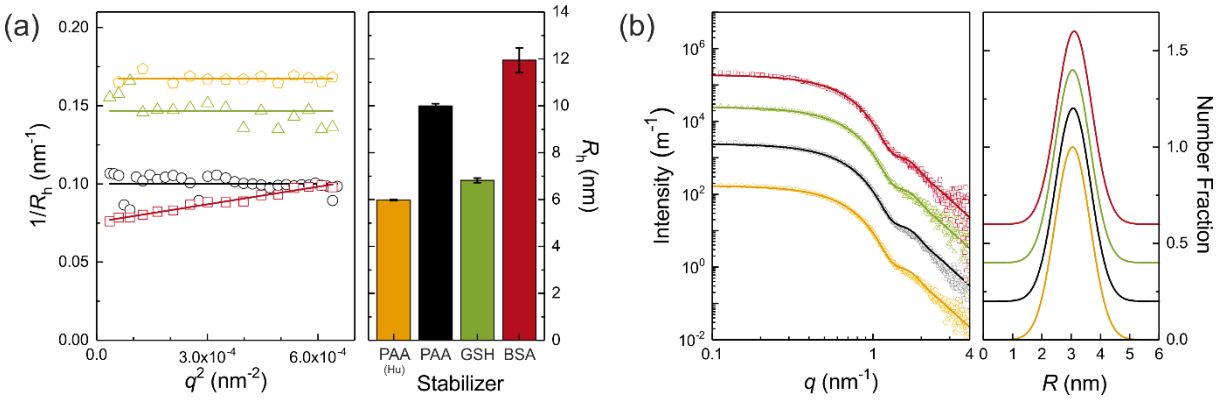

Figure 13. (a) DLS results for silver nanoparticles NP_{Hu}, NP_{PAA}, NP_{GSH}, and NP_{BSA} (orange, black, green, and red, respectively). Left: the reciprocal values of the hydrodynamic radii as a function of q^2 (symbols) were fitted by a linear relationship to determine the extrapolated hydrodynamic radius at zero angle. The fits shown in the left panel result in the hydrodynamic radii shown in the right panel. (b) Left panel: SAXS data and fits of NP_{Hu}, NP_{PAA}, NP_{GSH}, and NP_{BSA} (orange, black, green, and red, respectively) using SASfit[72] resulting in size distributions shown in the right panel. The curves in (b) are shifted vertically for better visibility.

SAXS was used to determine the size distribution of the particles' silver cores. Since the silver cores scatter 4×10^3 times stronger than the PAA shell, SAXS is an appropriate method for the determination of the core dimensions. The measured SAXS data was fitted assuming a spherical scattering object with a Gaussian size distribution using SASfit (Figure 13b).[72] The resulting number-weighted core size distributions for NP_{Hu}, NP_{PAA}, NP_{GSH} and NP_{BSA} are nearly identical. The mean number-weighted particle radius is R_n = 3.0 ± 0.1 nm, and the width of the size distributions is σ = 0.6 ± 0.1 nm, i.e. a relative width of σ_r = 20 ± 3%. We conclude that the core radii are independent of the stabilizer used. This is supported by electron micrographs showing a mean particle radius of $R_{n,TEM}$ = 3.0 nm (Figure 14). In the following we refer only to R_n. Estimates of the shell thickness can now be drawn from the difference between

the particle's hydrodynamic radius and its core radius $R_{shell} = R_h - R_n$, resulting in R_{shell} = 2.9 ± 0.2 nm (NP_{Hu}), 7.0 ± 0.2 nm (NP_{PAA}), 3.8 ± 0.2 nm (NP_{GSH}), and 8.9 ± 0.5 nm (NP_{BSA}).

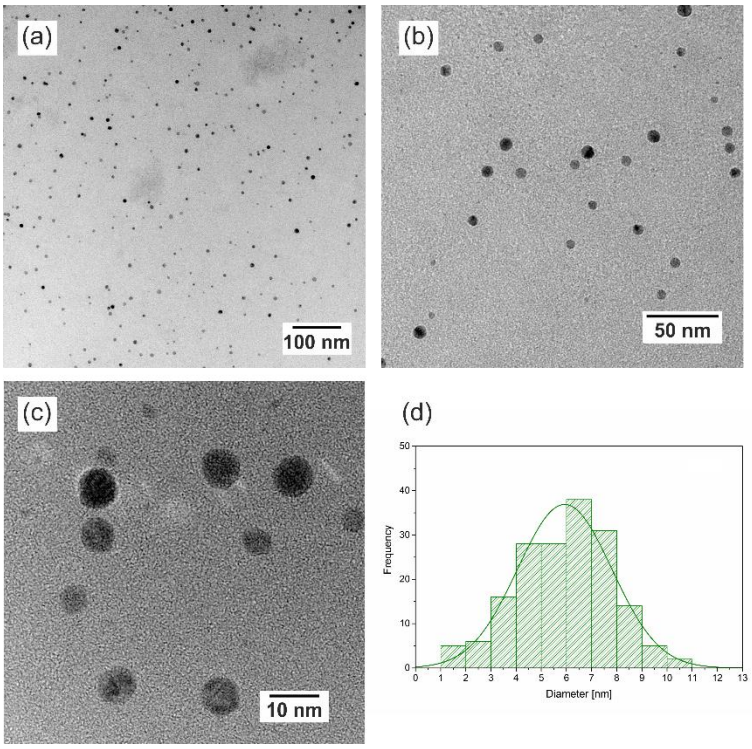

Figure 14. (a)-(c) Electron micrographs of NP_{PAA} at different magnifications (scale bars are 100 nm, 50 nm and 10 nm, respectively). In (c) it can be seen that the particles are single crystals. (d) The histogram of the particle diameters, with its maximum at 6.0 nm.

Knowledge of the particle concentration is of significant importance for the application as a reference material. The particle number concentration in the initial particle solution of NP_{PAA} as determined by SASfit[72] is c_n = (2.2 ± 0.1) × 10^{15} or (4.4 ± 0.2) × 10^{-6} mol L^{-1}, which corresponds to a volume concentration of c_v = 3.1 ± 0.1 g L^{-1}, in agreement with results from McSAS. These results were verified by two additional techniques: firstly, by density measurements resulting in $c_{v,density}$ = 3.0 ± 0.1 g L^{-1}, and secondly by atomic absorption spectroscopy, which provides $c_{v,AAS}$ = 3.01 ± 0.01 g L^{-1}.

To summarize the SAXS analysis, we found that NP_{Hu}, NP_{PAA}, NP_{GSH}, and NP_{BSA} display the same narrow core size distribution with a number-weighted radius of 3.0 nm. The ligand exchange of PAA with GSH and BSA was successful without formation of aggregates. Because of its instability, we omitted NP_{Hu} for the following investigations and concentrate on NP_{PAA} and its derivatives.

The colloidal stability of NP_{GSH} and NP_{BSA} at pH 7 and the DLS results are strong indicators that PAA was removed from the surface of the particles when functionalized with GSH and BSA. However, these findings provide no direct evidence. Within this respect it is helpful that the carbonyl vibration band is very sensitive to binding of carboxyl groups to silver surfaces.[83] Therefore, we utilized FTIR on the carbonyl vibration band to detect PAA (Figure 15a). NP_{PAA} shows a strong absorbance band with a maximum at 1723 cm^{-1}. This band is absent in the spectra of NP_{GSH} and NP_{BSA}. We assign this vibration band to the carboxylate groups of PAA bound to the surface of the silver cores. This has been previously observed by Kumar et al.,[84] who detected carboxylic groups of a poly(acrylic acid) on the surface of silver nanoparticles. A detailed discussion of the FITR spectra of PAA silver nanocomposites is given by Chalal et al.[85] Furthermore, Cardenas et al.[86] investigated PAA on the surface of metal clusters and reported shifts of the carbonyl vibration band between 1717 and 1752 cm^{-1} depending on the cluster. Therefore, the absence of the carbonyl band of PAA at approximately 1723 cm^{-1} in the spectra of NP_{GSH} and NP_{BSA} serves as a direct evidence for the replacement of PAA as stabilizer by GSH, and BSA, respectively.

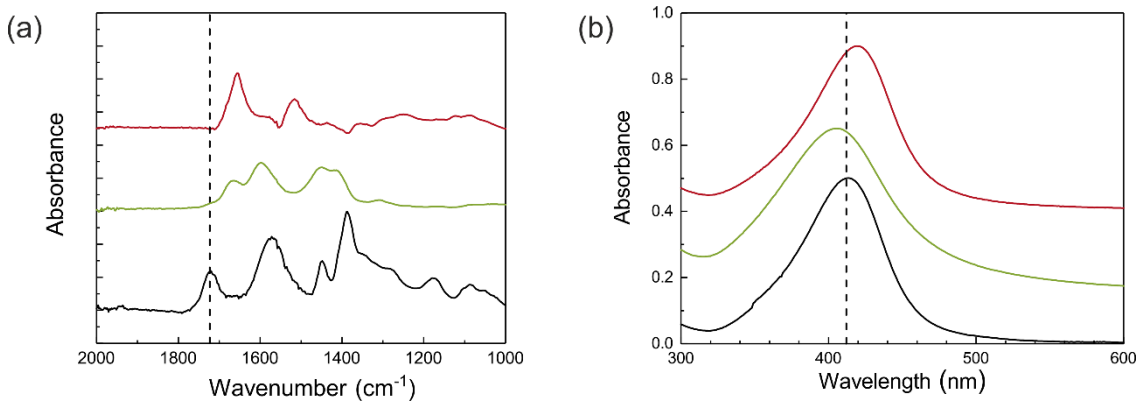

Figure 15. (a) FTIR spectra of NP_{PAA}, NP_{GSH}, and NP_{BSA} (black, green, and red curve, respectively). The dashed line indicates the position of the strong absorbance band of NP_{PAA} with a maximum at 1723 cm^{-1}, which is absent in the spectra of NP_{GSH} and NP_{BSA}. (b) UV/Vis spectrum of NP_{PAA} (black line) in water with a peak maximum at a wavelength of 412 nm (position is indicated by dashed line). The maxima of NP_{GSH} (green line) and NP_{BSA} (red line) are blue-, and red-shifted, respectively. Curves in (a) and (b) are shifted vertically for better visibility.

NP_{PAA} displays an intense UV/Vis absorbance peak with a maximum at λ_{max} = 412 nm and a full width at half-maximum (FWHM) of 58 nm (Figure 15b). This corresponds to the typical surface plasmon resonance band of very small silver nanoparticles and is in agreement with literature.[1] For NP_{GSH}, a blue-shift to a shorter wavelength of λ_{max} = 404 nm is observed

and the absorbance band broadens slightly to FWHM = 72 nm. In contrast, the band of NP_{BSA} is red-shifted to a larger wavelength of λ_{max} = 418 nm, while the band width of FWHM = 61 nm is nearly the same as for NP_{PAA}. The band shifts indicate that PAA was successfully replaced by GSH and BSA, respectively, because it is well-known that silver nanoparticles with different stabilizers can have quite different absorption spectra, even for the same particle size distribution.[87] Shifts of the surface plasmon band are attributed to changes in the refractive index of the particles' surroundings, resulting from changes of the shell composition.[87] Qualitatively, a more hydrophobic stabilizer shifts the plasmon band to larger wavelength. This agrees with our findings for NP_{BSA}, since BSA is much more hydrophobic than PAA, and therefore could explain the small red-shift of $\Delta\lambda_{max}$ = +6 nm. It has been reported that the binding of human serum albumin to Au/Ag alloy particles also produced a red-shift from 410 nm to about 416 nm when citrate is replaced by human serum albumin.[88] In addition, Alarcon et al.[89] found that BSA produces a small red-shift of the peak maximum of silver particles. The blue-shift of $\Delta\lambda_{max}$ = −8 nm when PAA is replaced by GSH has a similar explanation.[88] GSH contains a −SH group which has a strong affinity to silver surfaces, and is likely the reason for the blue-shift of λ_{max}. The UV/Vis spectrum of NP_{GSH} is visually the same as the spectrum of GSH-stabilized silver nanoparticles reported by Li et al.[90] In all cases, the absence of a striking broadening of the UV/Vis bands of NP_{GSH} and NP_{BSA} in comparison to NP_{PAA} additionally confirms the absence of a significant amount of aggregates.

Author contributions: Syntheses of nanoparticles were done by me. Furthermore, I performed SAXS, DLS, UV/Vis and IR measurements and data evaluation. Andreas F. Thünemann and I discussed the results, and wrote the manuscript together with main contribution coming from my side. All authors contributed to the final version of the manuscript.

5.1.2 Microwave Synthesis

This chapter is based on the paper "High-Speed but Not Magic: Microwave-Assisted Synthesis of Ultra-Small Silver Nanoparticles", which has been partially modified and is reprinted in its original form in Appendix A.2.

The use of microwave irradiation has become very popular for the synthesis of nanoparticles, including silver nanoparticles.[45, 91-93] The main advantage of using a microwave for synthesis is a dramatic reduction of the overall processing time because of the available high heating rates. Within this respect, a time-saving synthesis of silver nanoparticles by using microwave irradiation is obviously of interest for scientific as well as for industrial reasons. However, in literature, the influence of microwave radiation on the particle formation mechanism is under controversial discussion.[45] A main aspect of the ongoing dispute is related to the formation of hot spots, which could alter the reaction pathway.[94]

To clarify whether microwave radiation affects the reaction outcome with so-called "non-thermal" microwave effects,[45] this study is aimed to provide a direct comparison of conventional and microwave heating-based syntheses of silver nanoparticles. The comparison was performed by using the same conditions for both. These conditions include reactants, temperature, reaction time, and vessel material. Finally, we want to provide a fast and reliable synthesis procedure for production of ultra-small silver nanoparticles with a narrow size distribution by employing a versatile polyol process.[1] We employed SAXS to obtain the distribution of the core radii. The hydrodynamic radii, including shell and core, were determined by multi-angle DLS.

The synthesis of silver nanoparticles was first performed in ethylene glycol at its boiling point of 200 °C for direct comparison of conventional and microwave-assisted syntheses. Secondly, we used higher temperatures and pressures in the microwave reactor, which cannot be reached in conventional synthesis, because of the solvent's boiling point.

We adapted the previously used polyol synthesis (see chapter 4.1.1) for particle formation. Originally, a hot injection method is employed. This procedure had to be modified because no substances could be added during operation of the microwave. Therefore, all compounds were mixed at 20 °C immediately before microwave heating. The compounds were dissolved in ethylene glycol, which is identical to the procedure for conventional heating

synthesis. The resultant raw product was transferred from ethylene glycol to water using the same purification procedure for both synthesis methods.

The vessel material presents a possible factor influencing the reaction pathway in a microwave reactor because of material-dependent microwave absorption properties. Borosilicate glass exhibits a minimal absorption of microwave radiation, while silicon carbide (SiC) absorbs strongly.[95] Hence, a homogeneous heating of ethylene glycol as a reaction medium in borosilicate glass can be expected, whereas in silicon carbide, heating via heat conduction from the vessel walls occurs.[95] Because of this difference, we investigated the influence of the vessel material on the resulting particle characteristics.

For the comparison of microwave and conventional syntheses, we applied the same conditions as in our previous protocol: a reaction time of 15 min at a temperature of 200 °C. Before purification, the mean radius of the resulting particles does not significantly differ in dependence of the used glass vessel. The particles were characterized as synthesized in ethylene glycol by SAXS. Typical scattering curves and curve fits are shown in Figure 16a. The corresponding size distributions were approximated with Gaussian distributions. Conventional heating synthesis using a borosilicate vessel yielded particles with a mean radius of R_V = 3.0 ± 0.1 nm and a size distribution width of σ = 0.6 ± 0.1 nm.

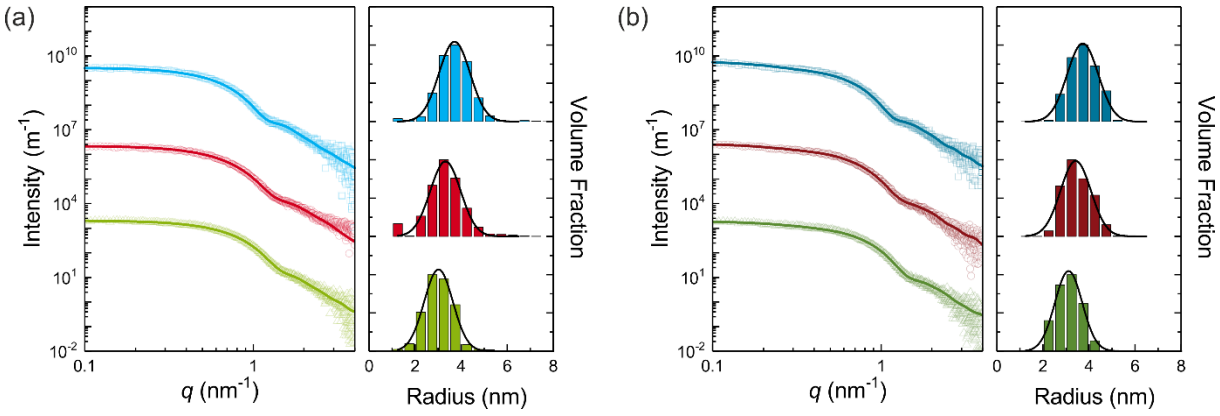

Figure 16. SAXS data (symbols) and curve fits (solid lines) of silver nanoparticles as synthesized in ethylene glycol (a) and after their transfer into water (b). Particles were prepared via conventional heating (glass vessel, green triangles) and via microwave-assisted heating (glass vessel, red circles, and SiC vessel, blue squares). The curve fits in the left panel correspond to the size distributions shown in the right panel (bars), respectively. Gaussian fits of the histograms (solid black lines) provide mean radii. The scattering curves were shifted vertically for better visibility.

Control experiments using a regular laboratory glass flask for conventional heating synthesis resulted in particles with the same values (not shown). For particles prepared via microwave-assisted synthesis, we found R_V = 3.3 ± 0.1 nm and σ = 0.7 ± 0.1 nm when using a borosilicate glass vessel. The values were R_V = 3.7 ± 0.1 nm and σ = 0.7 ± 0.1 nm for synthesis in vessels made of SiC.

The nanoparticles were transferred from ethylene glycol to water. For the conventionally synthesized particles, we obtained R_V = 3.1 ± 0.1 nm and σ = 0.6 ± 0.1 nm, derived by SAXS measurements (Figure 16b). Microwave-synthesized particles using a microwave glass vessel exhibited values of R_V = 3.4 ±0.1 nm and σ = 0.7 ± 0.1 nm. For the particles synthesized in SiC vessels, we found R_V = 3.7 ± 0.1 nm with σ = 0.7 ± 0.1 nm. As an initial conclusion, we state that there is no significant difference in the particle core characteristics between conventional and microwave-assisted syntheses when the same vessels made of borosilicate glass are used (Figure 17). The usage of SiC vessels results in particles with slightly larger core radii but a similar size distribution. Therefore, neither the heating method, nor the vessel material has a substantial influence on the silver nanoparticles' core size. This indicates that the method is surprisingly robust against variations of the synthesis details. This is furthermore confirmed by identical UV/Vis-spectra. Each synthesis type results in particles with an absorption maximum at 413 ± 3 nm.

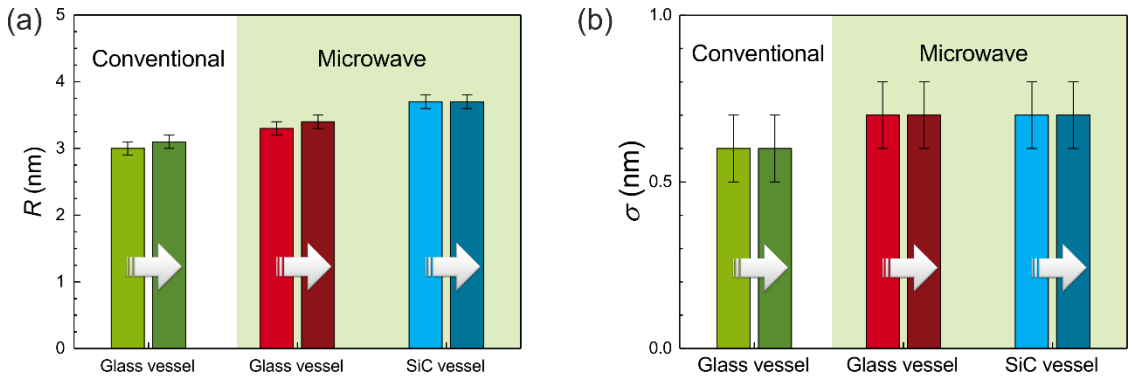

Figure 17. SAXS-derived characteristics of silver nanoparticles prepared via conventional and microwave-assisted heating in reaction vessels made of borosilicate glass and SiC, respectively. Shown are (a) mean radii R_V and (b) distribution widths σ of particles in ethylene glycol (raw product) and water (purified product) displayed as left and right bars, respectively (purification indicated by arrows).

Because of its comparably weak scattering, the PAA shell is practically invisible in SAXS. Therefore, we performed multi-angle dynamic light scattering for determination of the

hydrodynamic radii of the particles in aqueous solution. As the hydrodynamic radius includes the particles' silver core and their polymeric shell, R_h should be larger than the core radius derived from SAXS. We found that the reciprocal hydrodynamic radii $1/R_h$ were independent of the square of the scattering vector q^2 as shown in Figure 18. This leads us to the conclusion that particles from all syntheses are free of aggregates.[67]

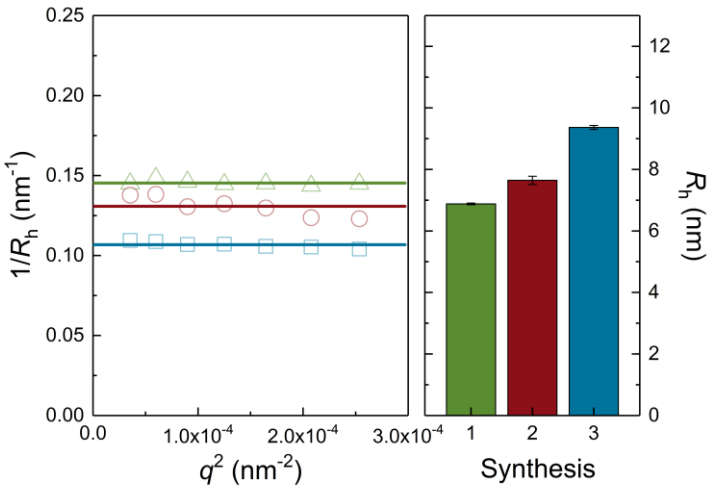

Figure 18. DLS results for silver nanoparticles prepared via conventional heating (green) and microwave heating in glass and SiC vessels (red and blue, respectively) after transfer from ethylene glycol to aqueous solution. Left panel: reciprocal values of the hydrodynamic radii as a function of q^2 (symbols) are constant (solid lines). Right panel: fits shown in the left panel result in R_h = 6.9 ± 0.1 nm (synthesis 1, conventional heating), R_h = 7.6 ± 0.2 nm (synthesis 2, microwave heating, glass), and R_h = 9.4 ± 0.1 nm (synthesis 3, microwave heating, SiC).

The hydrodynamic radius of the particles from conventional heating synthesis is R_h = 6.9 ± 0.1 nm with PDI = 0.11 ± 0.05. The particles resulting from microwave synthesis show a hydrodynamic radius of R_h = 7.6 ± 0.2 nm and PDI = 0.11 ± 0.02 for the microwave glass vessel, and R_h = 9.4 ± 0.1 nm and PDI = 0.12 ± 0.02 for the SiC vessel. Estimates of the shell thickness as $R_{shell} = R_h - R_V$ results in R_{shell} = 3.8 ± 0.2 nm (conventional heating), 4.2 ± 0.3 nm (microwave heating in glass), and 5.7 ± 0.2 nm (microwave heating in SiC). These values indicate that the particle shell thickness depends on the type of heating, that is, it is slightly larger for microwave-assisted synthesis. This contrasts with the heat-type independent core size of the particles. However, carrying out this modified one-pot particle synthesis at 200 °C for 15 min in glass vessels yielded reproducible particle systems irrespective of the heating source and vessel form. The utilization of SiC vessels seems to have a stronger impact on the distribution parameters (Table 3).

Table 3. Characteristics of silver nanoparticle systems from synthesis via conventional and microwave heating.[a]

synthesis	1	2	3
type of heating	conventional	microwave	microwave
reaction vessel	glass	glass	SiC
Particles dispersed in ethylene glycol (raw product as-prepared)			
R_V (nm)	3.0 ± 0.1	3.3 ± 0.1	3.7 ± 0.1
σ (nm)	0.6 ± 0.1	0.7 ± 0.1	0.7 ± 0.1
Particles dispersed in water (purified product, after transfer from ethylene glycol)			
R_V (nm)	3.1 ± 0.1	3.4 ± 0.1	3.7 ± 0.1
σ (nm)	0.6 ± 0.1	0.7 ± 0.1	0.7 ± 0.1
R_h (nm)	6.9 ± 0.1	7.6 ± 0.2	9.4 ± 0.1
PDI	0.11 ± 0.05	0.11 ± 0.02	0.12 ± 0.02
R_{shell} (nm)	3.8 ± 0.2	4.2 ± 0.3	5.7 ± 0.2

[a] Types of reaction vessels were borosilicate glass (synthesis number 1 and 2) and silicon carbide (SiC, synthesis 3). The particle core radii, R_V, and their size distribution widths, σ, of particles in ethylene glycol and after their transfer to water were determined by SAXS. The hydrodynamic radii, R_h, and the PDIs of particles in aqueous solution were determined by DLS. The shell thickness, R_{shell}, was calculated as $R_h - R_V$.

Because we wanted to take advantage of performing microwave synthesis at a high reaction rate, we investigated the results of the synthesis in terms of particle size and yield at different temperatures for a constant reaction time of 3 min. To study the particle formation process of our system, firstly the syntheses were carried out below the boiling temperature of ethylene glycol (197.5 °C) at 150 °C and then at temperatures of 200, 250, and 300 °C. The corresponding pressure values were 1, 1, 4, and 11 bar, respectively. We found no particle formation at a reaction temperature of 150 °C. This is in accordance with our expectation, because the polyol process is initiated once the boiling temperature of ethylene glycol is reached.[1] Then, oxidative decomposition of ethylene glycol results in the reduction of silver ions, forming silver atoms. These atoms first coalesce successively to silver clusters and further to nanoparticles, probably following the particle formation mechanism described by Polte et al.[25] At a reaction temperature of 200 °C, particles were formed; however the reaction yield shows an incomplete turnover of the silver ions within 3 min of heating. The formed particles exhibited a mean radius of R_V = 2.3 ± 0.1 nm and a distribution width of σ = 0.6 ± 0.1 nm (Figure 19a). The reaction was incomplete with a particle yield of 86 ± 5% (Figure 19b). The

size characteristics of the particles produced at 250 °C, as synthesized in ethylene glycol, are R_V = 3.7 ± 0.1 nm and σ = 0.9 ± 0.1 nm. For the particle synthesis at 300 °C, we determined R_V = 4.1 ± 0.1 nm and σ = 1.1 ± 0.1 nm. The yields of 94 ± 5% for 250 °C and 98 ± 5% for 300 °C indicate that the reaction was completed at both temperatures within 3 min.

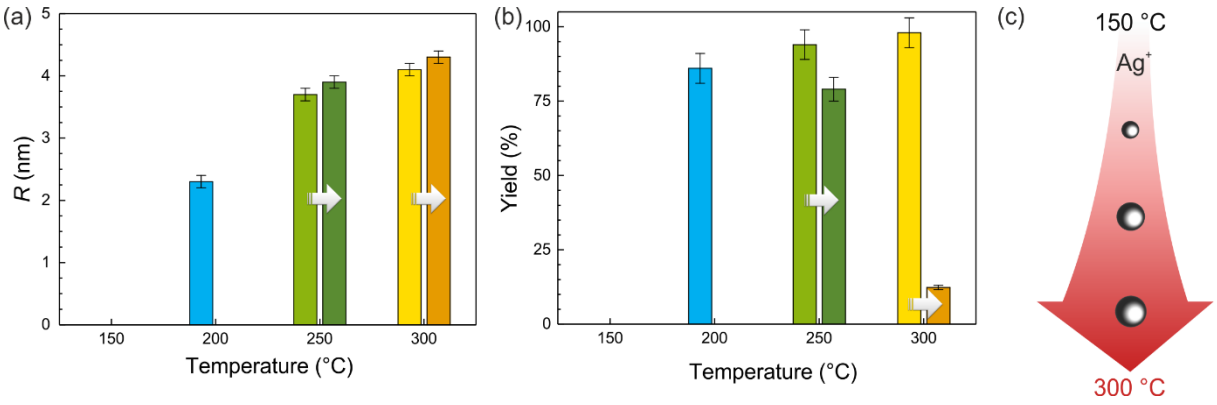

Figure 19. Three-minute synthesis at different temperatures (150, 200, 250, and 300 °C). Comparison of (a) mean radii R_V and (b) product yield before and after purification (left and right bars, respectively). (c) Scheme of the increasing particle size with increasing reaction temperature.

We transferred the batches with complete yield from ethylene glycol to water and found that the particle size characteristics remain constant (Figure 19a). Surprisingly, the 200 °C batch with the uncompleted reaction cannot be transferred from ethylene glycol to water. Probably, remaining silver ions, which are present from the incomplete conversion of Ag^+ to Ag^0 after 3 min at 200 °C are causing this behavior. One may speculate that Ag^+ ions adsorbed onto the PAA-covered silver nanoparticle surface prevent the solvent transfer. The particles synthesized at 250 and 300 °C display product losses resulting from the transfer procedure of 16 ± 2 and 88 ± 10%, respectively (Figure 19b). Thereby, the former value represents an acceptable result for a purification procedure in contrast to the latter one. A partial degradation of PAA at a temperature of 300 °C might lead to the high product loss. Thermal degradation investigations of PAA support this assumption.[82]

DLS measurements of the purified particles display hydrodynamic radii within a range of 8–11 nm, without significant dependence on the temperature used for the microwave synthesis. The PDIs are tendentially lower when the synthesis was performed at 250 °C (PDI = 0.19 ± 0.02) than at 300 °C (PDI = 0.28 ± 0.02).

The formation of larger particles with increasing temperature, as schematically depicted in Figure 19c, is initially surprising. Intuitively, one expects that the higher the temperature, the higher the number of seeds from which the particles grow, and therefore, the final particle size should decrease with increasing temperature. However, if we consider a mechanism of coalescence of silver clusters, more clusters coalesce at higher temperatures to form a nanoparticle. Therefore, we assume temperature-dependent cluster coalescence as a dominating mechanism to explain the difference in the particle size. Clark et al.[96] provided a theoretical description on controlling the size distribution of nanocrystals via the production conditions.

The findings above suggest that a microwave reaction temperature of 250 °C is an optimum in terms of particle yield for three-minute syntheses. Reducing the reaction time further to a minimum of 30 s still led to a complete conversion. The particle size distribution parameters are nearly identical to the standard reaction conditions (200 °C, 15 min) and do not significantly change upon purification. In comparison, mean radii of R_V = 3.3 ± 0.1 nm (200 °C) and R_V = 3.4 ± 0.1 nm (250 °C) before purification, as well as R_V = 3.6 ±0.1 nm (200 and 250 °C) after purification are obtained (Figure 20a). The distribution widths before and after purification amount to σ = 1.0 ± 0.1 nm (200 °C) and σ = 0.8 ± 0.1 nm (250 °C). The scattering patterns of the purified systems are highly comparable, as shown in an overlay of the data in Figure 20b.

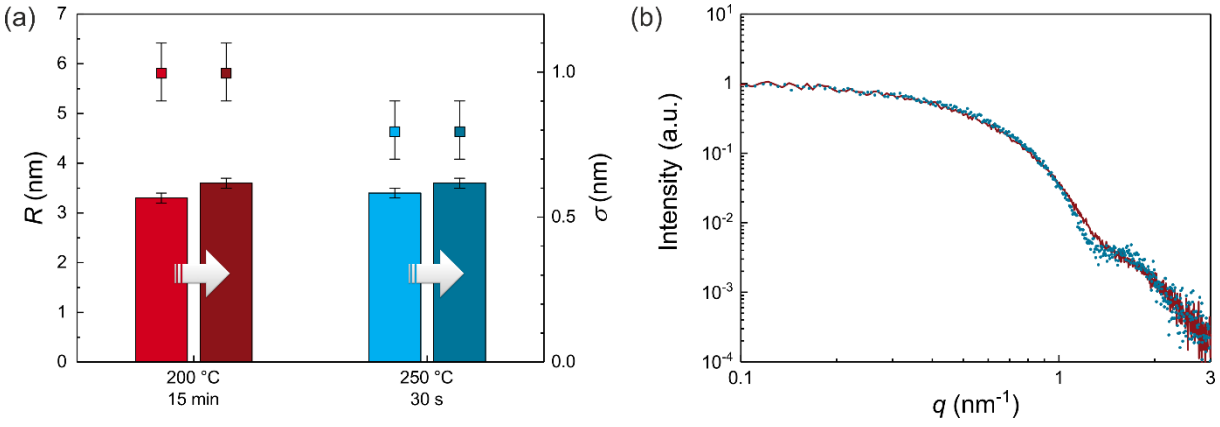

Figure 20. (a) Mean radii R_V (bars) and their distribution widths σ (symbols). Arrows indicate parameters before and after purification of the particles. (b) Overlay of the scattering curves from particles synthesized for 15 min at 200 °C and for 30 s at 250 °C with microwave heating after purification (solid red line and dotted blue line, respectively). The curves were normalized to unity for better comparison.

Thus, we can state that the particle synthesis in a microwave can be effectively accelerated by increasing the temperature by 50 K without affecting the size distribution parameters.

The Arrhenius equation describes the relation between the reaction rate constant k_i and the temperature T_i via the pre-exponential factor A, energy of activation E_a, and the universal gas constant R as $k_i = A \exp\left[-\frac{E_a}{RT_i}\right]$. At two different temperatures, T_2 and T_1, the corresponding reaction rate constants are $k_1 = A \exp\left[-\frac{E_a}{RT_1}\right]$ and $k_2 = A \exp\left[-\frac{E_a}{RT_2}\right]$. The ratio of the reaction rate constants is $\frac{k_2}{k_1} = \exp\left[\frac{E_a}{R}\left(\frac{1}{T_1} - \frac{1}{T_2}\right)\right]$ from which the activation energy can be estimated as

$$E_a = \frac{R\, T_1 T_2 \ln(k_2/k_1)}{T_2 - T_1} \tag{16}$$

For an increase of the temperature from T_1 = 200 °C to T_2 = 250 °C, we found a decrease in the reaction time of $t_2 \approx t_1/30$. Because the educts and the products did not change for the different reaction times t_i, we assume that the product of the reaction time and rate is the same for both syntheses. Hence, we can estimate that the ratio of the reaction times t_1/t_2 is the same as the ratio of the reaction rate constants k_2/k_1. According to equation (16), we calculated an activation energy of $E_a \approx 139$ kJ mol^{-1}. This value seems to be reasonable, because it is between the reported dissolution energy of 69 kJ mol^{-1} for silver nanoparticles[96] and the activation energy of 174 kJ mol^{-1} reported for the growth of silver nanoparticles.[97]

In nanoparticle synthesis, the exact tuning of the particle parameters is of high importance. As the silver particle formation is completed after 3 min at 300 °C, the question arises whether it is possible to fine-tune the particle radius with a subsequent growth phase. Because of increasing pressure values at 300 °C, the temperature was lowered to 250 °C after 3 min to allow further growth of the particles for 12 min.

Indeed, larger particles with R_V = 7.1 ± 0.1 nm and σ = 2.6 ± 0.1 nm were obtained (Figure 21a). As shown above, the conversion of silver ions to elementary silver is completed after 3 min at 300 °C, forming particles with R_V = 4.1 ± 0.1 nm and σ = 1.1 ± 0.1 nm. Therefore, we conclude that the 12 min incubation at 250 °C led to a particle growth by approximately 3 nm, which was accompanied by a broadening of the size distribution. It is not clear whether this growth is caused by Ostwald ripening or coalescence, because it is difficult to distinguish these processes from each other.[98] According to LaMer's principle of particle formation, the

separation of nucleation and particle growth is a crucial factor for the production of particles with a narrow size distribution. To achieve a better separation of the initial synthesis at 300 °C and the subsequent growth phase, a short cooling to 45 °C was added. The resulting particles were slightly smaller (R_V = 6.2 ± 0.1 nm) and have a narrower size distribution width (σ = 2.1 ± 0.1 nm) than those obtained without intermediate cooling (Figure 21a). Unfortunately, aggregates were present after the transfer from ethylene glycol to water. This is reflected in R_h values of 20.1 ± 0.4 nm (without cooling) and 25.5 ± 2.2 nm (with cooling) as well as PDIs of 0.33 ± 0.02 and 0.30 ± 0.01, respectively. We assume that this is mainly caused by a partial decomposition of the stabilizing PAA. Interpretation of the SAXS data shows that a mixture of primary particles and aggregates is present after transfer. In the first case (12 min incubation at 250 °C), the primary particles display a core radius of 7.8 ± 0.1 nm and the radius of the aggregates amounts to 17.9 ± 0.3 nm (Figure 21b).

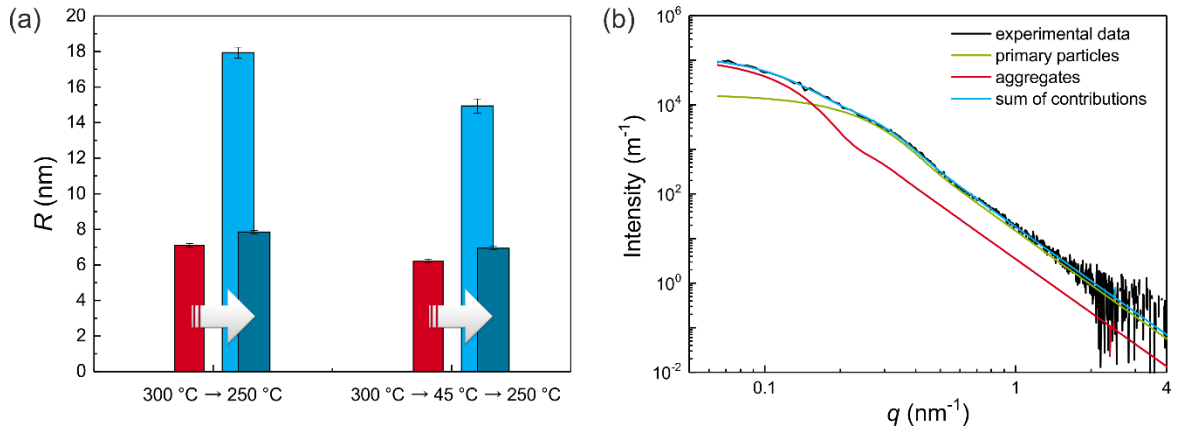

Figure 21. (a) Comparison of the mean radii R_V after subjecting the reaction mixture to the denoted temperature sequence, before (left red bar for each temperature sequence) and after purification (right bars for each temperature). After purification, the particle systems consist of a mixture of primary particles (bright blue bar in the middle) and aggregates (dark blue bar on the right). (b) Scattering curve of the particles produced by the temperature sequence 300 °C → 45 °C → 250 °C (black), and the curve fit (blue) composed of the contribution of primary particles (green) and aggregates (red).

From the relative intensities of the scattering contributions, we calculate a number ratio of primary particles to aggregates of 60 to 1. From the volume ratio of aggregates to primary particles, we estimate an aggregation number of about 12 primary particles per aggregate. In the second case (added short cooling to 45 °C), the primary particles display a core radius of 6.9 ± 0.1 nm, and the radius of the aggregates is 14.9 ± 0.4 nm. The relative intensities of the

scattering contributions allow the determination of the number ratio of primary particles to aggregates of 44 to 1. The volume ratio of aggregates to primary particles leads to an aggregation number of about 10 primary particles per aggregate.

Therefore, we conclude that silver nanoparticles can be further grown by a post-synthetic heating step. A remaining crucial challenge lies in gaining more control over the dispersity, which can at least be reduced by intermediate cooling between particle synthesis and growth phase.

Author contributions: The general concept of the study was set up by me. Syntheses of nanoparticles were done by Patrick E. J. Saloga. SAXS measurements were performed by Patrick E. J. Saloga. We interpreted the SAXS data with main contributions coming from my side. Patrick E. J. Saloga and I discussed the results and wrote the manuscript together with equal contributions. All authors contributed to the final version of the manuscript.

5.1.3 Inter-Laboratory Comparison

This chapter is based on the paper "Nanoparticle size distribution quantification: results of a small-angle X-ray scattering inter-laboratory comparison", which has been partially modified and is reprinted in its original form in Appendix A.3.

Today, a high variety of analytical methods are available. Many new techniques are being developed, especially for the characterization of nanomaterials, such as the single particle tracking analysis.[99] With this evolution of new methods, the question of the reliability of analytical techniques has seen a renewed importance. This question can be answered with an inter-laboratory comparison, comparing results inferred from measurements of identical samples using different measuring devices. There are only a few inter-laboratory comparisons for the analytical methods used in nanotechnology to date, such as for single particle inductively coupled plasma mass spectrometry (SP-ICP-MS)[100-101] and transmission electron microscopy.[102] Furthermore, only one inter-laboratory comparison exists for small-angle neutron scattering (SANS),[103] and there are none at all for SAXS. SAXS is a method for the quantification of nanostructures and is particularly sensitive to the smaller end of the nanoscale. It has been shown that results from SAXS agree well with findings from electron microscopy,[104-105] and comparisons of the results of different SAXS instruments demonstrate its inter-instrument reproducibility.[106-107]

A suitable sample must be chosen for an inter-laboratory comparison. For SAXS, this sample should exhibit an appropriate stability, a limited size dispersity, a size in the sub-20 nm region, and a reasonable scattering power (combination of contrast and concentration). All these requirements are fulfilled by our PAA-stabilized silver nanoparticles which where, thus, used for the investigation of the practical precision and accuracy of SAXS.

This work provides the first inter-laboratory comparison of the measurement of nanoparticle size distributions with SAXS. The received measurements are anonymized and evaluated by three substantially different analysis methods. On this basis, we are able to estimate how precise the SAXS method is for the determination of sizes of nanoparticles in the sub-20 nm range.

The NP_{PAA} were measured using 24 different SAXS instruments, revealing a high resistance of the particles against synchrotron radiation. No time-correlation effect was

observed in the samples for the duration of the comparison. This shows that the sample was stable throughout the experiment, and also stable against environmental changes encountered during shipping.

The received measurement protocols demonstrated that the laboratory procedures for SAXS measurements varied greatly between the participants. For instance, the type of sample containers differed between reusable containers or flow-through capillaries and non-identical containers for the sample and background measurements. Therefore, different data correction procedures have been applied. Both variations in data collection and correction can affect the resulting data.[108] Nevertheless, the first comparison of the received and pre-processed data shows a high similarity with only two outliers. Details of the quantification of the size distributions were produced by the utilization of three different data evaluation methods: (i) the GIFT, implementing an indirect Fourier transformation (IFT),[74] (ii) SASfit,[72] using a model fit of spheres with a lognormal size distribution, and (iii) McSAS,[73] implementing a Monte Carlo determination of size distributions assuming spherical scattering objects.

The IFT method does not provide the population modes, which results in a quantification of the distribution by fitting with a lognormal function. The resulting distribution of IFT are slightly asymmetric around their maxima, with the tail decaying more slowly towards larger radii. Hence, symmetric function like the Gaussian profile cannot be used, whereas a lognormal function is suitable. The employed function is written in equation (17). A is defined as the area of the size distribution, w as the scale parameter determining the width of the size distribution, and R_0 as the median radius. The median radius can be converted to the mean radius R and its standard deviation σ using equation (18) and (19), respectively.

$$f(R) = \frac{A}{\sqrt{2\pi} w R} e^{\left[-\frac{\ln\left(\frac{R}{R_0}\right)}{2w^2}\right]} \tag{17}$$

$$R = R_0 \, e^{2w^2} \tag{18}$$

$$\sigma = R_0 \sqrt{e^{2w^2} - e^{w^2}} \tag{19}$$

The fitting procedure was applied for all data sets minus the two outliers to determine the number-weighted mean radius $R_{n,IFT}$ and the mean width $\sigma_{n,IFT}$ (Figure 22). The mean values amount to $R_{n,IFT}$ = 2.82 ± 0.04 nm and $\sigma_{n,IFT}$ = 0.67 ± 0.02 nm. The box plot depicted in Figure 22a

shows that 90% of the values for the radius are within 0.1 nm, which is surprisingly low for a sample with a dispersity of approximately 20 %.

The IFT data evaluation was repeated for the calculation of the volume-weighted radius and its standard deviation, which results in $R_{v,IFT}$ = 3.22 ± 0.04 nm and $\sigma_{v,IFT}$ = 0.71 ± 0.05 nm (Figure 22**Figure 22**). In this case, the box plot also reveals a spread of the values on a 90 % interval within 0.1 nm. In comparison with the number-weighted radii, the volume-weighted ones are significantly larger due to the dispersity of the sample. For monodisperse systems, R_n would be identical to R_v. The precision of the determined radii is surprising for a size-disperse sample. Therefore, we assume that the data evaluation via the IFT method is insensitive to variations between the data sets of the participants and their instruments. Nonetheless, the IFT data evaluation method includes a smoothness constraint on the resulting size distribution, which may artificially constrict the results, and thus may lead to an overestimated degree of precision. Therefore, we investigated the influence of the data evaluation method by comparing it with two other procedures.

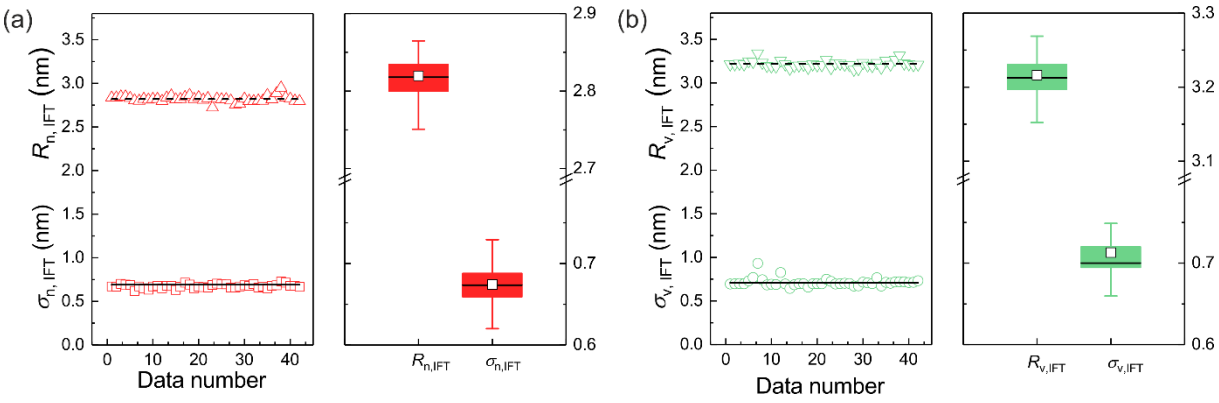

Figure 22. Results of data evaluation using the IFT method: (a) Left panel: number-weighted radii, $R_{n,IFT}$, and widths of the size distribution, $\sigma_{n,IFT}$, as a function of the data set number (triangles and squares, respectively). Mean values of $R_{n,IFT}$ and $\sigma_{n,IFT}$ are marked with horizontal lines. Right panel: box plot depicting the distribution of $R_{n,IFT}$ and $\sigma_{n,IFT}$ from the measurements. The horizontal line that forms the top of the box is the 75th percentile (Q_1). The horizontal line that forms the bottom is the 25th percentile (Q_3). The horizontal line within the box corresponds to the median value, and the square corresponds to the mean value. The whiskers represent lower 5 and 95% values. (b) Left panel: volume-weighted radii, $R_{v,IFT}$, and widths of the size distribution, $\sigma_{v,IFT}$, as a function of the data set number (triangles and spheres, respectively). Mean values of the data sets $R_{v,IFT}$ and $\sigma_{v,IFT}$ are shown as horizontal lines. Right panel: box plot of the distribution of $R_{v,IFT}$ and $\sigma_{v,IFT}$ from the measurements.

We used SASfit as a classical curve-fitting procedure, with an assumption of a mathematical form of the distribution, and McSAS[73] as a Monte Carlo fitting program (a minimal assumption method). The results of this comparison are depicted in Figure 23 and the data is summarized in Table 4. In its current implementation, SASfit only provides estimates of the number-weighted size distribution. As a prerequisite, a lognormal size distribution has been chosen for data evaluation. From the box plots in Figure 23, it can be seen that the mean radii and widths are similar for all three data evaluation procedures. To test whether the mean values are the same, we employed analysis of variance (ANOVA) at the 0.05 level. This reveals that the number weighted radii are not equal (with a data mean of 2.76 ± 6 nm). Furthermore, the volume-weighted mean radii $R_{v,IFT}$ and $R_{v,McSAS}$ differ significantly according to ANOVA (with a mean of 3.20 ± 4 nm). The number-weighted mean widths retrieved from IFT, SASfit and McSAS are significantly different (data mean is 0.65 ± 1 nm). In contrast, the volume-weighted mean widths $\sigma_{v,IFT}$ and $\sigma_{v,McSAS}$ are equal (data mean is 0.71 ± 1 nm). From the ANOVA tests, we conclude that the values for R_n, R_v and σ_n are dependent on the type of evaluation method. On the contrary, σ_v is independent of the choice of the method. However, the spread of R_n, R_v, σ_n and σ_v is smaller for IFT and SASfit in comparison to McSAS. The reason for this is that McSAS produces fewer assumptions than IFT and SASfit.

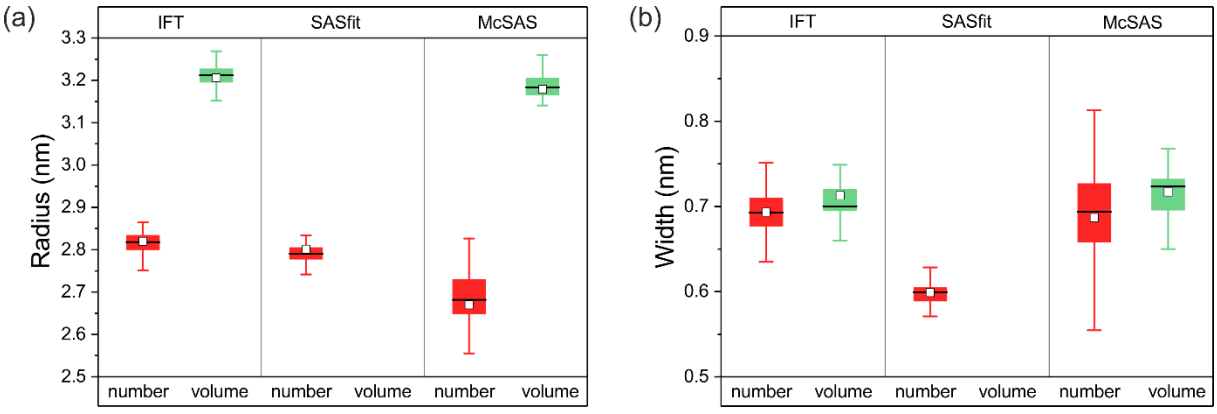

Figure 23. Comparison of number- and volume-weighted (a) radii and (b) widths derived from IFT and the SASfit and McSAS programs. Number-weighted values are in red, volume-weighed in green. The top and bottom of the box delineate the 75th (Q_1) and 25th (Q_3) percentiles. The horizontal line within the filled box is the median value, and the square represents the mean value. The whiskers correspond to lower 5 and 95% limits.

In general, the values for the interquartile ranges for all three methods are small enough for us to recommend all three for data evaluation purposes. The consistent results of

the IFT method prove that this data evaluation method is the most suitable for the quantification of the size distribution of the particular sample of NP_{PAA}. The form-free nature of McSAS resulted in wider interquartile ranges, which leads to the suggestion that this method is suitable for samples where little a priori knowledge about the investigated sample is given. The use of SASfit is recommended if an estimate of the size distribution form is known.[72] In ambiguous situations, a comparison of the results of more than one data evaluation method should be done.

Table 4. Summary of the statistical data of the inter-laboratory comparison.

	IFT				SASfit [a]		McSAS			
Weighting	Number		Volume		Number		Number		Volume	
Statistical value	R_n (nm)	σ_n (nm)	R_v (nm)	σ_v (nm)	R_n (nm)	σ_n (nm)	R_n (nm)	σ_n (nm)	R_v (nm)	σ_v (nm)
Mean	2.82	0.67	3.22	0.71	2.80	0.60	2.67	0.69	3.18	0.72
Width, SD	0.04	0.02	0.04	0.05	0.07	0.02	0.16	0.08	0.07	0.06

[a] The SASfit software provides estimates of the number-weighted particle properties only.

Twenty-eight of the received data sets were provided on an absolute scale, which enables the determination of the particle concentration.[109] For this purpose, absolute calibration intensity standards such as water[76] or glassy carbon[110] are required. SASfit provides an estimate of number-weighted particle concentrations, which can be converted to particle mass concentrations.[72] McSAS provides estimates of volume fractions, which can be directly converted to mass concentrations.[73] In contrast, in the IFT method, the calculation of particle concentrations is not implemented.[111]

For the determination of the particle concentrations, the scattering contrast was calculated to be $\Delta\rho = 6.8 \times 10^{-3}$ nm^{-2} for silver in water, calculated for an energy of 8 keV. The resultant volume concentrations were multiplied with the bulk density of silver (10.49 g cm^{-3}) to obtain the mass concentrations.

The number-weighted and volume-weighted concentrations derived by SASfit and McSAS are depicted in Figure 24. The mean number-weighted concentration determined by SASfit was $c_{n,SASfit} = 4.20 \pm 0.73 \times 10^{-6}$ mol L^{-1} and the mean volume-weighted concentration determined by McSAS was $c_{v,McSAS} = 2.86 \pm 0.31$ g L^{-1}. Conversion of the number concentration

to volume concentration results in $c_{v,SASfit}$ = 3.00 ± 38 g L^{-1}. The conversion of the volume-weighted concentration $c_{v,McSAS}$ to the corresponding number-weighted distribution results in $c_{n,McSAS}$ = 3.37 ± 0.37 × 10^{-6} mol L^{-1}. ANOVA tests revealed that the volume-weighted concentrations are equal at the 0.05 level, whereas the number-weighted ones are significantly different. This indicates that a conversion of number-weighted concentrations to volume-weighted ones results in appropriate results. However, it is generally not recommended to convert the volume-weighted concentrations to number-weighted ones due to the discrepancy of the numerical nature of this operation.

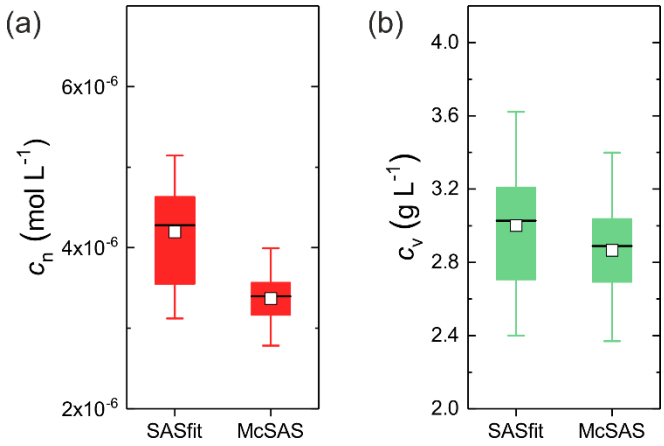

Figure 24. (a) Particle number concentration from SASfit and McSAS, with the latter converted from the volume concentration. (b) Particle mass concentration as converted from the SASfit number concentration in (a) and as a direct determination from McSAS. The white squares and horizontal lines in the box charts are the mean and median values, respectively. The lower and upper values of the box represent the quartiles Q_1 and Q_3; the upper and lower whiskers are the 5 and 95% levels.

Both data evaluation procedures, McSAS and SASfit, produce consistent values for the particle concentration. The uncertainty in the determination of the concentration of silver nanoparticles is approximately 10 %, and therefore SAXS presents a suitable alternative to other methods like ICP-MS, where also non-particulate, ionic species would be detected.

Author contributions: Syntheses of nanoparticles were done by me. Data evaluation of the SAXS measurements was performed by Brian R. Pauw, Andreas F. Thünemann and me, with main contribution from Brian R. Pauw and Andreas F. Thünemann. We interpreted the SAXS data and we wrote the manuscript together, with main contribution coming from Brian R. Pauw. All authors contributed to the final version of the manuscript.

5.2 Applications of Silver Nanoparticles

5.2.1 Catalyst in the Reduction of 4-Nitrophenol

This chapter is based on the paper "Catalytic Reduction of 4-Nitrophenol Using Silver Nanoparticles with Adjustable Activity", which has been partially modified and is reprinted in its original form in Appendix A.1.

We investigated the catalytic properties of PAA-, GSH-, and BSA-stabilized silver nanoparticles by utilizing the reduction of 4-nitrophenol to 4-aminophenol with sodium borohydride. This reaction functions as a "gold standard" for investigating the catalytic properties of nanoparticles made of silver, gold, palladium, etc.[112] For ease of comparison, we used the same experimental conditions as applied by Fenger et al.,[78] who investigated the size dependency of the catalytic activity of CTAB-stabilized gold nanoparticles. They found that not as expected the smallest, but medium-sized nanoparticles with a radius of 6.5 nm were the most efficient. These particles display a higher catalytic activity than smaller (5 and 2.8 nm) and larger particles (14 and 28 nm). Therefore, the catalytic activity of metal nanoparticles does not necessarily increase with decreasing size, potentially due to the strong curvature of the surface of very small particles. This means that the small size of our silver particles is not a guarantee for a high catalytic efficiency.

We started the investigation of our nanoparticles by adding NP_{PAA} (12.5 nmol silver) to a solution containing 4-nitrophenol and sodium borohydride. Sodium borohydride leads to a basic pH and a yellow solution of 4-nitrophenolate which is stable for hours if no catalyst is added. We found that the yellow color of the solution decolorizes within seconds after addition of the nanoparticles. After a reaction time of 20–30 s, no 4-nitrophenol could be detected by UV/vis spectroscopy, which approximately corresponds to a rate constant of $0.3 \pm 0.1\ s^{-1}$. From this number, we estimate that the NP_{PAA} are about 60-fold higher catalytically active than the 6.5 nm gold nanoparticles of Fenger et al., which show a rate constant of $(6.1 \pm 0.1) \times 10^{-3}\ s^{-1}$.

With the surprisingly high catalytic activity of NP_{PAA}, we focused on the catalytic properties to quantify the reaction kinetics with UV/vis spectroscopy. Therefore, we reduced the amount of added NP_{PAA} stepwise from 12.5, 6.2, 3.2 to 1.6 nmol silver to monitor the

decolorization more precisely. The resulting UV/vis spectra of the catalytic process of 4-nitrophenolate to 4-aminophenolate after adding NP_{PAA} are shown in Figure 25a. Therein, the main peak of 4-nitrophenolate ions at 400 nm is decreasing with reaction time, while the second peak at 300 nm of 4-aminophenolate is slowly increasing. Two isosbestic points are visible at 280 and 314 nm.

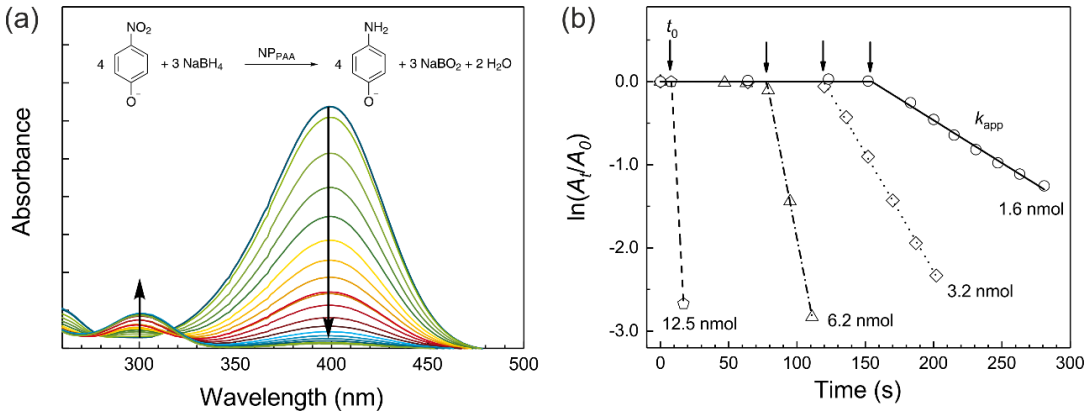

Figure 25. (a) UV/vis spectra of the catalytic process of 4-nitrophenolate to 4-aminophenolate in water after adding NP_{PAA} (1.6 nmol silver). The absorbance band at 400 nm of 4-nitrophenolate is decreasing with reaction time, while the band at 300 nm of 4-aminophenolate is increasing (indicated by arrows). (b) Comparison of the catalytic activity of different amounts of NP_{PAA}: 12.5, 6.2, 3.2, and 1.6 nmol silver. The induction periods, t_0, are indicated by arrows; the apparent reaction constants, k_{app}, correspond to the linear slope in each curve. The lines are fit curves from applying equation (20).

The time dependence of the absorbance of 4-nitrophenolate ions at 400 nm is characterized by an induction period t_0, where the absorbance is constant, followed by a linear decrease (Figure 25b). The absorbance can therefore be quantified by t_0 and an apparent reaction constant, k_{app}, as

$$\ln\left(\frac{A}{A_0}\right)(t) = 0 \quad \text{for } t \leq t_0$$
$$\ln\left(\frac{A}{A_0}\right)(t) = \ln\left(\frac{A}{A_0}\right)(0) - k_{app}t \quad \text{for } t > t_0 \tag{20}$$

The induction periods are obtained as

$$t_0 = \frac{\ln\left(\frac{A}{A_0}\right)(0)}{k_{app}} \tag{21}$$

The absorbance of 4-nitrophenolate before NP_{PAA} has been added corresponds to A_0. The ratio A/A_0 is identical to the ratio of the concentration of 4-nitrophenolate at a time t, to its

concentration before the reaction starts, i.e., $A/A_0 = c/c_0$. Therefore, equation (20) quantifies the relative change of the concentration of 4-nitrophenolate. Typical results of fitting equation (20) to the experimental $\ln(A/A_0)(t)$ curves are shown in Figure 25b. The induction period t_0 decreases and k_{app} increases for increasing amounts of added NP_{PAA} (1.6, 3.1, 6.2, and 12.5 nmol silver). The relationship of the induction period as a function of the concentration of NP_{PAA} is nonlinear and was approximated by a quadratic polynomial (Figure 26a):

$$t_0 = (214 \pm 23)\ \mathrm{s} - (9.2 \pm 1.6) \cdot 10^5\ \mathrm{L\ s\ g^{-1}} \cdot c_{Ag} + (1.0 \pm 0.2) \cdot 10^9\ \mathrm{L^2\ s\ g^{-2}} \cdot c_{Ag}^2 \quad (22)$$

Gu et al.[113] reported an induction period in all cases they studied when using gold/palladium alloy nanoparticles as catalyst. In their studies t_0 amounts to approximately 20 s.[114] They hypothesized that t_0 is related to a surface restructuring of the nanoparticles and supported this explanation with a study on gold nanoparticles.[115] This theory is still under debate. Also, silver nanoparticles display an induction period, but in literature it is typically not discussed in detail. For example, a t_0 of 103 s was reported by Walker and Zaleski,[116] who embedded silver nanoparticles in the corona of magnetic nanoparticles. The largest t_0 of silver nanoparticles that we are aware of in literature is approximately 1900 s, reported for Ag@ $SiO2@Ag_{seeds}$ particles by Lee and Jang.[117] There, the catalytic degradation of rhodamine B was chosen as model reaction. Hence, the presence of an induction period seems to be a general phenomenon in nanoparticle catalysis, but is hardly investigated. We speculate that a low reproducibility of t_0 and the absence of reasonable physical understanding may explain this gap. In our opinion, t_0 is an important parameter for rating and understanding nanoparticles' catalytic potential and, therefore, should be considered more closely in future studies.

The catalytic activity is strongly connected to the apparent reaction constant, k_{app} and its dependence on the amount of used particles. It has to be expected that k_{app} increases with increasing amount of added NP_{PAA}. More particles correspond simply to a larger total surface area of the catalyst and the availability of more active sites. A priori, we expected a linear increase of k_{app} with the amount of NP_{PAA}. The linear approximation of $k_{app} = 436 \pm 23\ \mathrm{L\ s^{-1}\ g^{-1}} \times c_{Ag}$ is sufficiently fulfilled (Figure 26b). Lara et al.[118] recently reported also on a linear increase of k_{app} with increasing catalyst concentration, but for a Fe_3O_4@dextran/Pd nanoparticle system. However, many reported studies, use only a single concentration, making it impossible to draw further conclusions with respect to linearity.

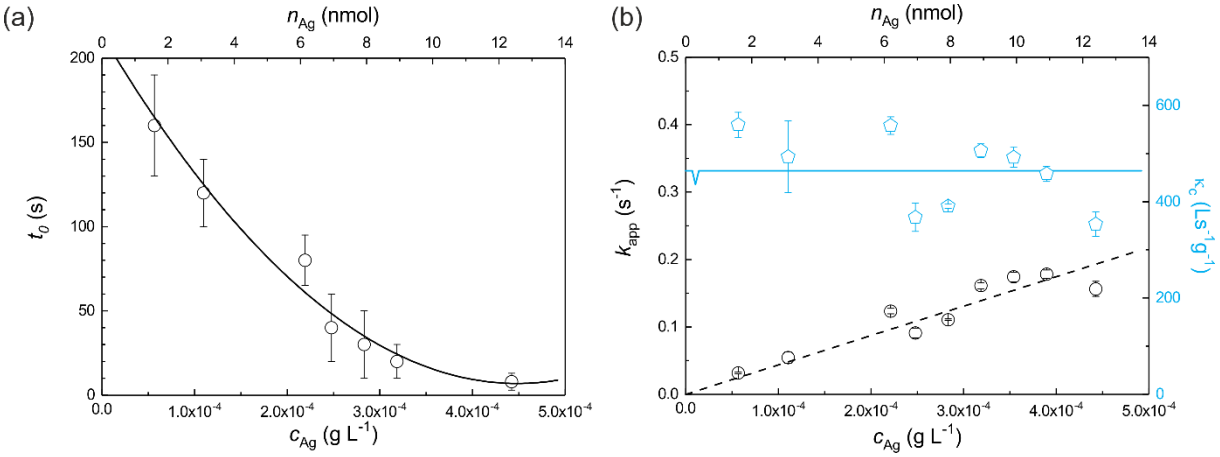

Figure 26. (a) Induction period t_0 as a function of the concentration of NP$_{PAA}$ (circles) and its approximation by a quadratic polynomial according to equation (22) (solid black line). (b) Apparent reaction constant k_{app} as a function of the added amount of NP$_{PAA}$ (circles) and its approximation by a linear relationship (dashed black line): $k_{app} = 436 \pm 23$ L s^{-1} g^{-1} × c_{Ag}. The reaction parameter κ_c as a function of the concentration (blue pentagons) can be approximated by a constant of $\kappa_c = 464 \pm 26$ L s^{-1} g^{-1} (solid blue line).

Despite the widespread use of the 4-nitrophenol reduction, a direct comparison of our data with data from literature is complicated by the variety of catalytic parameters that have been reported. Most of these studies simply report on k_{app} as summarized in a recent review by Zhao et al.[112] However, k_{app} is dependent on the amount of silver nanoparticles used in the reaction. Therefore, the "activity parameter" κ is in use. Parameter κ is often normalized with respect to the total mass of the catalyst added, κ_m, which ignores the reaction volume and consequently the catalyst concentration.[119] Thus, a second version of the "activity parameter", κ_c, is in use, which takes the mass of the catalyst and the volume of the reaction solution into account. To our opinion, κ_c, is the most appropriate parameter for comparison of data from different studies.[118] For clarification, κ_c corresponds to the ratio of k_{app} to the concentration of the metal catalyst in mass per volume, i.e., $[\kappa_c]$ = L g^{-1} s^{-1}. To ensure not to overestimate the catalytic activity of NP$_{PAA}$, the mean value of $\kappa_c = 464 \pm 26$ L s^{-1} g^{-1} is used in the following (derived from Figure 26b).

The determination of the activity parameter of NP$_{GSH}$ gives a value of 77.6 ± 0.9 L s^{-1} g^{-1}, which was measured for adding 1.6 nmol of silver. An increase of the used amount of silver to 12.5 nmol was necessary to detect a significant catalytic activity of 3.47 ± 0.50 L s^{-1} g^{-1} for NP$_{BSA}$. A direct comparison of the experimental curves and the resulting activity parameters of NP$_{PAA}$, NP$_{GSH}$, and NP$_{BSA}$ is shown in Figure 27.

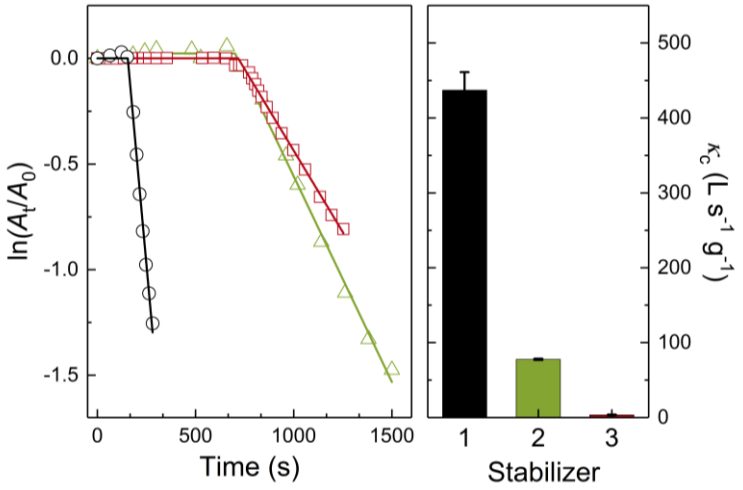

Figure 27. Comparison of the catalytic activity of NP_{PAA}, NP_{GSH}, and NP_{BSA} (black, green, and red, respectively). Left panel: time dependence of the absorbance of 4-nitrophenolate ions at 400 nm. Solid lines display the linear sections, from which the reaction constants k_{app} were determined. The added amounts of NP_{PAA} and NP_{GSH} were 1.6 nmol, while of NP_{BSA} 12.5 nmol was added. Right panel: resulting activity parameters of the particles.

We selected a few important studies from the literature for comparison with our findings. Their catalytic properties are summarized together with our data in Table 5. First of all, Baruah et al.[119] reported on silver nanoparticles with a radius of 9 nm stabilized by cationic polynorbornenes. They found a κ_m of 1375 s^{-1} g^{-1}, which they classified as significantly higher than other systems reported in literature before 2013. This value corresponds to a normalized activity parameter of κ_c = 1.375 L s^{-1} g^{-1}. As far as we know, this is still the highest published value for freely suspended silver particles. Quite recently, normalized activity parameters have been summarized by Zhang et al.[120] They reported a value of κ_c = 4.38 ± 0.37 L s^{-1} g^{-1} for their silver nanoparticles which were stabilized in suspension on a support of sulfhydryl-functionalized poly(glycidyl methacrylate) microspheres. They classified them as the silver nanoparticles with the highest known κ_c for composite particles. Zheng et al.[31] reported on silver nanoparticles wrapped by an exopolysaccharide with radii of 2.5 nm and κ_m = 15.75 s^{-1} g^{-1}, which corresponds to κ_c = 0.047 L s^{-1} g^{-1}. This is an unexpectedly low value considering the small particle size. A possible explanation could be the structure of this system. The structure model consists of an aggregate of exopolysaccharide chains with embedded silver nanoparticles forming a nanocomposite with a hydrodynamic radius of approximately 150 nm. The reaction components must diffuse a relatively long path through exopolysaccharide aggregates before they reach the silver particles' surface. We speculate that

this diffusion is the crucial step that lowers the catalytic activity. Patra et al.[121] provided a comparison of selected silver nanoparticles with respect to their catalytic activity. They studied silver nanoparticles embedded in porous poly(styrene) beads. The radii of the pores and the silver particles are estimated to be below 5 nm. The reported activity parameter is κ_m = 974.07 s^{-1} g^{-1}, which corresponds to κ_c = 1.95 L s^{-1} g^{-1}. This κ_c is surprisingly high and indicates that the surface of the silver nanoparticles is catalytically well accessible for the reactants. However, this fast reaction starts only after 1000 s. Prior to that, an induction period of 400−500 s was observed followed by a period of slow reaction kinetics for several hundreds of seconds. It seems that the morphology of their system provides complex nano-confinement effects which affect the reaction kinetics.

To the best of our knowledge, the κ_c for NP_{PAA} is the highest value reported for silver nanoparticles so far. Substantially higher values are only found for particles with different core materials, such as palladium nanoparticles. Lara et al.[118] reported of palladium nanoparticles with a radius of 3.9 nm and κ_c = 3650 L s^{-1} g^{-1}. The palladium nanoparticles were located on a dextran coating of magnetite particles. To understand why NP_{PAA} display such a high catalytic activity, surface area and accessibility must be considered. The surface area of a silver nanoparticle with a radius of 3 nm is 10^3 m^2 cm^{-3}, and the specific surface is 95 m^2 g^{-1}, assuming that the particles have the same density as silver in bulk form. The catalytic activity of the silver surface can now be normalized by the specific surface resulting in κ_c/S_a = 4.58 ± 0.25 L m^{-2} s^{-1} (NP_{PAA}), 0.81 ± 0.01 L m^{-2} s^{-1} (NP_{GSH}), and 0.036 ± 0.005 L m^{-2} s^{-1} (NP_{BSA}). The S_a and κ_c/S_a values are summarized for all systems in Table 5.

Compared with the κ_c/S_a values of the other catalytic systems, it becomes clear that even when normalized to the specific surface area the NP_{PAA} particles are around 2 orders of magnitude more active than the other silver particle based systems. Only the palladium system has a much higher value of κ_c/S_a = 151 L m^{-2} s^{-1}, and for a gold nanoparticle system the value is 0.5 L m^{-2} s^{-1}. We conclude that the particle surface of NP_{PAA} is well accessible for the reactants through their water-swollen PAA shell, probably similar to the dextran shell of the palladium particles in the study of Lara et al.[118]

Table 5. Comparison of parameters of the catalytic reduction of 4-nitrophenolate to 4-aminophenolate from this study and literature. Listed are temperature, T, particle radius, R_c, silver concentration, [Ag], apparent rate constant of the reaction, k_{app}, activity parameter, κ_c, specific surface area of the particles, S_a, and the activity parameter normalized by the specific surface area, κ_c/S_a.

Nano-particles	T (°C)	R_c (nm)	[Ag] (10^{-3} g L^{-1})	k_{app} (10^{-3} s^{-1})	κ_c (L s^{-1} g^{-1})	S_a (m^2 g^{-1})	κ_c/S_a (L m^{-2} s^{-1})
NP_{PAA}	22	3.0	0.035	15.46 ± 0.84	436 ± 24	95	4.58 ± 0.25
NP_{GSH}	22	3.0	0.219	17.04 ± 0.19	77.7 ± 0.9	95	0.81 ± 0.01
NP_{BSA}	22	3.0	0.442	1.53 ± 0.22	3.5 ± 0.5	95	0.036 ± 0.005
Ag[a]	25	9	4.0	5.5	1.375	31	0.01
Ag[b]	RT	8.5	0.9	3.94 ± 0.33	4.38 ± 0.37	17	0.07
Ag[c]	25	2.5	0.0267	1.26	0.047	114	0.0001
Ag[d]	25	< 5	0.0139	974.07	1.948	57	0.01
Pd[e]	15	3.9	0.0269	0.092	3650	6.3	151
Au[f]	25	6.5	0.807	0.0061	7.55	4	0.5

[a]Silver nanoparticles AgNP-PG-5K stabilized with a cationic polynorbornene, M_w = 5000 g mol^{-1}.[119] [b]Silver nanoparticles AgNP@PGMA-SH stabilized with sulfhydryl functionalized poly(glycidyl methacrylate) microspheres.[120] [c]Silver nanoparticles dispersed by a exopolysaccharide.[31] [d]Silver nanoparticles embedded in porous poly(styrene) beads.[121] [e]Palladium nanoparticles on the surface of Fe_3O_4@dextran particles.[118] [f]Gold nanoparticles stabilized with cetyltrimethylammonium bromide.[78]

Some researchers prefer to use the turnover frequency, k_{TOF}, instead of the activity parameter to quantify the catalytic activity of nanoparticles. The turnover frequency is the number of reactant molecules (4-nitrophenol) that 1 g of catalyst (Ag) can convert into product (4-aminophenol) per time.[122] Therefore, the turnover frequency for a first-order reaction can be calculated from the activity parameter by

$$k_{TOF} = \kappa_c \cdot c_{e,0} \cdot e_c^{-t\, c_c\, \kappa_c} \tag{23}$$

The c_c is the concentration of the catalyst in g L^{-1}, and $c_{e,0}$ corresponds to the concentration of 4-nitrophenol at t = 0 in molecules L^{-1} (without induction period). In the limit of short times we get

$$k_{TOF} = \kappa_c \cdot c_{e,0} \tag{24}$$

The resulting k_{TOF} values are 28.78 ± 1.58 mmol g^{-1} s^{-1} for NP_{PAA}, 5.12 ± 0.06 mmol g^{-1} s^{-1} for NP_{GSH}, and 0.23 ± 0.03 mmol g^{-1} s^{-1} for NP_{BSA}. More clearly, these values correspond to reaction frequencies of 3.10 ± 0.17 4-nitrophenol molecules per silver atom and second for NP_{PAA}, 0.552 ± 0.006 for NP_{GSH}, and 0.025 ± 0.004 for NP_{BSA}.

Author contributions: Syntheses of nanoparticles were done by me. Furthermore, I performed the first catalysis experiments. The repetition of these experiments for reproducibility was done by Mona Heinrich. Catalytic data was evaluated by me with the help of Andreas F. Thünemann. Andreas F. Thünemann and I discussed the results, and wrote the manuscript together with main contribution coming from my side. All authors contributed to the final version of the manuscript.

5.2.2 Fluorescent Silver Nanoparticles for Biological Application

This chapter is based on the manuscript "Fate of Fluorescence Labels – Their Adsorption and Desorption Kinetics to Silver Nanoparticles", which has been partially modified and is reprinted in its original form in Appendix A.4.

Regarding biological investigations, a fluorescent marker is often used to monitor transport and possible degradation of silver nanoparticles.[123] For this purpose, the particles' ligand shell is either exchanged for a fluorescent stabilizer or the ligand is modified to include an emissive marker. A major challenge of fluorescence-labeled nanoparticles in biological application is: Do we see the fluorescent marker which is attached to the particle or the liberated fluorescent marker? Kreyling et al.[124] observed a partial loss of the ligand in physiological environment for gold nanoparticles which are coated by a thiol-functionalized polymer – a ligand which is known for a strong binding.[125-126] Knowledge concerning the binding kinetics is important, because these markers are typically not covalently bound to the particles. Their adsorption and desorption onto the nanoparticles' surface is a dynamic process. Overall, relatively little is known about the binding behavior of fluorescent markers to nanoparticles, and therefore it is the aim of this study to contribute to this field.

Hence, we provide an investigation of the binding properties and kinetics of two different fluorescent ligands on small silver nanoparticles (Figure 28). PAA-stabilized small silver nanoparticles were thoroughly characterized in a previous study (see chapter 5.1.1).[32] The PAA ligand was exchanged for tyrosine or fluorescent-marked albumin (BSA-FITC). The adsorption of the ligands was monitored by DLS. The fluorescent particles were characterized by SAXS, UV/Vis, and fluorescence spectroscopy. Afterwards, desorption of the ligands tyrosine and BSA-FITC was monitored by fluorescence spectroscopy, showing that the BSA-FITC/particle complex exhibits sufficient stability for laboratory applications. Based on these results, the BSA-FITC-labeled nanoparticles were first used in biological applications, namely cell viability tests, cellular uptake analyses, and *in vitro* imaging.

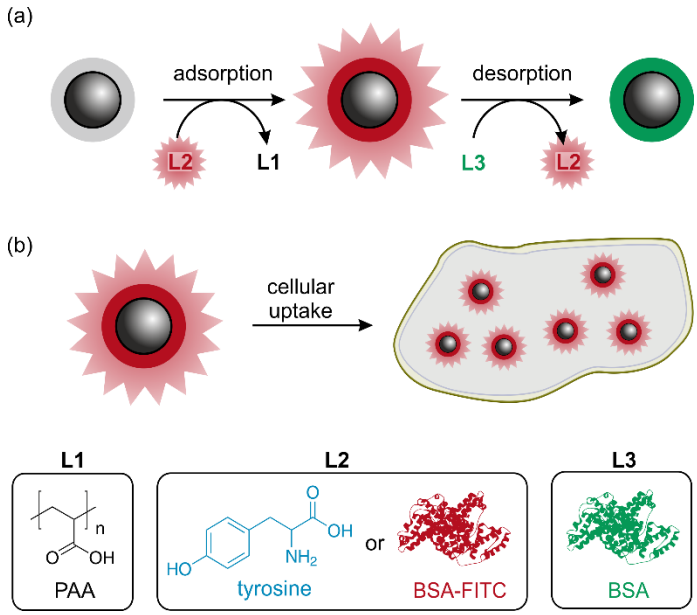

Figure 28. Scheme of adsorption and desorption experiments with the fluorescent labels tyrosine and BSA-FITC to silver nanoparticles.

Adsorption Process

For the production of fluorescent-labeled particles, we have chosen two different molecules for ligand exchange: i) tyrosine and ii) BSA-FITC. Tyrosine is a non-essential amino acid and has a high biocompatibility. Due to the conjugation with the aromatic ring, the side chain is optically active. Typically, tyrosine is excited at wavelengths around 276 nm and emits at 310 nm. BSA-FITC is composed of the protein albumin and the fluorescent marker fluorescein isothiocyanate (FITC). BSA-FITC is excited between 480 and 500 nm and emits at 519 nm. As depicted in Figure 29, the two fluorescent labels were chosen because they show only a small overlap of their emission spectra with the absorbance band of the silver nanoparticles. Therefore, potential quenching effects caused by the spatial proximity to the silver nanoparticles are reduced. Nevertheless, a variety of conditions and molecular interactions, for example molecular rearrangements, ground state complex formation and collisional quenching can result in fluorescence-quenching effects.[127]

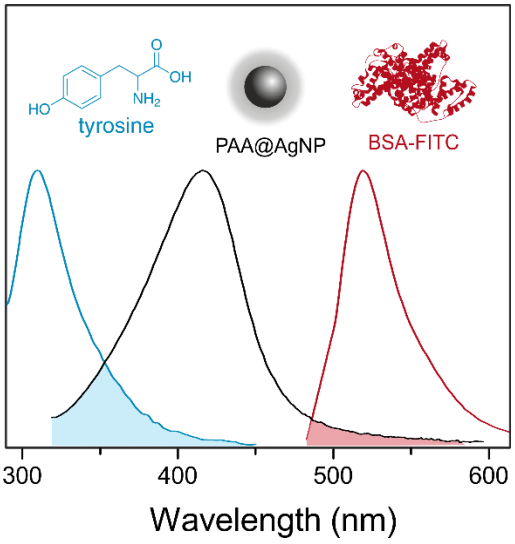

Figure 29. Normalized absorbance spectrum of PAA-stabilized silver nanoparticles (black line) and emission spectra of tyrosine (blue line) and BSA-FITC (red line) in water at 298 K. The areas where absorbance and emission spectra overlapped are marked by brighter colors.

The ligand exchange process was monitored by DLS. After addition of the new ligand, the hydrodynamic radius was changing with desorption of PAA and concurrent adsorption of tyrosine or BSA-FITC (Figure 30). The initial particles showed a hydrodynamic radius of R_h = 7.1 ± 0.4 nm (Figure 30b). We observed that for tyrosine the R_h decreased to 5.5 ± 0.3 nm immediately after addition of tyrosine. This radius did not change significantly over the time range of 196 h. In contrast, for the ligand exchange with BSA-FITC, the hydrodynamic radius increased slowly over time. Since BSA-FITC was added in excess, the reaction can be treated as a pseudo-first order reaction. Therefore, we used the following equation for data evaluation:

$$R_h(t) = R_h(0) + \Delta R_h(1 - e^{-kt}) \quad (25)$$

In this equation $R_h(0)$ is the initial hydrodynamic radius before ligand exchange, ΔR_h is the extrapolated increase of the hydrodynamic radius for infinite times, k is a formal rate constant and t is the experimental time in hours. The curve fit with its 95 % confidence interval is shown in Figure 30a. With the best fit value for ΔR_h of 3.6 ± 0.2 nm, we determined the value for the final hydrodynamic radius R_h = 10.7 ± 0.4 nm. This value is close to the experimental finding after three days and later. With equation (26) we calculated the time when half of the ligand on the surface of the particles is exchanged:

$$t_{1/2} = \ln(2) \cdot k^{-1} \quad (26)$$

The value for $t_{1/2}$ amounts to 26 ± 3 h for BSA-FITC. Therefore, the reaction time for a full conversion to can be expected to be around 3 days. These findings show that the rate-determining step of the ligand exchange is the adsorption of the new ligand, and that the reaction is mainly independent on desorption of PAA.

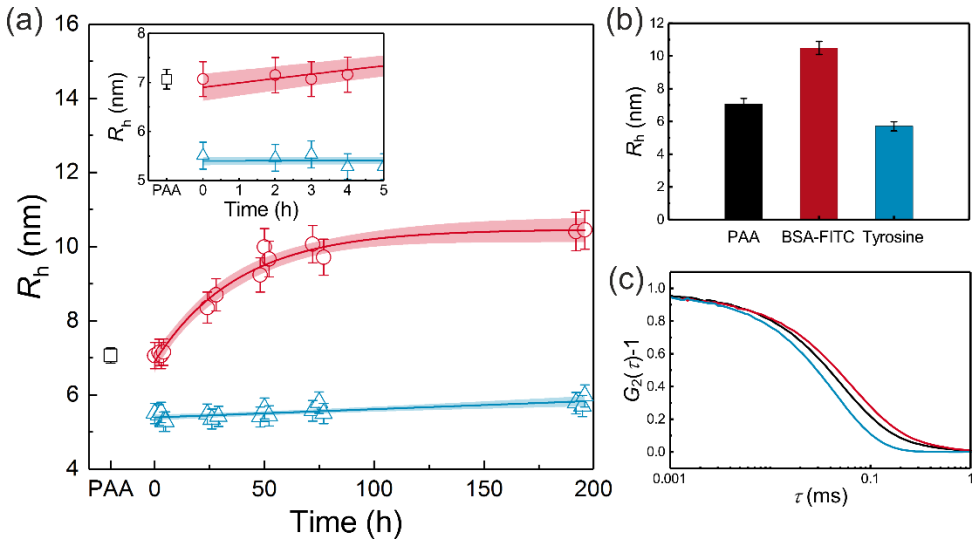

Figure 30. (a) DLS results for monitoring of the ligand exchange with BSA-FITC (red), and tyrosine (blue). Time-dependent hydrodynamic radius after addition of the new ligand is marked by symbols (red circles for BSA-FITC and blue triangles for tyrosine). The resulting fit for a first order reaction is given for BSA-FITC (solid red line), whereas for tyrosine a linear fit is displayed (solid blue line). Confidence bands at a 95 % level are included (brighter areas). Inset: detailed view of the initial hydrodynamic radius and the first 5 h. (b) Final hydrodynamic radii before and after respective ligand exchange. (c) Correlation functions of the initial particles and the particles after ligand exchange.

We used SAXS to verify that the observed effects on the hydrodynamic radius originate from the successful ligand exchange and not from agglomeration or aggregation (Figure 31a). The volume-weighted size distribution of the particles was calculated from the SAXS curves with the help of a Monte Carlo-based evaluation method, which was proven suitable for precise size distribution quantification.[73, 128] In order to determine the mean volume-weighted radius and the distribution width, the size distributions were approximated by a Gaussian function (Figure 31b). The mean volume-weighted radius of the initial particles was $R_{v,PAA}$=3.1 ± 0.1 nm, whereas the radii after ligand exchange with tyrosine, and BSA-FITC amounted to $R_{v,tyrosine}$ = $R_{v,BSA\text{-}FITC}$ = 3.3 ±0.1 nm. Thus, the size distribution of the particle cores did not change substantially upon ligand exchange.

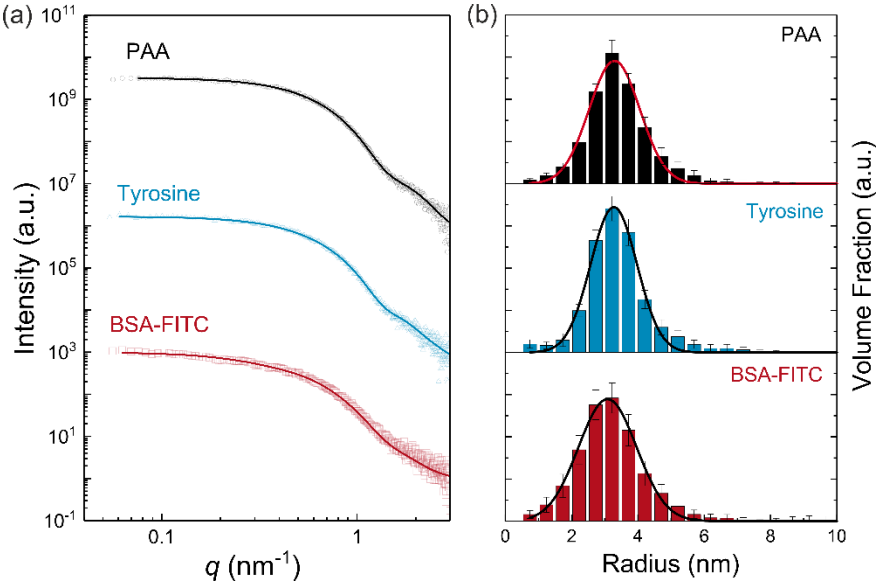

Figure 31. (a) SAXS data and corresponding curve fits (symbols and solid lines, respectively) of silver nanoparticles stabilized by PAA (black), tyrosine (blue), and BSA-FITC (red). The curves are shifted vertically for better visibility. (b) Volume-weighted size distributions (bars) derived from curve fits in (a). Gaussian fits of the size distributions are marked by solid lines (red for PAA, black for tyrosine and BSA-FITC).

The results of the SAXS evaluations agree with the imaging data obtained via scanning transmission electron microscopy (STEM), as depicted in Figure 32. The particles were spherical and showed no sign of aggregation after successful ligand exchange.

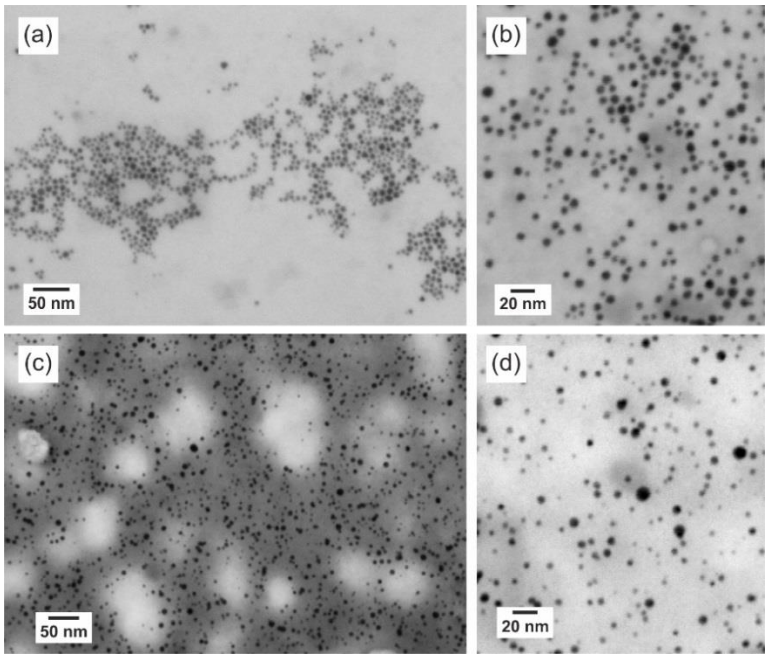

Figure 32. STEM images of the transfunctionalized silver nanoparticles at different magnifications: (a) and (b) show tyrosine-stabilized nanoparticles (scale bars are 50 nm and 20 nm); (c) and (d) show BSA-FITC-stabilized nanoparticles (scale bars are 50 nm and 20 nm) after successful ligand exchange.

The fluorescent properties of the transfunctionalized particles were characterized by fluorescence spectroscopy (Figure 33). From the comparison of the fluorescence emission spectra of the particles coated with tyrosine or BSA-FITC with their corresponding free analogs (without particles, same concentration), we assume that the silver nanoparticles induce fluorescence quenching. This is in accordance with the literature, in which silver nanoparticles are described as highly efficient quencher for fluorescence.[129] We found that the fluorescence intensity of the BSA-FITC-stabilized particles was 70 % of the intensity of pure BSA-FITC, at the fluorescence maximum of 520 nm. A stronger fluorescence quenching of 54 % at the emission maximum of 310 nm was observed for the tyrosine-stabilized particles. However, the remaining fluorescence intensity was intensive enough for the intended application of these particles in biological investigations.

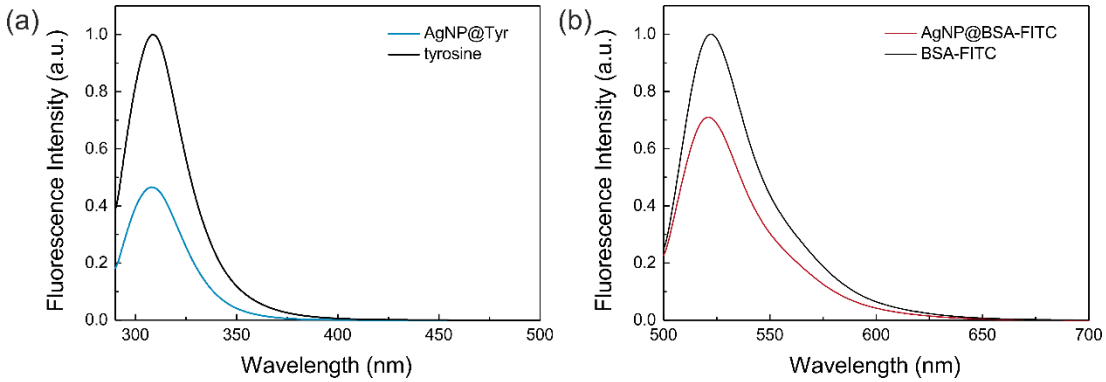

Figure 33. Fluorescence emission spectra of (a) tyrosine and (b) BSA-FITC (black curves) in comparison with the corresponding stabilized silver nanoparticles (blue and red curve, respectively). Excitation wavelengths were 276 nm for tyrosine and 487 nm for BSA-FITC.

A parameter of high interest is the amount of surface-bound ligand.[130-132] Its quantitative determination *in situ* remains particularly challenging. We used a fluorescence titration method to elucidate this issue. With this technique, the fluorescent ligand is titrated against the nanoparticles. The increase in the fluorescent signal allows the calculation of the amount of surface-bound ligand. For the adsorption of BSA-FITC, the changes in fluorescence quenching in comparison with the system without nanoparticles are displayed in Figure 34a. The fluorescence intensity reaches a limit where the fluorescence of further added ligand is not quenched (Figure 34b). Thus, the particle surface coverage by the fluorescent BSA-FITC ligand has reached saturation, and additional ligands diffuse "freely" in solution. The point where the curve of Figure 34b reaches the saturation region corresponds to the intersection of

two tangents, which approximate the linear curve progression in the beginning and at the end. We calculated that the silver nanoparticle surface is covered by 20 ± 9 BSA-FITC molecules.[133] This corresponds in approximation to a monolayer of the ligand.

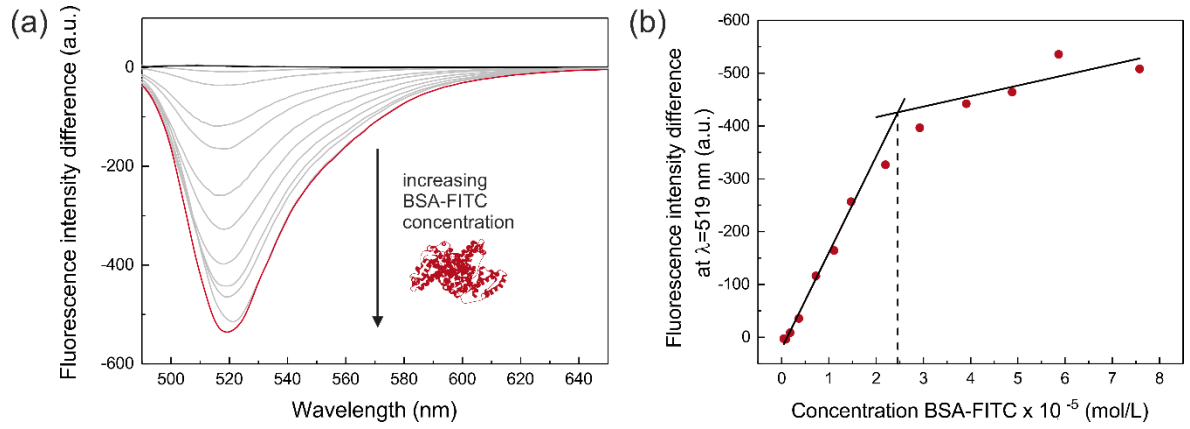

Figure 34. (a) Difference of fluorescence spectra of silver nanoparticles stabilized by BSA-FITC ($I_{BSA\text{-}FITC}$) and of the system without nanoparticles (I_{ref}): $I_{BSA\text{-}FITC}$ - I_{ref}. Different BSA-FITC concentrations were used, ranging from 0.5 µM (black curve) to 75.8 µM (red curve). (b) Displayed are the intensities at 519 nm of (a) in dependence of the BSA-FITC concentration (red circles). Crossing of the two tangents (black lines) represents the equivalence point which gives the ratio of BSA-FITC molecules per silver nanoparticle of 20 ± 9.

For the tyrosine-stabilized particles, the silver nanoparticles were titrated against a known amount of tyrosine. The amount of surface-bound ligand was determined by a data evaluation similar to the one previously described (Figure 35). For tyrosine, this corresponds to a number of 15900 ± 200 molecules per nanoparticle, which would imply a multi-layered structure on the particle surface. At a first glance, the high number of tyrosine molecules contrasts the results of the DLS, as the ligand shell should be larger than 2.2 nm (~0.6 nm would correspond to a tyrosine monolayer). A possible explanation for this discrepancy is the formation of a hard and soft corona of tyrosine, similar to that reported for many proteins.[134-136] Since the nanoparticles were filtered before DLS measurements, the soft corona can be potentially sheared off during sample preparation. To verify this hypothesis, we again measured the DLS of the tyrosine-stabilized nanoparticles without previous filtration. The measured hydrodynamic radius was substantially higher (R_h = 7.8 ± 0.5 nm, 4.5 nm shell thickness), and thus affirmed the assumption of a hard and a soft corona.

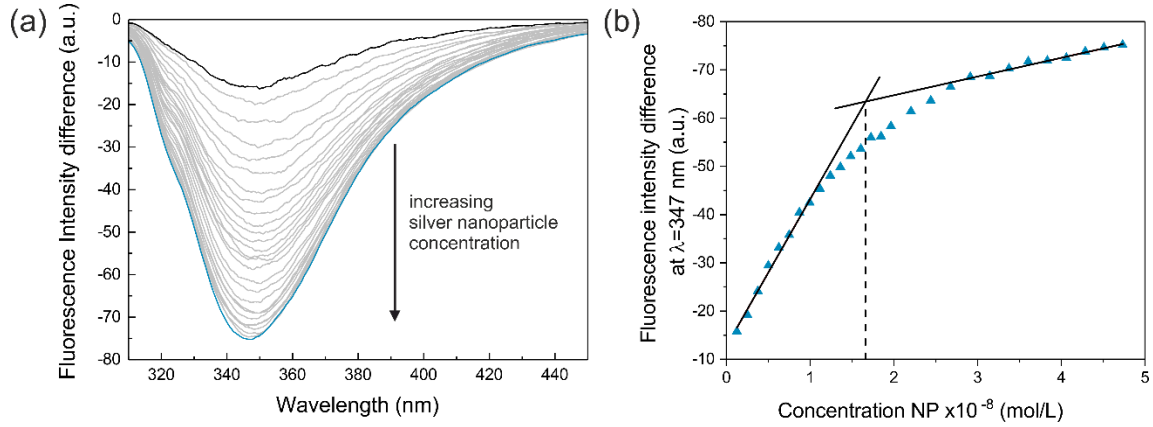

Figure 35. (a) Difference of fluorescence spectra of silver nanoparticles stabilized by tyrosine (I_{tyr}) and of the system without nanoparticles (I_{ref}): I_{tyr}- I_{ref}. Silver nanoparticles were titrated against a constant tyrosine solution (silver nanoparticle concentrations ranging from 1.3 nM (black curve) to 47.3 nM (blue curve). (b) Displayed are the intensities at 347 nm of (a) in dependence of the silver nanoparticle concentration (blue triangles). Crossing of the two tangents (black lines) represents the equivalence point which gives the ratio of tyrosine molecules per silver nanoparticle of 15900 ± 200.

Desorption Process

Toxicological studies of nanoparticles often comprise *in vitro* and *in vivo* studies, in which the transport, uptake and a possible accumulation of the particles can be observed. The use of a fluorescent marker is, therefore, a common concept to provide traceability. An important question, which is often not considered, is: How long does the fluorescent marker remain on the particle surface in physiological environment? We designed an experiment to give an approximation for this time span: the BSA-FITC-stabilized particles were diluted by a concentrated (20 g L^{-1}) solution of BSA which was not fluorescent-labeled. Fluorescence intensity was expected to increase when BSA-FITC of a population, which is attached to the silver surface or also in the vicinity of the silver surface, is exchanged with non-fluorescent BSA and released into the bulk solvent. Due to the exchange, fluorescence is not quenched anymore and increases as long as BSA-FITC is released. For our experiment, we have chosen two different dilutions (1:300 and 1:3000) of the silver nanoparticles to give an insight into desorption time spans (Figure 36). As a control experiment, the particles were diluted in phosphate-buffered saline (PBS), which is the matrix for BSA in the exchange experiment. Therein, the fluorescence intensity of the BSA-FITC-stabilized nanoparticles was normalized to 1 after a 1:300 dilution in PBS. The intensity of this mixture was in equilibrium instantaneously and remained constant for 12 days. In contrast, in the same time interval, the

fluorescence intensity of the mixture of BSA-FITC-stabilized particles with BSA increased from 0.45 to approximately 0.6 for a dilution of 1:300 and from 0.45 to 1.0 for a dilution of 1:3000. Thus, it is obvious that a very high dilution and long incubation times are needed to remove BSA-FITC from the particles.

For the quantification of the release of BSA-FITC we applied a simple model. Corresponding to the adsorption process, we utilized a similarly modified first order reaction kinetic rate equation:

$$I_f(t) = I_f(0) + \Delta I_f\left(1 - e^{-k\,t}\right) \tag{27}$$

The I_f (t) is the fluorescence intensity at time t, I_f (0) is the fluorescence intensity at t = 0, and ΔI_f is the extrapolated value for the increase of the fluorescence intensity for infinite time, k is a formal rate constant, and t is the experimental time in hours. In order to avoid ambiguous results, we used constant values of I_f (0) = 0.45, and ΔI_f = 0.55 to fulfill the normalization condition $I_f(0) + \Delta I_f = 1$ at infinite time. Therefore, only k remained as a free fit parameter. The k-values can be utilized to calculate the time τ required to release 50 % of BSA-FITC contained in ΔI_f by

$$\tau = \ln(2) \times k^{-1} \tag{28}$$

The resultant τ-value is 21 ± 3 days for a dilution of 1:300 and 3.4 ± 0.4 days for the 1:3000 dilution. Therefore, we assume that the release of BSA-FITC from the vicinity of the silver cores is in the order of days for the high 1:3000 dilution and in the order of weeks for the lower 1:300 dilution. This shows that the binding of BSA-FITC to the particles is relatively strong. We conclude that there is no indication for a substantial risk that the BSA-FITC-stabilized particles lose their fluorescent corona due to dilution when used, for example, in cell experiments for toxicological studies.

The same experiment was conducted with the tyrosine-stabilized nanoparticles, during which no slow increase in the fluorescence intensity was observed after addition of BSA. We conclude that similar to the fast adsorption of tyrosine, the desorption of tyrosine also occurs quickly, which results in a constant fluorescence signal after addition of BSA. Therefore, we assume that it was not possible to monitor the exchange process because it was too fast, and with the first UV/Vis measurement directly after addition (t=0), the desorption process was already completed. Furthermore, the stronger binding of the BSA by thiol groups has a greater range than the adsorption of tyrosine via carbonyl groups, and therefore supports the fast

desorption. We conclude that the exchange of tyrosine is fully completed in the time range of seconds.

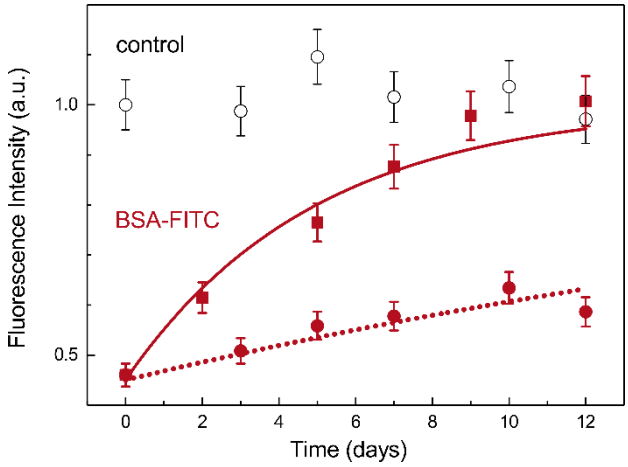

Figure 36. Fluorescence intensity at 519 nm as a function of time after the mixing of BSA-FITC-stabilized silver nanoparticles with a solution of native BSA (not fluorescence-labeled) with a dilution of 1:300 (red circles) and 1:3000 (red squares), with respect to the ratio of nanoparticles to water. Curve fits of a pseudo first-order reaction reveal τ-values of 21 ± 3 days (1:300 dilution, dotted red line) and 3.4 ± 0.4 days (1:3000 dilution, solid red line), respectively. The results of the control experiment (mixing of BSA-FITC-stabilized silver nanoparticles with PBS) is marked by black circles.

Biological Application

Based on the adsorption and desorption experiments, the BSA-FITC-stabilized silver nanoparticles were proven to be suitable for the investigation of their uptake and cellular localization in *in vitro* experiments. Therefore, we selected two cell models: (1) the liver cell model HepG2, which is a very commonly used hepatocyte *in vitro* model and (2) the most common cell model for the intestinal enterocytes, differentiated Caco-2 cells. Both cell types were incubated with non-cytotoxic concentrations of BSA-FITC marked silver nanoparticles for up to 24 h. Representative confocal images are given in Figure 37. They show a time-dependent uptake of silver nanoparticles in HepG2 cells with some nanoparticles having cell contact after 2 h, and numerous particles deep inside the cells after 24 h. In contrast to this, the differentiated Caco-2 monolayer showed just a few particles in contact with the microvilli brush border on the apical side of the monolayer for all time points, and almost no particles inside the cells. Therefore, the fluorescence labeling-enabled time-dependent uptake studies showed clear differences in particle uptake for cells from different tissues.

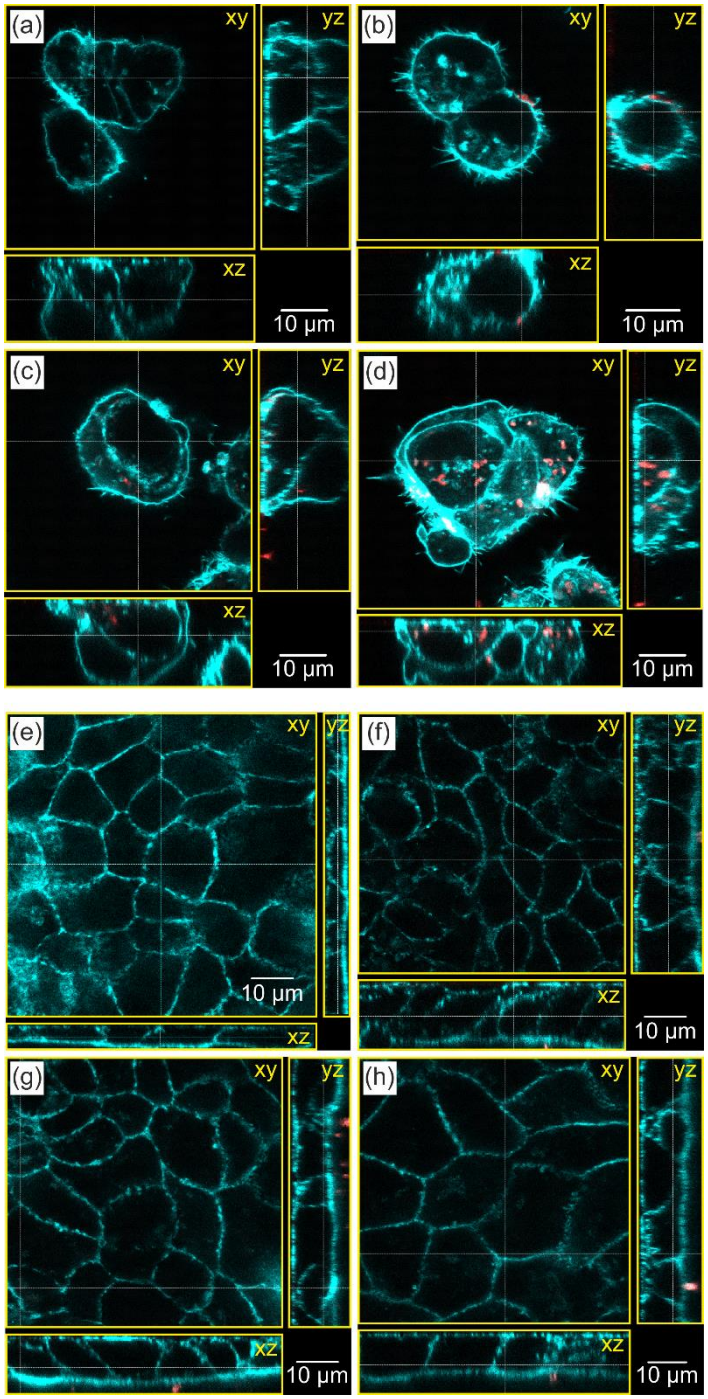

Figure 37. Confocal fluorescence microscopy images of HepG2 (a-d) and differentiated Caco-2 cells (e-h). The cell lines were incubated with BSA-FITC-stabilized particles for 2, 6, and 24 h (b-d for HepG2, and f-h for Caco-2 cells). A control sample for each cell line shows the status without silver nanoparticles (a and e). From preliminary cytotoxicity tests, non-cytotoxic silver concentrations of 10 and 25 µg/ml were chosen for HepG2 and Caco-2 cells, respectively. The images show the view in xy, xz and yz direction (yellow boxes), whereas the dotted white lines mark the plane from which the other cutting planes are derived. The cytoskeleton is stained by ActinRed 555 marked with blue color, whereas the BSA-FITC-stabilized particles are marked by red color.

Author contributions: Syntheses and characterization of nanoparticles were done by me. Furthermore, I performed the fluorescence experiments together with Maximilian Ebisch, with main contribution from my side. Data evaluation of SAXS, DLS and fluorescence spectroscopy was done by me. Linda Böhmert obtained the confocal fluorescence microscopy images. Linda Böhmert and I discussed the results, and I wrote the manuscript. All authors contributed to the final version of the manuscript.

5.2.3 Artificial Digestion of Silver Nanoparticles

This chapter is based on the paper "Monitoring the fate of small silver nanoparticles during artificial digestion", which has been partially modified and is reprinted in its original form in Appendix A.5.

Today, silver nanoparticles can be found in toothpastes and many other cosmetic products, as well as textiles, children's toys and dietary supplements.[6] The estimated human dietary intake of silver is 70–90 μg per day, which can be substantially higher in individual cases due to a widespread application of silver nanoparticles.[10] The unique properties of the nanoparticles are strongly dependent on the conditions of their surroundings. The examination of orally ingested particles is particularly interesting due to the dramatically changing surrounding conditions during digestion, such as changes in pH and salt concentrations. There, the particles pass through different digestion steps, during which physicochemical parameters like the pH are shifted over a wide range. The steps of an *in vivo* digestion include the introduction of the nanoparticles in saliva, which is followed by exposure to gastric and intestinal juices. Hence, different mechanisms are possible, which include aggregation, enhanced ion release or *de novo* particle formation.[137-138]

Most studies regarding the toxicological potential of silver nanoparticles are focused on their intestinal uptake and interaction with different cell types, such as M-cells or Caco-2-cells.[51] However, when considering different altering mechanisms during the digestion process, the question arises whether the silver particles can pass through the different digestion steps in a nanoscale form. These complex interactions between particles and the conditions of their surroundings can only be investigated in an *in vitro* model. Therefore, as previously described,[79] we used an artificial digestion procedure, which is based on the German standard DIN 19378.[80] We adjusted this procedure for digestion of silver nanoparticles (Figure 38). It simulates the three steps of the gastro-intestinal passage by replicating oral, gastric, and small intestinal conditions. These contain all relevant factors for a realistic environment, such as pH changes, transit times between different digestion steps, and also enzymes and digestive juices. Furthermore, the addition of food components completes the simulation of a realistic digestion process in a human body. Previous studies only considered the digestion without food components.[138] However, there is a lack of detailed investigations

regarding the influence of food components on changes of the size distribution of silver nanoparticles.[139]

We used the PAA-stabilized silver nanoparticles in the artificial digestion process. To evaluate possible changes in their characteristics, including core sizes, shapes and size distributions, we utilized SAXS. The silver particles can be measured directly in saliva, gastric and intestinal juice without purification or separation from the juices.[138] The aim of this study is to reveal the impact of digestion on the colloidal stability of very small silver nanoparticles for two different scenarios: digestion with and without food additives. As representative food components, we have chosen oil, starch, skimmed milk powder and a mixture of these three components to mimic realistic food surroundings.

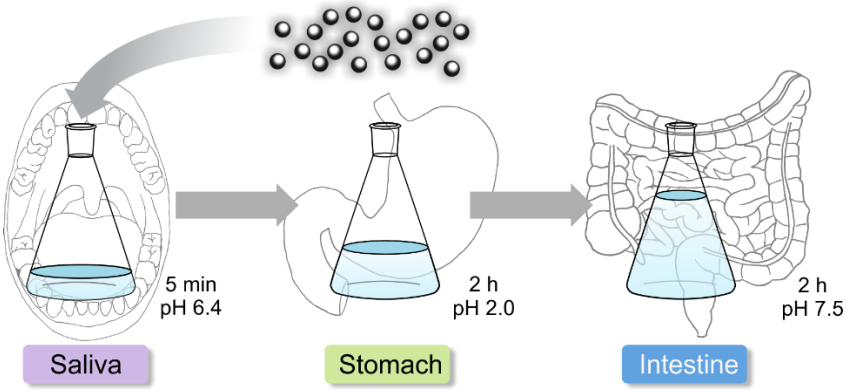

Figure 38. Scheme of the artificial digestion of silver nanoparticles following three stages: saliva, gastric, and intestinal tract. The path taken by the particles is indicated by arrows. Residence times and pH values are denoted.

For the digestion of NP_{PAA} in absence of food components, radii distributions which can be interpreted as result of mixtures of primary particles and aggregates were present. We found that the following sum of two cumulative lognormal distribution functions suitably quantifies the distributions for all stages of digestion:

$$F(R) = \frac{a_1}{2}\, erfc\left(\frac{log\left(\frac{R_{0,1}}{R}\right)}{\sqrt{2}w_1}\right) + \frac{a_2}{2}\, erfc\left(\frac{\left(log\left(\frac{R_{0,2}}{R}\right)\right)}{\sqrt{2}w_2}\right) \tag{29}$$

Therein a_i are scaling factors, which are a measure for the volume fraction of primary particles and aggregates, respectively. The w_i are width parameters and the $R_{0,i}$ correspond to the median radii. Using these parameters, the mean radii R_i and the relative standard deviations of the width of the size distributions σ_i were calculated according to equations (30) and (31).

$$R_i = R_{0,i}\, e^{\frac{w_i^2}{2}} \tag{30}$$

$$\sigma_i = R_i \sqrt{e^{2w_i^2} - e^{w_i^2}} \tag{31}$$

The radii distribution of the pristine particles displays a mean radius of R_1= 3.1 ± 0.1 nm and a relative distribution width of σ_1 = 0.2. The second term in equation (29) was zero, which means that no indication for the presence of aggregates was found. An amount of 100% of particles is smaller than 6 nm (Figure 39). With SAXS, only the silver core of the particles can be characterized, while the stabilizing shell of PAA is practically invisible due to the large X-ray scattering contrast of silver. The particles are stable at a basic pH, but aggregate at acidic pH. Therefore, as expected, aggregation took place when the primary particles were incubated in the saliva at pH 6.4 for 5 min (Figure 39). Only 48 % of the primary particles are present. The rest of them form aggregates with a mean radius of R_2= 8 ± 2 nm and a relative width of σ_2 = 0.31.

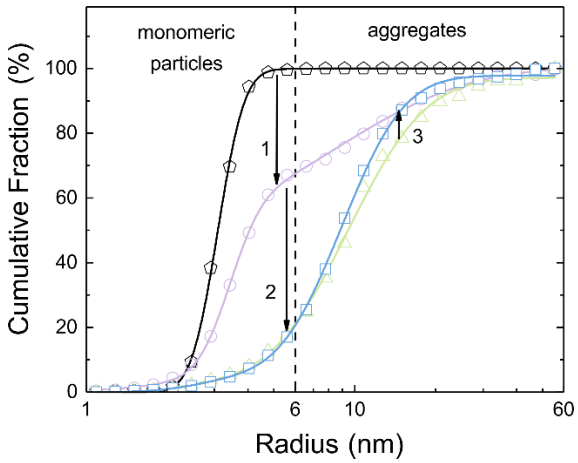

Figure 39. Volume-weighted radii distributions of silver nanoparticles derived by SAXS measurements. Shown are pristine particles and particles after the three stages of artificial digestion: saliva, stomach, and intestine (black pentagons, purple spheres, green triangles and blue squares, respectively) in cumulative fraction presentation. Particles were digested without food components. The solid lines are best fit curves according to equation (29). The path of digestion is indicated by numbered arrows.

We estimated the aggregation number from the ratio of the volume of an aggregate to the volume of a primary particle according to equation (32).

$$N_{agg} = \frac{R_2^3}{R_1^3} \tag{32}$$

From this follows that the aggregates consist of 21 ± 13 primary particles. The second step of digestion includes the incubation at pH 2 in the stomach for 2 h. After this stage, the size of primary particles decreased to R_1 = 2.2 ± 0.7 nm, and their relative fraction decreased to 3 ± 2 %. The remaining particles form aggregates with a mean radius of R_2 = 9 ± 1 nm and a relative width of σ_2 = 0.23. Due to the small fraction of primary particles, a reliable determination of the aggregation number is not possible. The final step is the incubation in the intestinal juice at pH 7.5 for 2 h. At this stage, the radius of the primary particles amounts to R_1 = 2.6 ± 0.7 nm and the volume fraction of primary particles stays constant. The aggregates display a mean radius of R_2 = 9 ± 1 nm with a relative width of σ_2 = 0.18.

As an initial summary, we conclude that the radii of the primary particles decrease in the stomach in the course of digestion (Figure 41a). Most of the particles immediately form aggregates in saliva. Only a few primary particles are present in the stomach and the intestine (Figure 41b). All size distribution parameters are summarized in Table 6.

To obtain information about the whole particle complex, including core and ligand shell, DLS is typically applied. A combination of SAXS and DLS data allows an estimation of the thickness of the particles' shells.[140] DLS cannot be used for the present system due to the complex media of the turbid digestion fluids, wherein the particles are dispersed. DLS provides no meaningful results for particles in such turbid media.

The digestion of the particles was repeated in the presence of oil, starch, milk and a mixture of the three. The resulting distributions of the radii and curve fits utilizing equation (29) are shown in Figure 40. Distribution parameters are summarized in Table 6. From the inspection of the figures and the fit parameters, it is clear that the presence of food strongly influences the aggregation behavior in comparison to the situation without food. Furthermore, the curves and parameters in the presence of oil and starch are similar, as well as the curves and parameters for the presence of milk and the food mixture.

The primary particle radii are constant in saliva in all cases, like they were in the absence of food. The radii decrease in the stomach from R_1 = 3.1 nm to R_1 = 2.5 nm and R_1 = 2.2 nm in the presence of oil and starch, whereas no reduction was observed for milk and food mixture.

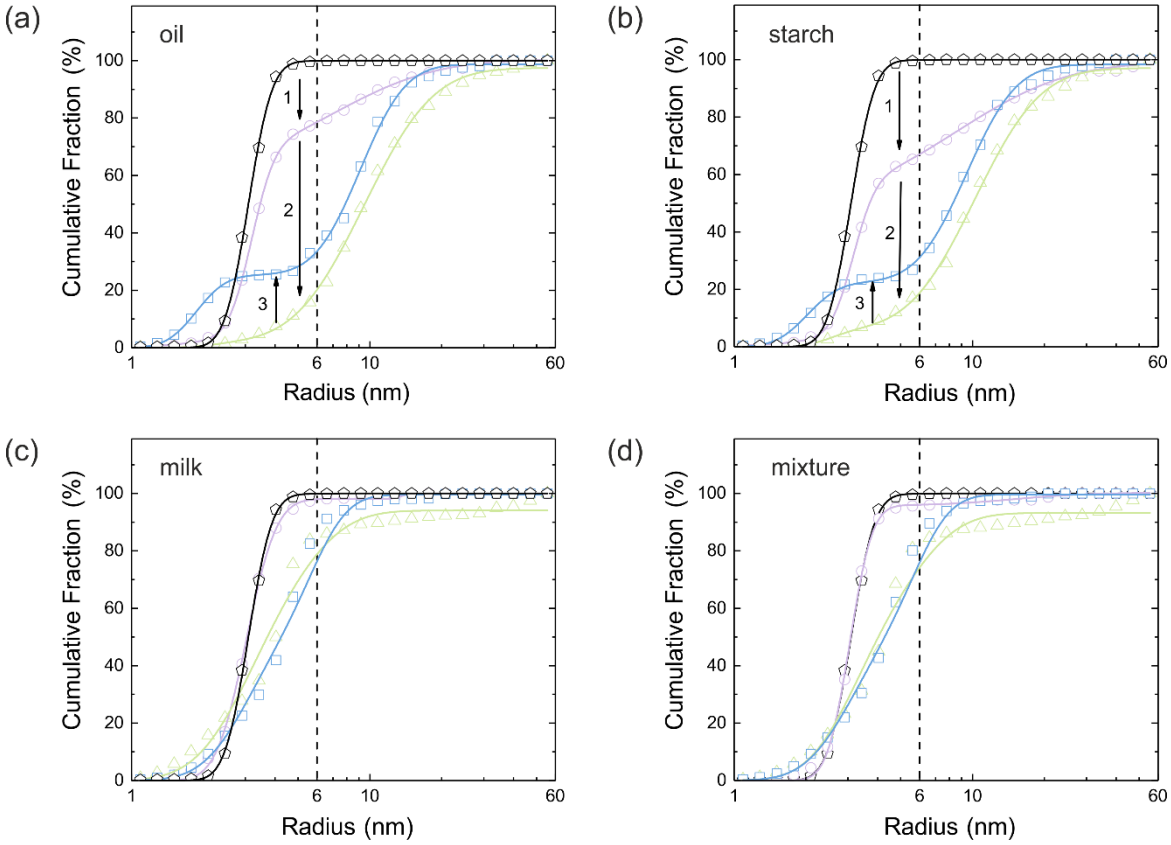

Figure 40. Volume-weighted radii distributions of pristine particles (black pentagons) and at the three stages of artificial digestion: saliva, stomach, and intestine (purple circles, green triangles and blue squares, respectively) in cumulative fraction presentation. Particles were digested with oil (a), starch (b), skimmed milk powder (c), and a mixture of all components (d). The solid lines are best fit curves utilizing equation (29). The dashed vertical line at a radius of 6 nm indicates the upper limit of the radius of primary particles.

Additionally, the size of the aggregates is almost the same, both, in the presence of food and without. In saliva, the aggregates' radius is $R_2 = 7 \pm 1$ nm for oil and $R_2 = 9 \pm 1$ nm for starch, while no aggregates were found for milk and the food mixture. The aggregates' radii in the stomach and the intestine are very similar for oil $R_2 = 9 \pm 1$ nm and starch $R_2 = 10 \pm 1$ nm. Only very small aggregates of 6 nm radius were detectable for milk and the food mixture (Figure 41a). Interestingly, the volume fraction of primary particles displays a low minimum of approximately 2 % and 6 % in the stomach followed by an increase to 25 % and 22 % in the intestine for oil and starch, respectively. In contrast, a fraction of 100 % primary particles was found in saliva for milk and the food mixture. This is followed by a continuous decrease to 72 % for milk and 60 % for the mixture in the stomach. Final values were 57 % for milk and 56 % for the food mixture in the intestine. The aggregation numbers in the presence of oil increase successively: $N_{agg} = 13 \pm 3$, 86 ± 2, and 117 ± 4. Similarly, in the presence of starch,

aggregation numbers of N_{agg} = 25 ± 4, 66 ± 2, and 103 ± 5 are determined. In contrast, small aggregation numbers of approximately 7 were found for milk and the food mixture in the stomach and the intestine (Figure 41c).

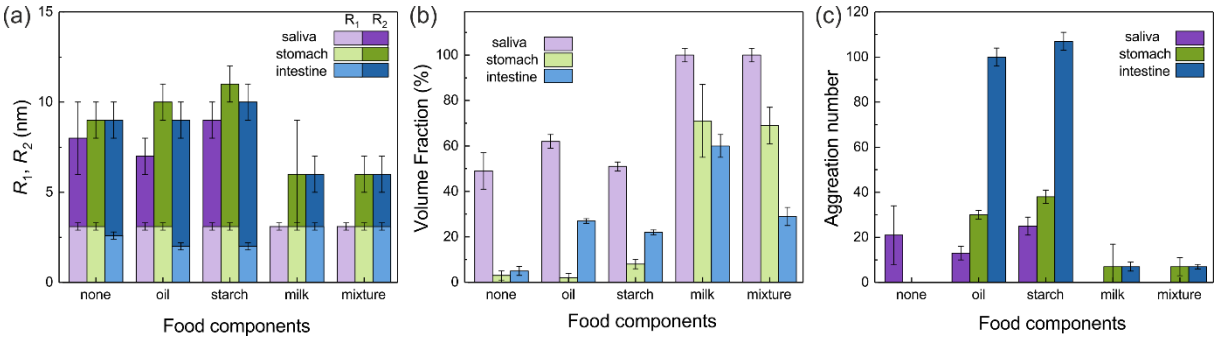

Figure 41. (a) Mean radii of primary silver nanoparticles, R_1, and radii of their aggregates, R_2, (b) volume fractions of primary silver nanoparticles, and (c) aggregation numbers as a function of different food components. The parameters are presented according to the three stages of the digestion process: saliva, stomach and intestine (purple, green, and blue bars, respectively).

Our findings show that all food components have a strong colloidal stabilizing effect in comparison to the situation without additives. Oil and starch are similar in their stabilization properties, and the size of aggregates is limited to a radius of approximately 10 nm and maximum aggregation numbers of approximately 100. Milk and the food mixture are the strongest in preventing particle's aggregation. Here, the size of aggregates is limited to a radius of approximately 6 nm, with aggregation numbers of approximately 7. Moreover, only in the presence of milk proteins was no radius reduction of the primary particles observed after intestinal incubation. We attribute these findings to the strong colloidal stabilizing properties of milk proteins. The surprising increase of the fraction of primary particles from the stomach to the intestine in the presence of oil may be explained by the presence of lipase in the latter. The artificial intestinal juice is composed of pancreatin which mainly contains lipase. This enzyme catalyzes the hydrolysis of fats, just like the used oil. Therefore, we assume that the oil is converted to fatty acids, which stabilize the primary particles and lead to their increase. Similarly, we assume that stabilizing oligosaccharides were formed by the hydrolysis of starch due to the enzyme amylase, which is also present in pancreatin. That could explain the increase of primary particles from the stomach to the intestine in the presence of starch.

Table 6. Characteristics of primary particles and aggregates in pristine state and after the digestion stages saliva, stomach and intestine, resultant from curve fits applying equation (29). Given are primary particle radii (R_1), their relative volume fraction (Fraction), radii of the aggregates (R_2), their relative distribution width (σ_2) and average aggregation numbers of primary particles per aggregate (N_{agg}). The relative width σ_1 is in the range of 0.1–0.2 and the uncertainty of R_1 is ± 0.1 nm.

Food	R_1 (nm)	Fraction (%)	R_2 (nm)	σ_2	N_{agg}
Pristine silver nanoparticles					
	3.1	100	-[a]	-[a]	-[a]
Nanoparticles in saliva					
None	3.1	48 ± 10	8 ± 2	0.31	21 ± 13
Oil	3.1	62 ± 3	7 ± 1	0.30	13 ± 3
Starch	3.1	51 ± 2	9 ± 1	0.35	25 ± 4
Milk	3.1	100	-[a]	-[a]	-[a]
Mixture	3.1	100	-[a]	-[a]	-[a]
Nanoparticles in the stomach					
None	2.2	3 ± 2	9 ± 1	0.23	80 ± 2
Oil	2.2	2 ± 2	9 ± 1	0.23	86 ± 2
Starch	2.5	6 ± 2	10 ± 1	0.22	66 ± 2
Milk	3.1	72 ± 14	6 ± 2	0.16	7 ± 9
Mixture	3.1	60 ± 15	6 ± 2	0.16	7 ± 6
Nanoparticles in the intestine					
None	2.6	5 ± 2	9 ± 1	0.18	42 ± 2
Oil	1.9	25 ± 1	9 ± 1	0.15	117 ± 4
Starch	2.0	22 ± 1	9 ± 1	0.16	103 ± 5
Milk	3.1	57 ± 6	9 ± 1	0.16	7 ± 2
Mixture	3.1	56 ± 5	9 ± 1	0.11	7 ± 1

[a] No aggregates were detected.

Author contributions: Syntheses of nanoparticles were done by me. Furthermore, I performed the artificial digestion together with Dajana Lichtenstein, Maximilian Ebisch and Petra Fengler. SAXS measurements and data evaluation were done by me. I wrote the manuscript. All authors contributed to the final version of the manuscript.

5.2.4 Artificial Digestion of Silver Nitrate

This chapter is based on the paper "What happens to the silver ions? – Silver thiocyanate nanoparticle formation in an artificial digestion", which has been partially modified and is reprinted in its original form in Appendix A.6.

In contrast to gold, silver nanoparticles can continuously release ions through slow corrosion. For example, it was demonstrated by Sotiriou et al.[141] that small-sized silver nanoparticles (radius < 5 nm) release a significant concentration of silver ions from their surface. Therefore, biological impacts may emerge from formed silver ions and not from the nanoparticles itself. Considering Sotiriou's study, it is reasonable to assume a coexistence of particle degradation and formation. Therefore, nanoparticle formation from silver ions also has to be taken into account.[11] Whereas most investigations focus on the incorporation of silver nanoparticles during digestion, only a small number of studies are dealing with the possible impact of a nanoparticle formation from silver ions in a physiological environment.

The major uptake route of silver particles and ions is the oral ingestion.[10] A human digestion process includes different conditions which can strongly affect nanomaterials. Hence, for the evaluation of nanomaterials about digestion, changes of their physicochemical properties including aggregation, interaction with biomolecules, and dissolution must be investigated under these conditions. These changes can strongly influence later biological effects of the nanoparticles (so-called "nano-effects"). Interconversions of the particles additionally indicate that a transition between ions and nanoparticles may play an important role. The group of Walczak[142] took a closer look on the impact of the digestive procedure on silver nitrate and its formed particles. They detected nanoparticles with radii of about 10 – 20 nm in the intestinal tract but not at the earlier stages of digestion. They also suggested the presence of smaller particles. This assumption lacks experimental proof due to the detection limit of single particle-inductively coupled plasma mass spectrometry (SP-ICPMS) of approximately 10 nm,[101] used in their study. They were not able to determine the composition of the formed nanoparticles unambiguously.

The aim of our study is therefore to enhance the knowledge of nanoparticle formation from silver nitrate during artificial digestion. We used SAXS to monitor the emergence of particles and changes in their size distribution. We used the same standardized digestion

procedure as for silver nanoparticles (chapter 5.2.3) (Figure 42).[80, 143] Additionally, also the behavior of silver nitrate in presence of a mixture of relevant food components[143] (oil, starch and skimmed milk powder) was studied to simulate a realistic surrounding present at oral uptake. The samples were analyzed with SAXS after every step.

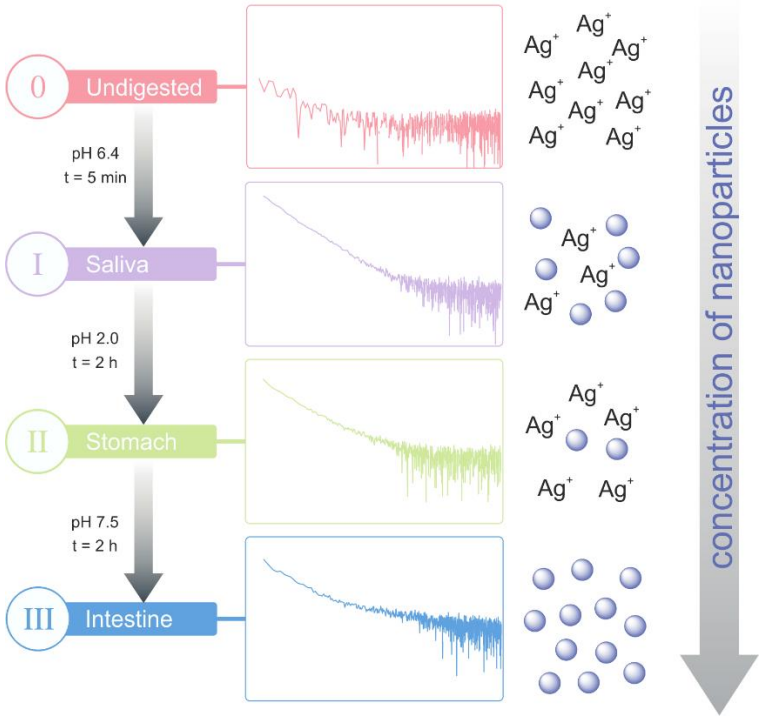

Figure 42. Scheme of the artificial digestion, the formation of nanoparticles, and monitoring by SAXS with the corresponding curves. Displayed are the 4 steps of the procedure (before digestion, saliva, stomach, and intestine).

The SAXS curves from saliva, stomach and intestine are typical for the presence of nanoparticles, which are not visible in the undigested silver nitrate solution (Figure 42). Volume-weighted radii distributions were evaluated with a Monte Carlo based data evaluation procedure[73] which was proved suitable for precise nanoparticles size distribution quantification.[128] The resulting size distributions are shown in Figure 43. Defined nanoparticle populations are present at all steps of digestion. The distributions are bimodal with particles with radii $R_1 < 5$ nm and particles with radii $R_2 > 5$ nm. Maxima for the small particles are clearly visible in the range of 2 - 4 nm, while no clear maxima are present for the larger particles. For quantification, data evaluation was conducted as for the digestion of silver nanoparticles (chapter 5.2.3): distributions were fitted by a sum of two cumulative lognormal functions which consist of two contributions according to equation (29). The mean radii R_i and the relative widths of the size distributions σ_i were calculated according to equation (30) and

(31), respectively. Since the SAXS measurements are defined on an absolute scale, the overall conversion of the silver ions into nanoparticles can be determined with the help of the resultant volume fraction and the density of the nanoparticles (ϱ = 3.828 g/cm^3, AgSCN).[144]

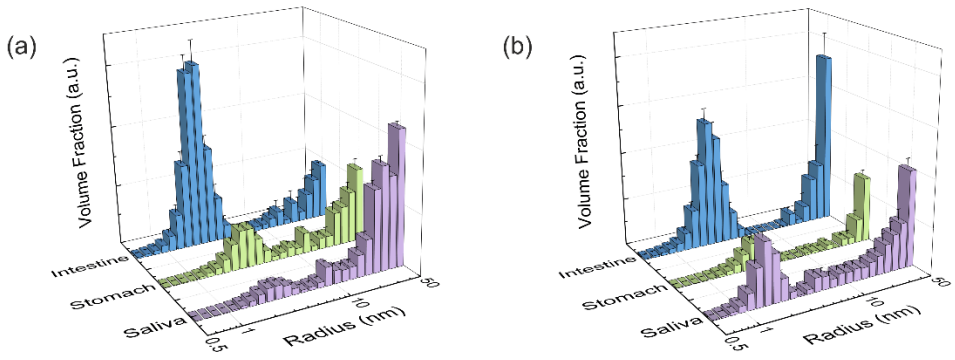

Figure 43. Volume-weighted size distributions derived by SAXS measurements of nanoparticles formed from (a) silver nitrate and (b) silver nitrate in the presence of food components at the three digestion steps: saliva, stomach and intestine (purple, green, and blue bars, respectively).

The experiments started with the digestion of silver nitrate in absence of food components. Already in saliva, nanoparticles are formed (Figure 43a). At this stage, the particles were incubated in saliva for 5 min at 37°C. The formed particle system consists of small particles with a narrow distribution width and larger particles which display a broader size distribution. A mean volume-weighted radius of R_1 = 4.0 ± 0.6 nm and a relative distribution width of σ_1 = 0.35 was determined for the small particles. All size distribution characteristics of the nanoparticles are summarized in Table 7. The small and large particles have relative volume fractions of 18 % and 82 %, respectively (Figure 44c), and the overall yield of the conversion of silver ions into particles amounts to 79 %. The following steps of digestion are the artificial gastric tract which includes a pH shift to a value of 2 and an incubation time of 2 h at 37 °C, as well as the intestine with a pH shift to 7.5 (incubation time and temperature are identical to stomach). During these digestion steps the fraction of small particles increases in stomach to 48 % and finally in the intestine to 78 %. The small particles' radius is decreasing at the same time from R_1 = 3.3 ± 0.2 nm to R_1 = 2.0 ± 0.1 nm in the intestinal tract. We also observed that the larger particles, which are present during every step, are also decreasing in size from R_2 = 45 ± 6 nm in saliva to R_2 = 30 ± 2 nm in intestine.

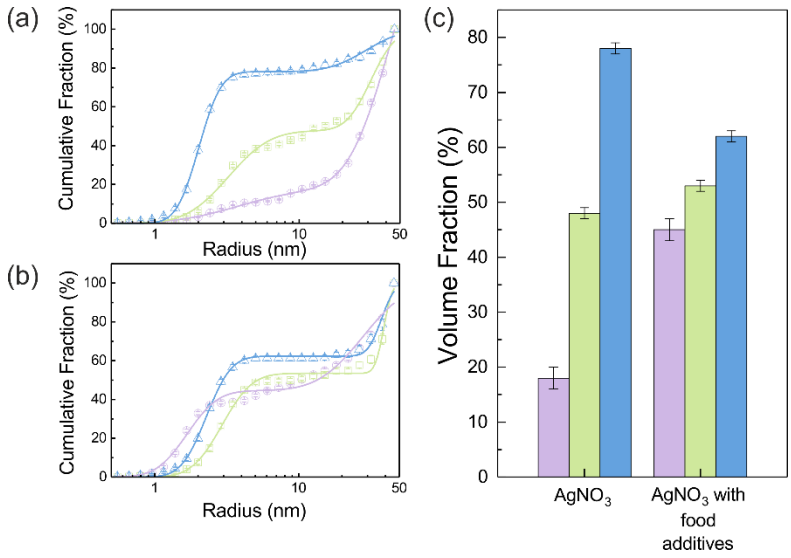

Figure 44. (a) and (b) Volume-weighted size distributions in cumulative fraction presentation at the three stages: saliva, stomach and intestine (purple, green, and blue symbols, respectively) with their corresponding fit curves (solid lines). Displayed are the resulting particles of the digestion of $AgNO_3$ (a) and $AgNO_3$ in the presence of food components (b). (c) Relative volume fractions of small particles at the three digestive steps.

The yield of the conversion decreases in stomach to 52 %, whereas in intestine a full conversion of 100 % was determined. We conclude that the digestive process promotes the formation of new particles. Especially the small particles show a narrowing size distribution with relative distribution widths of 0.35, 0.24, and 0.1, respectively (saliva, stomach and intestine). The radii of small and larger particles are decreasing in the course of digestion (Figure 45). A possible reason is the increasing amount of potentially stabilizing proteins in the digestive fluids, which enables a particle formation even in the first step of saliva.

As mentioned above, Walczak et al.[142] observed the formation of nanoparticles only in the intestinal tract, which is not in contrast to our results. The apparent differences between their and our results are due to the different lower detection limit of SP-ICPMS ($R_{limit} \geq 10$ nm) and SAXS ($R_{limit} \geq 0.5$ nm). We assume that the particles they found in the intestine are identical with the larger particles observed in our study. In addition to their findings we could prove that nanoparticles in the sub-10 nm range are present at each step of the digestive process.

The course of digestion of silver nitrate in the presence of a mixture of food components is depicted in Figure 43b and Figure 44b. Obviously, the formation of nanoparticles with radii lower than 5 nm starts also in saliva. Again, the size distribution is bimodal and contains small and larger particles. Here, the mean radius of the small particles is $R_1 = 1.7 \pm 0.1$ nm, whereas

the larger ones show a mean radius of R_2 = 29 ± 2 nm. The volume fraction of the small particles is 45 %.

The radii of small and large particles are reduced in comparison to the experiment without food components. The volume fraction of the small particles is twice as high as before. In a recent study about the digestion of silver nanoparticles we observed that food components improve colloidal stability of the particles during digestion.[143] Therefore, we assume that a stabilizing effect may also be present for nanoparticles produced from silver nitrate in saliva. The further steps of digestion show an increase in the volume fraction of small particles to 53 % and 62 % for the gastric and intestinal tract, respectively. The corresponding mean radii are R_1 = 3.0 ± 0.1 nm in stomach and R_1 = 2.3 ± 0.1 nm in intestine. Simultaneously, the radii of the larger particles increase in the gastric tract to R_2 = 39 ± 1 nm. This value stays constant until the end of digestion (R_2 = 38 ± 1 nm in intestine). The characteristics of the small particles in the stomach are not significantly different for the digestion with or without food components.

Table 7. Size distribution parameters of nanoparticles resulting from the digestion of $AgNO_3$ and $AgNO_3$ + food components (starch, oil and skimmed milk powder): small particle radii R_1, their relative distribution width σ_1, their relative volume fraction and radii of large particles R_2, their relative distribution width σ_2 and the overall yield of the conversion of silver ions into particles. Volume fractions of large particles can be calculated by: 100% – volume fraction of small particles.

Sample	R_1 (nm)	σ_1	Fraction (%)	R_2 (nm)	σ_2	Yield (%)
			Saliva			
$AgNO_3$	4.0 ± 0.6	0.35	18 ± 2	45 ± 6	0.24	79
$AgNO_3$ + food	1.7 ± 0.1	0.18	45 ± 2	29 ± 2	0.28	89
			Stomach			
$AgNO_3$	3.3 ± 0.2	0.24	48 ± 1	32 ± 1	0.13	52
$AgNO_3$ + food	3.0 ± 0.1	0.17	53 ± 1	39 ± 1	0.05	34
			Intestine			
$AgNO_3$	2.0 ± 0.1	0.10	78 ± 1	30 ± 2	0.20	100
$AgNO_3$ + food	2.3 ± 0.1	0.13	62 ± 1	38 ± 1	0.08	100

This indicates that the food components provide only a minor stabilizing effect on the formed particles in stomach and intestine. Also, the characteristics of the larger particles are independent of the presence of food components after passing stomach and intestine (Figure 45). The variation of the yield for the conversion of silver ions to particles shows the same trend as without food components: in saliva a high yield of 89 % is observed, whereas this decreases to 34 % in stomach. In intestine a full conversion is determined.

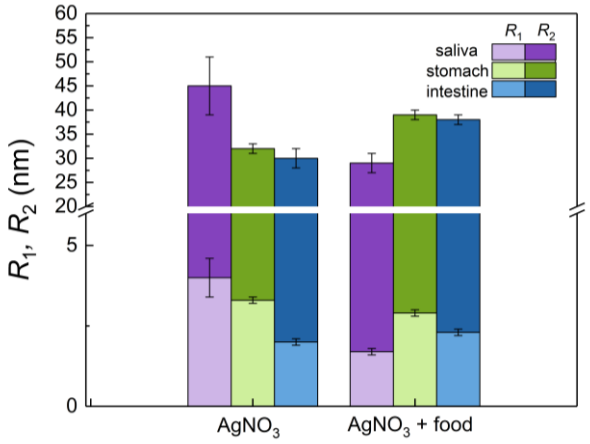

Figure 45. Mean volume-weighted radii of the small particles R_1 and of the larger particles R_2 formed during the digestion of $AgNO_3$ and $AgNO_3$ in the presence of food components. The radii are displayed according to the digestion steps: saliva, stomach and intestine (purple, green, and blue bars, respectively).

The composition of the particles remains an open question. The assumption of Walczak et al. that their particles consist of AgCl and Ag_2S, is based on energy dispersive X-ray spectroscopy (EDX) data. The EDX signals corresponded to silver, sulphur and chlorine species located at and nearby the particles. These findings need to be interpreted with caution since EDX provides only information on the elements located within the measured area. The electron beam cannot be focused on a single particle and, therefore, includes also signals of the surrounding environment. To elucidate the composition of the formed nanoparticles, we measured WAXS of the formed particles to reveal their crystalline structure. Unfortunately, the reflections of nanoparticles are very broad which often prevents an assignment of the crystal structure. Nevertheless, we can exclude the presence of AgCl and Ag_2S by direct comparison of the WAXS curve of the particles with those of suitable silver salts (AgCl, Ag_2S, Ag_2SO_4, Ag_3PO_4, AgSCN). Additionally, the off-white color of the particles proves that they cannot consist of Ag_2S (dark brown colored). Hence, also oxides can be excluded because of their black color. Silver hydroxides are formed only at basic pH values and can be ruled out

because the pH value ranged between 2.0 and 7.5 in artificial digestion. Bare silver clusters can also be excluded because of the absence of their typical plasmon resonance band at approximately 400 nm. Instead, the WAXS signal is indicative for AgSCN and we used IR spectroscopy to verify this assumption. The particles show two strong absorbance maxima at 2086 cm^{-1} and 2102 cm^{-1} as shown in Figure 46. As control, the saliva without added silver nitrate (labeled saliva blank) was measured and shows no bands in this region. IR signals at wavenumbers in the range of 2100 cm^{-1} are significant for thiocyanate compounds.[145]

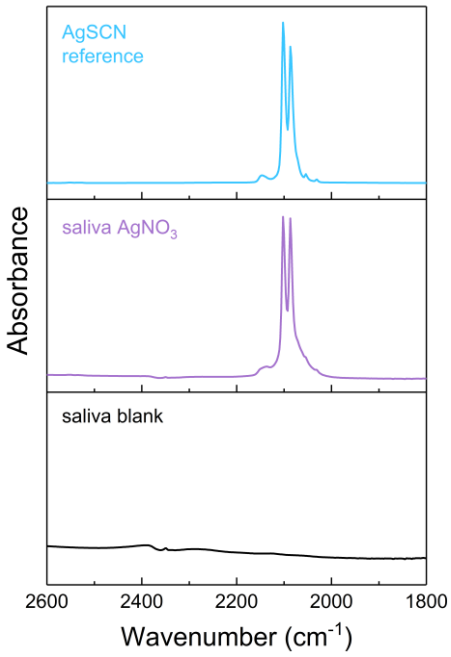

Figure 46. IR spectra of particles formed from $AgNO_3$ in saliva, control saliva (without particles/$AgNO_3$) and pure AgSCN (purple, black and blue solid lines, respectively). Strong absorption bands of AgSCN are found at 2102 cm^{-1} and 2086 cm^{-1}.

Therefore, we also measured pure silver thiocyanate which shows the same absorbance maxima as our particles. From combining WAXS and IR results we conclude that the particles are composed of silver thiocyanate. In water, AgSCN has a solubility of 1.68×10^{-4} g L^{-1} which is the lowest of the suitable silver salts. Therefore, we speculate that the AgSCN nanoparticle formation is thermodynamically driven.

This finding is not in contradiction with the results of Walczak et al. since the sulphur EDX signal is in line with the presence of AgSCN nanoparticles. Among the rare literature studies about AgSCN nanoparticles are the intended production by Yang and Ma[146] using AgCl as precursor and by Zurmühl et al.[147] who used a microemulsion process.

Author contributions: I performed the artificial digestion with the help of Maximilian Ebisch and Petra Fengler. SAXS measurements and data evaluation were done by me. I wrote the manuscript. All authors contributed to the final version of the manuscript.

5.2.5 Glutathione-Induced Disintegration of Silver Nanoparticles

This chapter is based on the paper "Kinetic monitoring of glutathione-induced silver nanoparticle disintegration", which has been partially modified and is reprinted in its original form in Appendix A.7.

When considering properties of silver nanoparticles, the type and the amount of coating ligands are of paramount importance. Ligands enable the setting of tailor-made properties, such as colloidal stability, antibacterial behavior, silver ion release kinetics and accessibility of particles' surfaces for substrates in catalytic reactions. An example for adjusting catalytic activity via choice of the ligand is the application of small silver nanoparticles with different coatings in the reduction of 4-nitrophenol (chapter 5.2.1). Here, the activity can be tuned from 436 to 77.6 L g^{-1} s^{-1} if the ligand polyacrylic acid (PAA) is replaced by glutathione (GSH).[32]

In nanoparticle research, GSH is of great interest because it is highly biocompatible and has a strong binding affinity to metal surfaces. As a natural tripeptide, GSH is the most abundant intracellular thiol with several biological functions and is the major antioxidant in liver.[148] Presumably due to its low molar mass of 307 g mol^{-1}, GSH is capable of effectively stabilizing small silver nanoparticles down to radii of about 0.5 to 1 nm.[149] These so-called silver clusters are not only of fundamental scientific interest, but are also useful for many applications,[150] such as fluorescent labels in bioimaging.[149] But besides from its undeniable advantages, GSH has some contradictory properties: under ambient conditions, a spontaneous formation of silver nanoparticles was observed when GSH is in contact with silver nitrate solutions. Furthermore, GSH was also found to induce the disintegration of silver nanoparticles.[151] Unfortunately, the role of GSH in particle formation, stabilization, and disintegration is presently unclear and, therefore, a subject of current research.

In this context, it is the aim of our study to understand the fate of silver nanoparticles in the presence of GSH. We utilized our PAA-stabilized silver nanoparticles and incubated these particles with GSH in aqueous environment, monitoring changes in the characteristics of particles with SAXS. Within this investigation, we provide a detailed insight into the disintegration of silver nanoparticles and formation of new, smaller particles.

For the initial silver nanoparticles, we used our PAA-stabilized silver nanoparticles, NP_{PAA}. After adding GSH to the particles in a molar ratio of 1 to 5 (silver atoms to GSH molecules), the mixture was incubated at a temperature of 21 °C. In accordance with the

literature,[151] we expected that GSH would continuously etch the silver nanoparticles, resulting in a decreasing radius and ending in their dissolution. SAXS was employed to follow the etching process over a period of 240 h. Radii distributions of the particles and their volume concentrations were determined from SAXS data with the help of a Monte Carlo method.[73]

A comprehensive overview on the particle population as a function of incubation time is provided in Figure 47. Therein, the initial radii distribution is monomodal, while surprisingly, the radii distribution of the incubated particles is bimodal. Radii and volume fractions of the larger particles continuously decreased while a population of small particles emerged.

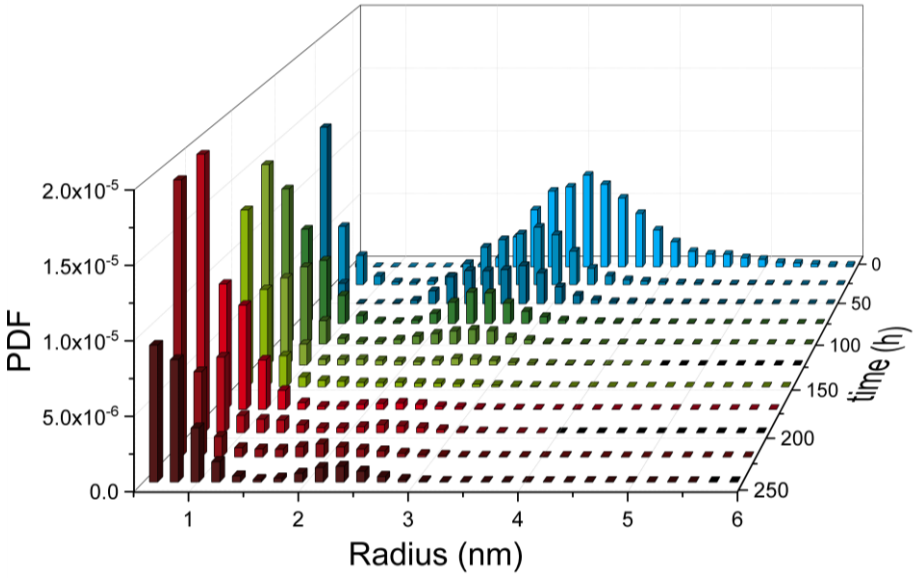

Figure 47. Glutathione-induced changes of the radii of silver particles. Presented are volume weighted partial differential functions (PDF) of the radii determined at 1, 24, 48, 72, 96, 120, 144, 168, 192, 216, and 240 h after addition of glutathione.

Examples of two typical scattering curves – one measured directly after addition of GSH and a second curve measured after 66 h incubation time – are displayed in Figure 48. The distributions are slightly asymmetric around their maxima, with tails decaying more slowly towards larger radii. Therefore, symmetric functions such as a Gaussian profile cannot be considered for their description, but a lognormal function describes the distribution sufficiently well, as confirmed earlier for the pristine particles.[128] When employing the lognormal distribution for interpretation, we found a volume-weighted mean particle radius of R = 3.22 ± 0.02 nm and a width of σ = 0.56 ± 02 nm for the pristine particles. These particles

consist of approximately 8100 silver atoms if a single silver atom requires a space of 0.0171 nm^3 as in bulk silver. In contrast, after 66 h of incubation, we determined a population of larger particles (NP_{large}) with a mean radius of $R = 2.51 \pm 0.01$ nm and a width of $\sigma = 0.43 \pm 0.01$ nm, and a second population of smaller particles (NP_{small}) with a mean radius of $R = 0.65 \pm 0.02$ nm and a width of $\sigma = 0.18 \pm 0.01$ nm. The corresponding numbers of silver atoms per particle are approximately 4000 and 60 to 70, respectively.

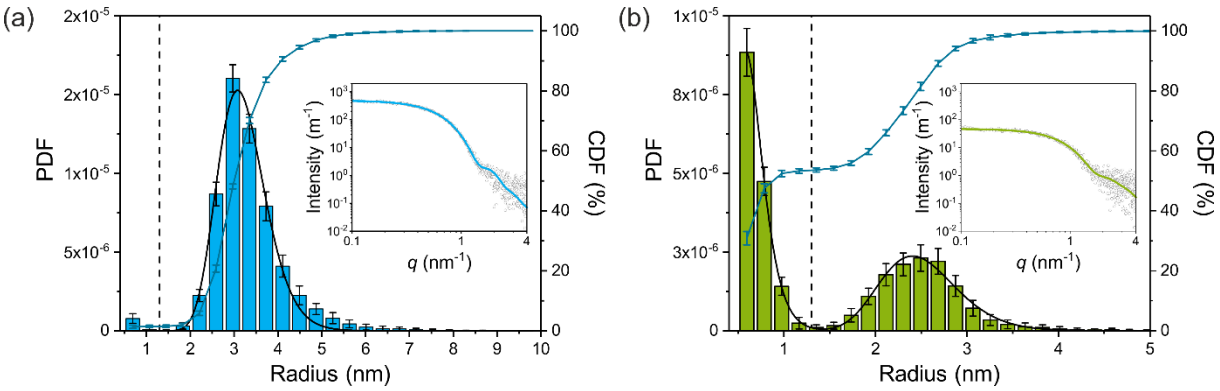

Figure 48. Volume-weighted size distributions of silver nanoparticles determined at times of $t = 0$ and 66 h after adding GSH (a and b, respectively). Displayed are partial differential functions (PDF, histograms), best fit curves using lognormal functions (solid black lines) and cumulative distribution functions (CDF, solid blue lines). PDFs are given as volume fraction, CDFs as volume fraction in percentage. Vertical dashed lines at 1.3 nm show the boundary between the two nanoparticle populations NP_{small} and NP_{large}. The insets show the SAXS data along with their best curve fits (symbols and solid lines, respectively).

Both particle populations NP_{small} and NP_{large} have a relative volume fraction of 50%, as can be seen from the CDF, and are well separated with a minimum in the PDF at about 1.3 nm. Attempts at using TEM to reveal the particle structure after incubation with GSH confirm that the particles are in the size range derived from SAXS. Unfortunately, only the particle population NP_{large} is clearly visible in the micrographs, while the population NP_{small} is below the resolution of the TEM instrument. To elucidate whether the small particle population is significant, we performed SAXS measurements with extended measurement times of 24 h. This provides higher quality data statistics to confirm the bimodal size distribution. Indeed, we found no significant difference in the resultant bimodal size distributions when short and long term SAXS measurements were used for data evaluation.

Based on the SAXS data, we can draw the hypothesis that incubation with GSH leads to the formation of "new", very small silver particles at the expense of the "old", larger

particles. Two different pathways are conceivable: i) the larger particles are "etched" and simply decrease in radius, or ii) two parallel processes take place – the etching of the larger particles and coincidently the formation of new small particles. To reveal the reaction pathway, detailed evaluations of time-dependent changes of particle radii, particle mass concentrations, particle surface areas and particle numbers are provided in the following.

As a first parameter, changes of the radii of both particle populations in dependence of incubation time were evaluated (Figure 49). The NP_{small} were first observed at an incubation time of three hours. Their median radius $R_{small} = 0.66 \pm 0.02$ nm was constant over time and showed a size distribution of moderate width (Figure 49a). In contrast, the radius of NP_{large} decreased continuously according to a power law (Figure 49b):

$$R_{\text{large}} = (3.1 \pm 0.1 \text{ nm})\, t^{-(0.063 \pm 0.003)} \tag{33}$$

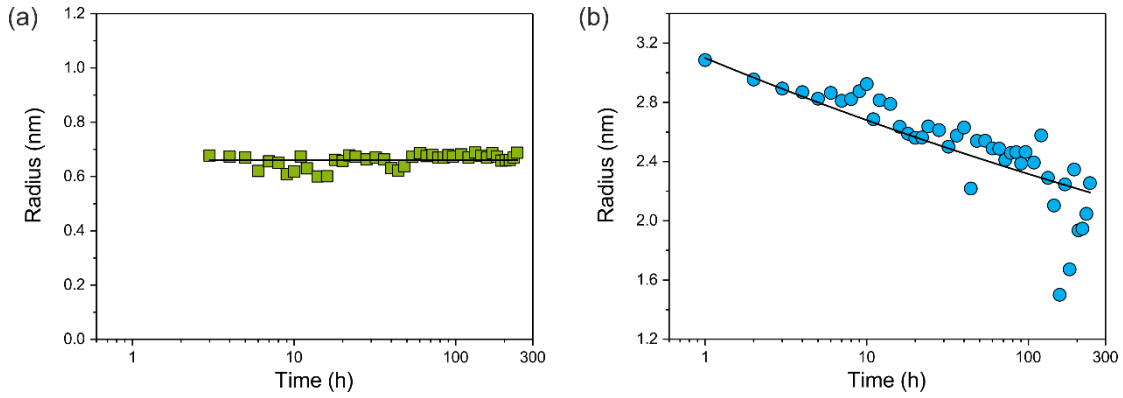

Figure 49. Radii (median values) of the two particle populations NP_{small} (a) and NP_{large} (b). Particles NP_{small} were first detected at an incubation time of 3 h and display constant radii of $R_{small} = 0.66 \pm 0.01$nm (solid black line in a). Radii of particles NP_{large} display a power law decay according to $R_{large} = R_0\, t^{-p}$ with $R_0 = 3.1$ nm and $p = 0.063 \pm 0.003$ (solid black curve in b).

While a decrease in R_{large} was expected, the finding of a constant value of R_{small} was surprising. Typically, a coalescence of particles or an Ostwald ripening occurs after nucleation of particles,[25, 152] whereas in the present study, particle growth stopped at a very early stage. The reason for this is unclear, but we speculate that these newly formed smaller nanoparticles are energetically preferred, since GSH seems to efficiently stabilize silver particles of this selected size. Our finding is consistent with results of Desireddy et al.,[153] who investigated highly stable thiolate-protected silver nanoclusters. We also assume that silver glutathione clusters containing only a few silver atoms (sub-nanometer particles) could be present during our etching experiment. In literature, clusters of 11 silver atoms are reported by Baksi et al.[154]

and clusters of 9 and 16 silver atoms are described by Yuan et al.[155] Observation of sub-nanometer particles containing only a few silver atoms is below the size detection limit of SAXS. Therefore, these sub-nanometer particles remain "invisible" to SAXS and are not included in the resulting size distribution.

For investigation of the reaction pathway, determination of changes in particle concentration of NP_{large} and NP_{small} is inevitable. Based on this, conclusions can also be drawn about the concentration of the non-detectable sub-nanometer particles. Particle concentrations were determined from SAXS data according to the procedure evaluated in our recent inter-laboratory comparison.[128] Values for NP_{small}, NP_{large} and the total particle concentration NP_{small} + NP_{large} are shown in Figure 50. The concentration of NP_{small} increased continuously, while that of NP_{large} decreased. For NP_{large}, the concentration is reduced from an initial value of approximately 0.7 g L^{-1} to a minimum concentration of 0.04 g L^{-1} at 100 – 150 h. This corresponds to a mass shrinkage of NP_{large} by 94%. In contrast, the concentration of NP_{small} reaches a limit in the range of 0.4 to 0.5 g L^{-1} at times longer than 150 h. It should be noted that a small amount of NP_{large} could still be found after an incubation period of 240 h, indicating that the particle population NP_{large} was not completely dissolved.

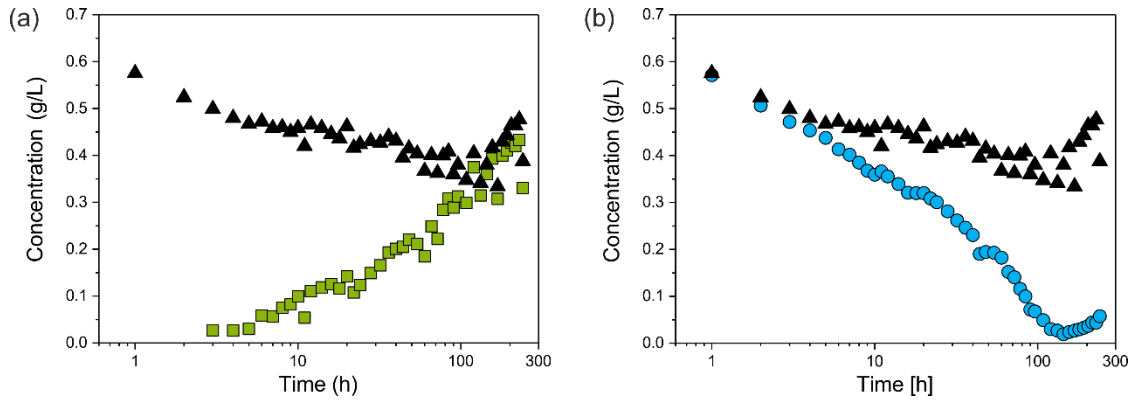

Figure 50. Mass concentration of the two particle populations NP_{small} (green squares in a) and NP_{large} (blue circles in b) as a function of incubation time. The total mass concentration $c_{total} = c_{small} + c_{large}$ is given in figures (a) and (b) for comparison (black triangles).

In addition to ambient conditions, the experiment was also carried out in absence of oxygen by using argon gas as protecting atmosphere, which resulted in no significantly different outcome. Therefore, we exclude that the presence of oxygen has a substantial influence on changes of the radii distributions. Instead, GSH seems to predominately promote

the transformation process of the particles size distribution. This finding is in accordance with a recent study of Baksi et al.,[156] who investigated the reactivity of GSH-stabilized silver clusters $Ag_{11}(GSH)_7$ and $Ag_{32}(GSH)_{32}$. They show that oxygen has no major influence on the degradation of these clusters by an excess of GSH. Conclusively, the initial concentration of NP_{large} was 0.7 g L^{-1} and the final concentration of NP_{small} is around 0.5 g L^{-1}, whereas the final concentration of NP_{large} is 0.04 g L^{-1}. Therefore, we assume that about 0.2 g L^{-1} of silver was present in form of "invisible" silver sub-nanometer particles.

An appropriate assumption is that the etching kinetics of the particles NP_{large} are strongly influenced by the surface area of particles exposed to GSH molecules. Therefore, the specific surface area of the particles per volume ($S_{V,small}$ and $S_{V,large}$) was determined as a function of time from the volume fraction of the particles (φ_{small} and φ_{large}) and the particles' median radius ($R_{V,small}$ and $R_{V,large}$) as

$$S_{V,small} = \frac{3\,\varphi_{small}}{R_{V,small}} \quad \text{and} \quad S_{V,large} = \frac{3\,\varphi_{large}}{R_{V,large}} \tag{34}$$

We found that $S_{V,small}$ of NP_{small} increases continuously with time, while $S_{V,large}$ of NP_{large} can be divided into three periods that change approximately linearly with time, as shown in Figure 51. $S_{V,large}$ decreases quickly within period 1, slowly in period 2 and stays approximately constant in period 3 (Figure 51b).

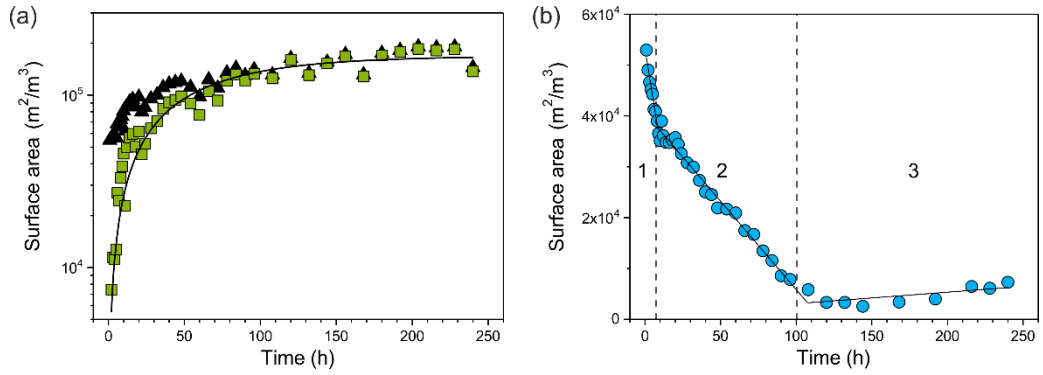

Figure 51. Changes of the surface area of particles NP_{small} (squares in a) and NP_{large} (spheres in b) as a function of time after addition of GSH. The total surface area of all particles is provided in (a) for comparison (black triangles). Solid black lines in (a) and (b) present best curve fits. The change of the surface area of NP_{large} is fitted with a piecewise linear function of different slopes in region 1, 2 and 3. The increase of the surface area of NP_{small} is fitted by an exponential function.

Linear functions were fitted for quantification of the three periods, each with a reaction constant k_i and $S_{V,large,i}(0)$ – the specific surface area extrapolated to t=0 – with i = 1,2,3:

$$S_{\mathrm{V,large,i}}(t) = S_{\mathrm{V,large,i}}(0) - k_i \cdot t \quad (35)$$

Equation (35) corresponds to reaction kinetics of zero order with respect to the specific particle surface area. Such a linear decrease of $S_{V,large}$ with time is in line with our expectations regarding the etching process. Utilizing equation (35) revealed that the initial specific surface area of NP_{large} was $S_{V,large,1}(t=0)$ = 53000 ± 1000 $m^2\ m^{-3}$. The $S_{V,large,1}(t)$ decreased with a rate constant of k_1 = 1850 ± 180 $m^2\ m^{-3}\ h^{-1}$ to $S_{V,large,1}(t_1)$ = 39900 ± 3400 $m^2\ m^{-3}$ at t_1 = 7.1 ± 0.6 h (Figure 51b). This corresponds to a surface area reduction of 25 % within period 1. $S_{V,large}$ was further reduced in period 2 with a lower rate constant of k_2 = 350 ± 10 $m^2\ m^{-3}\ h^{-1}$ down to $S_{V,large,2}(t_2)$ = 5400 ± 2100 $m^2\ m^{-3}$ at t_2 = 100.5 ± 1.7 h. Therefore, around 10 % of the initial surface area remains at the end of period 2. This value is almost constant in period 3, with a slight trend of increase with a rate constant of k_3 = 23 ± 9 $m^2\ m^{-3}\ h^{-1}$. All fitting parameters are summarized in Table 8. For interpretation of the different etching kinetics in period 1 and 2, we assumed that polyacrylic acid was firstly exchanged by GSH in period 1, because binding of the SH group of GSH to silver is much stronger than that of the carboxylic acid groups of polyacrylic acid.[63] It is reasonable that GSH acts as etching agent but also passivates the silver nanoparticle surface. An overlay of passivation and etching provides a possible explanation as to why the etching process was significantly slower in period 2 than in 1. Since NP_{large} did not disappear completely at the end of the measurement time, we conclude that a more complex reaction scenario than simple etching is present.

Table 8. Best fit parameters of the piecewise linear function applied for approximation of the change of the specific surface area $S_{v,large}$ of particles NP_{large}.

Region	Time interval (h)	$S_{v,large}(0)$ ($m^2\ m^{-3}$)	k ($m^2\ m^{-3}\ h^{-1}$)
1	$0 < t < t_1$ = 7.1 ± 0.6	53000 ± 1000	1850 ± 180
2	$t_1 < t < t_2$ = 100.5 ± 1.7	40600 ± 500	350 ± 10
3	$t_2 < t < t_3$ = 240	800 ± 400	- 23 ± 9

It has been reported in literature that silver nanoparticles can be nucleated from silver-GSH salts, which are formed by combination of silver ions and GSH in aqueous solution.[151] Similarly, this model can be adapted for the generation of GSH-stabilized silver particles

through etching of NP_{large} and the subsequent silver nanoparticle formation of NP_{small}. The change of the specific surface area of NP_{small} as a function of time can be quantified with the exponential function

$$S_{\mathrm{V,small}}(\mathrm{t}) = S_{\mathrm{V,small}}(\infty) \cdot (1 - e^{-k \cdot t}) \quad (36)$$

where $S_{V,small}(\infty)$ is the specific surface area extrapolated to infinite times and k is the rate constant of the formation of NP_{small}. Data and curve fit of equation (36) with $S_{V,small}(\infty)$ = (169 ± 6) × 10^3 m^2 m^{-3} and k = 0.0166 ± 0.0016 h^{-1} are shown in Figure 51a. Equation (36) corresponds mathematically to an equation of first order reaction kinetics for formation of the surface area of NP_{small}.[157] The observed increase of the specific surface area can be explained mechanistically analogous to silver nanoparticle formation from aqueous solutions of GSH and silver nitrate reported in literature.[151] To ensure consistency, it is of interest to calculate the theoretically possible maximum value of the particle surface as

$$S_{\mathrm{V,theory}} = \frac{3\,\varphi_{\mathrm{tot}}}{R} = \frac{3\,c_{\mathrm{Ag}}}{R \cdot \rho_{\mathrm{Ag}}}, \quad (37)$$

where a R_{small} of 0.66 nm is the radius of NP_{small}, φ_{tot} is the total volume fraction of all pristine silver nanoparticles, c_{Ag} = 0.7 g L^{-1} is the total silver concentration and ρ_{Ag} = 10.49 g cm^{-3} is the density of silver. Using these values, we calculated $S_{V,theory}$ = 3 × 10^5 m^2 m^{-3}. We conclude that about 56 % of the pristine silver nanoparticles are converted into small particles, 1 % of the silver is deposited in particles NP_{large} (with R_{large} = 2.2 nm) and the rest of the silver is present in the form of sub-nanometer silver particles. Attempts at using higher molar ratios than 5:1 of GSH to silver with the aim to completely dissolve NP_{large} led to formation of a black precipitate.

Finally, we shall consider the number of particles NP_{small} and the total number of particles NP_{small} + NP_{large} (Figure 52). After 7 h, the number of NP_{small} was almost identical to the total number of particles. At this stage of reaction and also later, the contribution of NP_{small} determined the total particle number. The increase of the number of NP_{small} can be described by an exponential growth function as

$$N_{\mathrm{small}} = \Delta N_{\mathrm{small}}\,(1 - \exp[-k_{\mathrm{small}}\,t]), \quad (38)$$

with ΔN_{small} = (1.45 ± 0.07) × 10^{-4} mol L^{-1}, which corresponds to N_{small} at infinite time, and k_{small} = 0.0186 ± 0.0023 h^{-1}.

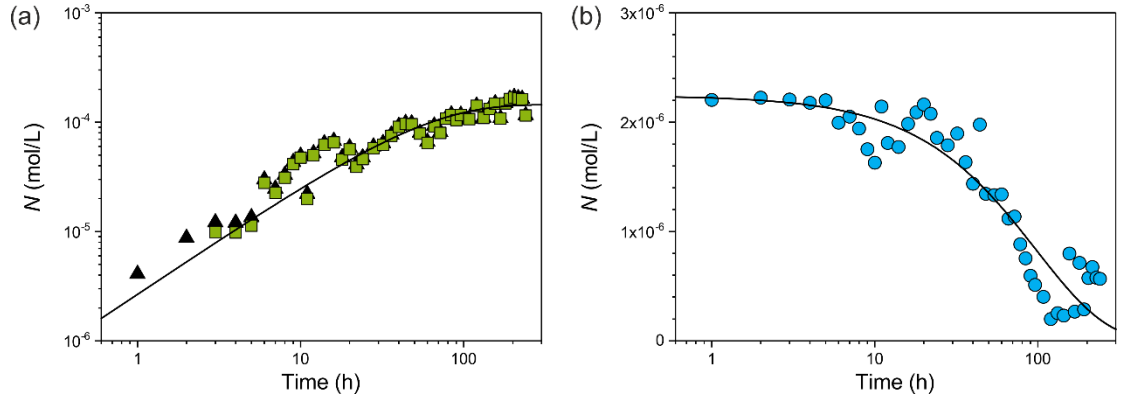

Figure 52. Changes of the number of particles NP_{small} (squares in a) and NP_{large} (spheres in b) as a function of time after the addition of GSH. The total number of all particles is provided in (a) for comparison (black triangles). The black solid line in (a) is the best curve fit of first order kinetics that describes the increase of the number of NP_{small}. The solid black line in (b) corresponds to the best curve fit of an exponential decay function with a lag time.

In analogy, the decrease of the number of NP_{large} is represented by

$$N_{\mathrm{large}} = \Delta N_{\mathrm{large}} \exp\left[-k_{\mathrm{large}} (t - t_0)\right], \quad (39)$$

with ΔN_{large} = -2.2 × 10^{-6} mol L^{-1}(N_{large} at infinite time), k_{large} = 0.0102 ± 0.004 h^{-1} and t_0 = 68 ± 6 h. The t_0 indicates the delay time necessary for not only etching, but also complete dissolution of a significant number of NP_{large}.

From a combination of both processes for NP_{large} and NP_{small}, we conclude that $\Delta N_{small}/\Delta N_{large}$ = -66, which means that for each disappearing particle NP_{large}, 66 new particles of NP_{small} are formed. The ratio of the reaction constants k_{small}/k_{large} shows that the formation of NP_{small} is significantly faster than the reduction of NP_{large}. The k-values can be utilized to calculate the time τ_i required to form and dissolve 50% of the final number of particles:

$$\tau_i = \ln(2)\, k_i^{-1} \quad (40)$$

For the formation of NP_{small}, this results in τ_{small} = 37 ± 4 h. Similarly, we calculated the time τ_{large} required to dissolve 50% of the initial number of particles NP_{large}, which gives τ_{large} = 136 ± 9 h.

By combining all data derived above, we can make a hypothesis for the mechanism of the observed particle transformation as sketched in Figure 53. Therein, the transformation of NP_{large} to NP_{small} is assumed to be mediated by complexes of Ag and GSH. These sub-nanometer particles may be present in form of GSH-stabilized Ag clusters, which contain only a small number of Ag atoms. A direct transformation of NP_{large} to NP_{small} must be considered as extremely unlikely, as the total number of particles did not stay constant. Therefore, we

conclude that the reaction pathway ii), consisting of two parallel processes – dissolution and formation of NP_{large} and NP_{small}, respectively – corresponds to the most likely reaction mechanism.

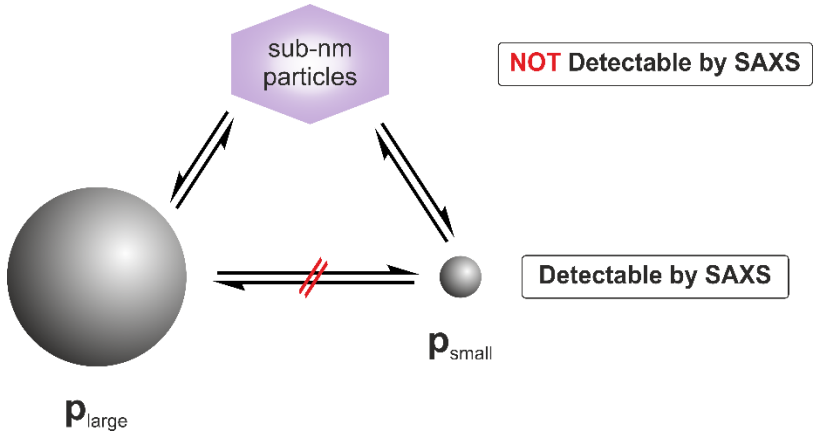

Figure 53. Sketch of the mechanism of the particle size transformation of NP_{large} to NP_{small} is assumed to be mediated by a complex of Ag and GSH. A direct transformation of NP_{large} to NP_{small} can be excluded. Particle populations of NP_{large} and NP_{small} can be detected with SAXS, while the sub-nanometer silver particles cannot be detected.

Author contributions: The general concept of the study was set up by me. SAXS measurements were performed by Patrick E. J. Saloga and I. We interpreted the SAXS data with main contributions coming from my side. Patrick E. J. Saloga and I discussed the results, and wrote the manuscript together with main contribution coming from my side. All authors contributed to the final version of the manuscript.

6 Conclusion and Perspectives

In summary, this work has demonstrated the synthesis and broad application of a versatile silver nanoparticle system. Ultra-small silver nanoparticles with a core radius of 3 nm were synthesized in large quantities, which enable their use as a standard material. The particles are stable at ambient storage conditions for more than 2 years. Initially, the particles are stabilized by PAA, which can easily be exchanged for other stabilizers to change the surface accessibility on demand, resulting in an increase or decrease of catalytic activity. This has been demonstrated by using BSA, GSH and tyrosine.

The classical synthesis was compared with microwave-assisted synthesis, which showed that the heating source and the vessel type have no substantial impact on the particle core size. In contrast, a dependence of the ligand shell thickness on the heating type was observed: microwave-assisted syntheses result in larger hydrodynamic radii than classical syntheses. Investigation of the dependence on temperature at the same reaction times showed that the particle size increases with reaction temperature. Thus, it is assumed that the growth of the particles is dominated by a temperature-dependent cluster mechanism. By increasing the reaction temperature by 50 K, the reaction time can be effectively reduced by 97%. Due to the high temperature required and the corresponding high pressure, this reaction pathway is only available with microwave reactors, which provide pressurized environments. While the size parameters derived from SAXS and DLS show no significant change, the particle losses during purification increase with increasing temperature. This indicates that time and material-saving reaction routes should be weighed up against each other. Potential specific or non-thermal microwave effects could not be observed during these experiments.

The PAA-stabilized particles were used in the first inter-laboratory comparison for the determination of precision and accuracy of SAXS instruments. Due to the high stability and

location at the lower end of the nanoscale, the particles were proven to be a suitable calibration standard. The inter-laboratory comparison showed that SAXS is a suitable technique for the precise and accurate determination of nanoparticle size distributions and particle concentrations. The results were independent on the type of instrument used. Different software tools are available for the data evaluation, which all give consistent findings.

The exchange of the stabilizing ligand of the silver nanoparticles gives the opportunity to increase biocompatibility and change the particle surface on demand. It was demonstrated that the catalytic activity of the particles in the reduction of 4-nitrophenol to 4-aminophenol differs strongly depending on the applied ligand. The initial PAA-stabilized particles display the highest known catalytic activity of silver nanoparticles to date. In contrast, the BSA and GSH-stabilized particles show substantially lower activities. It is assumed that PAA provides a high surface accessibility for the reactants, which together with the small size of the particles, results in a high catalytic activity.

As a first step in the direction of biological applications, the binding behavior of fluorescent ligands with the silver nanoparticles has been evaluated. The process of ligand adsorption and desorption of BSA-FITC and tyrosine has been monitored by DLS, SAXS and fluorescence spectroscopy. It was established that tyrosine shows substantially faster adsorption kinetics, whereas the ligand adsorption of BSA-FITC takes at least three days. For BSA-FITC, the amount of stabilizer corresponds to a monolayer, whereas tyrosine forms a multi-layered hard and soft corona. In a desorption experiment, BSA-FITC exhibited a long residence time in the range of days, in contrast to tyrosine which desorbs as fast as it adsorbs. Therefore, the BSA-FITC-stabilized particles are suitable for application in biological studies. As an example, data from human HepG2 and Caco-2 cells were provided. The Caco-2 cells show no uptake or incorporation of silver nanoparticles, whereas silver nanoparticles were already found in HepG2 cells after 2 h.

For the investigation of transformations of the silver nanoparticles after oral ingestion, an artificial digestion procedure was set up consisting of three steps: saliva, stomach and intestine. This investigation proved that the particle sizes are nano-scaled throughout the process, but undergo a transformation in the ratio of primary particles and aggregates. Furthermore, different food components were tested for their influence on the size distribution, and it was found that skimmed milk powder exhibits a stabilizing effect, mainly

caused by the proteins it contains. In this case, the size distribution did not change substantially, whereas the addition of oil or starch resulted in changes in the radii distribution and partial disaggregation. Therefore, it can be concluded that the addition of food components has a strong impact on the size distribution of silver nanoparticles during digestion.

Furthermore, the artificial digestion was repeated with silver nitrate as a sample to investigate possible particle formation processes initiated by silver ions during digestion. This is the first study to characterize the emergent particles directly in digestive media. Nanoparticles were formed in saliva and are present during the entire digestion process. The particles displayed a bimodal size distribution consisting of small particles with radii in the range of 1.5 – 4 nm and narrow size distribution, and large particles with radii in the range of 30 – 50 nm. The composition of the particles was evaluated by WAXS and IR spectroscopy. The formed particles are silver thiocyanate nanoparticles. The addition of food components did not result in significant changes, except for the particles in saliva.

The transformation of silver nanoparticles in silver ions and vice versa is a central topic for biological applications. Thus, an investigation into the interaction of silver nanoparticles with GSH was conducted. For high concentrations of GSH to silver (5:1), an etching process of PAA-stabilized silver nanoparticles with concurrent formation of new smaller silver nanoparticles was observed by SAXS. The etching process follows zero order kinetics and can be divided into three periods: a fast etching in period one which is based on the exchange of PAA with GSH, a slow etching in period two where passivation through GSH hinders etching, and a steady-state situation in period three. At the same time, the formation of very small nanoparticles is observed, which follows first order kinetics.

In conclusion, I would like to take a look at the bigger picture and classify the contemporary role of silver nanoparticles in the field of nanomaterials. This thesis focuses on an in-depth characterized material, for which a deep insight into the structure-activity relationship regarding size and surface functionality has been obtained. It should be emphasized that this silver nanoparticle system exhibits long-term stability (> 2 years), which is rarely found for nanoparticles of such a small size. We demonstrated that ultra-small silver nanoparticles display outstanding properties, for example the high catalytic activity in the reduction of 4-nitrophenol. Although other nanomaterials, e.g. gold or palladium

nanoparticles, exhibit higher catalytic activities, silver is comparably cheap and therefore ideally suited for broad commercial applications. The affordability and specific properties have already led to the use of silver in a wide range of commercial products, which will further increase in the future.

Additionally, we could demonstrate that with the help of SAXS, nanomaterials can be investigated *in situ* and *ex situ*. SAXS enables the investigation of systems in complex media, which will be important for future biological studies, since it allows the direct monitoring of changes without a distortion of the specific environment. Of course, this work cannot completely answer the question of the toxicity of silver nanoparticles; however, it provides a first attempt to improve the comparability of future biological and toxicological investigations through the utilization of a thoroughly characterized material (Figure 54).

In the future, this silver nanoparticle system can be used as an international reference material for three different purposes: i) consistent determination of size, size distribution widths and concentration with different analytical techniques, ii) further development of nanoparticles in relevant catalytical processes, iii) enhancement of comparability of toxicological investigations *in vitro* as well as *in vivo*. The last point is particularly important, because the toxicity of silver nanoparticles is still under controversial debate. In this respect, the opportunity to directly investigate nanoparticles and their changes using SAXS in complex media such as digestive juice could be extended to other biological media like blood, food components etc.

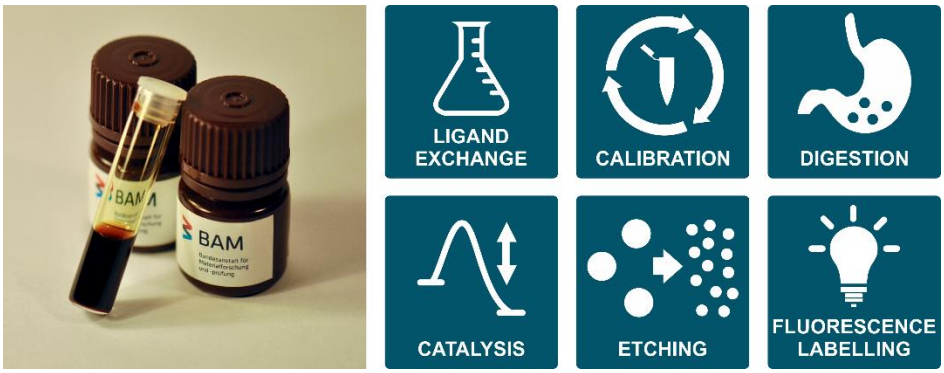

Figure 54. Left: picture of the synthesized PAA-stabilized silver nanoparticles. Right: applications of the particles which were investigated in this thesis.

7 Bibliography

1. Hu, Y.; Ge, J.; Lim, D.; Zhang, T.; Yin, Y., Size-controlled synthesis of highly water-soluble silver nanocrystals. *J. Solid State Chem.* **2008,** *181*, 1524-1529.
2. The Nanodatabase: http://nanodb.dk/en/ (accessed on 05.04.2018).
3. Nowack, B.; Krug, H. F.; Height, M., 120 Years of Nanosilver History: Implications for Policy Makers. *Environ. Sci. Technol.* **2011,** *45*, 1177-1183.
4. Chaloupka, K.; Malam, Y.; Seifalian, A. M., Nanosilver as a new generation of nanoproduct in biomedical applications. *Trends Biotechnol.* **2010,** *28*, 580-588.
5. Duncan, T. V., Applications of nanotechnology in food packaging and food safety: Barrier materials, antimicrobials and sensors. *J. Colloid Interface Sci.* **2011,** *363*, 1-24.
6. Rogers, K. R.; Bradham, K.; Tolaymat, T.; Thomas, D. J.; Hartmann, T.; Ma, L.; Williams, A., Alterations in physical state of silver nanoparticles exposed to synthetic human stomach fluid. *Sci. Total Environ.* **2012,** *420*, 334-339.
7. Windler, L.; Height, M.; Nowack, B., Comparative evaluation of antimicrobials for textile applications. *Environ. Int.* **2013,** *53*, 62-73.
8. Haase, A.; Rott, S.; Mantion, A.; Graf, P.; Plendl, J.; Thünemann, A. F.; Meier, W. P.; Taubert, A.; Luch, A.; Reiser, G., Effects of Silver Nanoparticles on Primary Mixed Neural Cell Cultures: Uptake, Oxidative Stress and Acute Calcium Responses. *Toxicol. Sci.* **2012,** *126*, 457-468.
9. Xiu, Z.-m.; Zhang, Q.-b.; Puppala, H. L.; Colvin, V. L.; Alvarez, P. J. J., Negligible Particle-Specific Antibacterial Activity of Silver Nanoparticles. *Nano Lett.* **2012,** *12*, 4271-4275.
10. Wijnhoven, S. W. P.; Peijnenburg, W. J. G. M.; Herberts, C. A.; Hagens, W. I.; Oomen, A. G.; Heugens, E. H. W.; Roszek, B.; Bisschops, J.; Gosens, I.; Van De Meent, D.; Dekkers, S.; De Jong, W. H.; van Zijverden, M.; Sips, A. J. A. M.; Geertsma, R. E., Nano-silver – a review of available data and knowledge gaps in human and environmental risk assessment. *Nanotoxicol.* **2009,** *3*, 109-138.
11. Glover, R. D.; Miller, J. M.; Hutchison, J. E., Generation of Metal Nanoparticles from Silver and Copper Objects: Nanoparticle Dynamics on Surfaces and Potential Sources of Nanoparticles in the Environment. *ACS Nano* **2011,** *5*, 8950-8957.
12. Feynman, R. P., There's plenty of room at the bottom. In *Feynman and computation*, Anthony, J. G. H., Ed. Perseus Books: 1999; 63-76.
13. Royal Society; Royal Academy of Engineering, Nanoscience and Nanotechnologies: Opportunities and Uncertainties. Royal Society: 2004.

14. Lu, Y.; Wang, Y.; Chen, W., Silver nanorods for oxygen reduction: Strong effects of protecting ligand on the electrocatalytic activity. *J. Power Sources* **2011,** *196*, 3033-3038.
15. Rossetti, R.; Nakahara, S.; Brus, L. E., Quantum size effects in the redox potentials, resonance Raman spectra, and electronic spectra of CdS crystallites in aqueous solution. *J. Chem. Phys.* **1983,** *79*, 1086-1088.
16. van Dijk, W. D.; Gopal, S.; Scheepers, P. T. J., Nanoparticles in cigarette smoke; real-time undiluted measurements by a scanning mobility particle sizer. *Anal. Bioanal. Chem.* **2011,** *399*, 3573-3578.
17. Liz-Marzán, L. M., Nanometals: Formation and color. *Mater. Today* **2004,** *7*, 26-31.
18. Wang, Y.; Xia, Y., Bottom-Up and Top-Down Approaches to the Synthesis of Monodispersed Spherical Colloids of Low Melting-Point Metals. *Nano Lett.* **2004,** *4*, 2047-2050.
19. Mijatovic, D.; Eijkel, J. C. T.; van den Berg, A., Technologies for nanofluidic systems: top-down vs. bottom-up-a review. *Lab Chip* **2005,** *5*, 492-500.
20. Verma, S.; Gokhale, R.; Burgess, D. J., A comparative study of top-down and bottom-up approaches for the preparation of micro/nanosuspensions. *Int. J. Pharm.* **2009,** *380*, 216-222.
21. Park, J.; Joo, J.; Kwon, S. G.; Jang, Y.; Hyeon, T., Synthese monodisperser sphärischer Nanokristalle. *Angew. Chem.* **2007,** *119*, 4714-4745.
22. LaMer, V. K.; Dinegar, R. H., Theory, Production and Mechanism of Formation of Monodispersed Hydrosols. *J. Am. Chem. Soc.* **1950,** *72*, 4847-4854.
23. Ostwald, W., Über die vermeintliche Isomerie des roten und gelben Quecksilberoxyds und die Oberflächenspannung fester Körper. *Z. Phys. Chem.* **1900,** *34U*, 495-503.
24. Murray, C. B.; Kagan, C. R.; Bawendi, M. G., Synthesis and Characterization of Monodisperse Nanocrystals and Close-Packed Nanocrystal Assemblies. *Annu. Rev. Mater. Sci.* **2000,** *30*, 545-610.
25. Polte, J.; Tuaev, X.; Wuithschick, M.; Fischer, A.; Thuenemann, A. F.; Rademann, K.; Kraehnert, R.; Emmerling, F., Formation Mechanism of Colloidal Silver Nanoparticles: Analogies and Differences to the Growth of Gold Nanoparticles. *ACS Nano* **2012,** *6*, 5791-5802.
26. Alexander, J. W., History of the Medical Use of Silver. *Surg. Infect.* **2009,** *10*, 289-292.
27. Lea, M. C., On allotropic forms of silver. *AmJS* **1889,** *Series 3 Vol. 38*, 47-49.
28. Calderón-Jiménez, B.; Johnson, M. E.; Montoro Bustos, A. R.; Murphy, K. E.; Winchester, M. R.; Vega Baudrit, J. R., Silver Nanoparticles: Technological Advances, Societal Impacts, and Metrological Challenges. *Front. Chem.* **2017,** *5*, 1-26.
29. Alshehri, A. H.; Jakubowska, M.; Młożniak, A.; Horaczek, M.; Rudka, D.; Free, C.; Carey, J. D., Enhanced Electrical Conductivity of Silver Nanoparticles for High Frequency Electronic Applications. *ACS Appl. Mater. Interfaces* **2012,** *4*, 7007-7010.
30. Yeshchenko, O. A.; Dmitruk, I. M.; Alexeenko, A. A.; Kotko, A. V., Surface plasmon as a probe for melting of silver nanoparticles. *Nanotechnology* **2010,** *21*, 045203.
31. Zheng, Z.; Huang, Q.; Guan, H.; Liu, S., In situ synthesis of silver nanoparticles dispersed or wrapped by a Cordyceps sinensis exopolysaccharide in water and their catalytic activity. *RSC Advances* **2015,** *5*, 69790-69799.
32. Kästner, C.; Thünemann, A. F., Catalytic Reduction of 4-Nitrophenol Using Silver Nanoparticles with Adjustable Activity. *Langmuir* **2016,** *32*, 7383-7391.
33. Aussenegg, F.; Ditlbacher, H., Plasmonen als Lichttransporter: Nanooptik. *Phys. Unserer Zeit* **2006,** *37*, 220-226.

34. Garcia, M. A., Surface plasmons in metallic nanoparticles: fundamentals and applications. *J. Phys. D: Appl. Phys.* **2012,** *45*, 389501.
35. Eustis, S.; El-Sayed, M. A., Why gold nanoparticles are more precious than pretty gold: Noble metal surface plasmon resonance and its enhancement of the radiative and nonradiative properties of nanocrystals of different shapes. *Chem. Soc. Rev.* **2006,** *35*, 209-217.
36. Willets, K. A.; Van Duyne, R. P., Localized Surface Plasmon Resonance Spectroscopy and Sensing. *Annu. Rev. Phys. Chem.* **2007,** *58*, 267-297.
37. Lee, P. C.; Meisel, D., Adsorption and surface-enhanced Raman of dyes on silver and gold sols. *J. Phys. Chem.* **1982,** *86*, 3391-3395.
38. Creighton, J. A.; Blatchford, C. G.; Albrecht, M. G., Plasma resonance enhancement of Raman scattering by pyridine adsorbed on silver or gold sol particles of size comparable to the excitation wavelength. *J. Chem. Soc., Faraday Trans. 2* **1979,** *75*, 790-798.
39. Mafuné, F.; Kohno, J.-y.; Takeda, Y.; Kondow, T.; Sawabe, H., Structure and Stability of Silver Nanoparticles in Aqueous Solution Produced by Laser Ablation. *J. Phys. Chem. B* **2000,** *104*, 8333-8337.
40. Huang, H. H.; Ni, X. P.; Loy, G. L.; Chew, C. H.; Tan, K. L.; Loh, F. C.; Deng, J. F.; Xu, G. Q., Photochemical Formation of Silver Nanoparticles in Poly(N-vinylpyrrolidone). *Langmuir* **1996,** *12*, 909-912.
41. Evanoff, D. D.; Chumanov, G., Synthesis and Optical Properties of Silver Nanoparticles and Arrays. *ChemPhysChem* **2005,** *6*, 1221-1231.
42. Fievet, F.; Lagier, J. P.; Figlarz, M., Preparing Monodisperse Metal Powders in Micrometer and Submicrometer Sizes by the Polyol Process. *MRS Bull.* **2013,** *14*, 29-34.
43. Dong, H.; Chen, Y. C.; Feldmann, C., Polyol synthesis of nanoparticles: status and options regarding metals, oxides, chalcogenides, and non-metal elements. *Green Chem.* **2015,** *17*, 4107-4132.
44. Holade, Y.; Sahin, E. N.; Servat, K.; Napporn, W. T.; Kokoh, B. K., Recent Advances in Carbon Supported Metal Nanoparticles Preparation for Oxygen Reduction Reaction in Low Temperature Fuel Cells. *Catalysts* **2015,** *5*.
45. Baghbanzadeh, M.; Carbone, L.; Cozzoli, P. D.; Kappe, C. O., Microwave-Assisted Synthesis of Colloidal Inorganic Nanocrystals. *Angew. Chem. Int. Ed.* **2011,** *50*, 11312-11359.
46. de la Hoz, A.; Diaz-Ortiz, A.; Moreno, A., Microwaves in organic synthesis. Thermal and non-thermal microwave effects. *Chem. Soc. Rev.* **2005,** *34*, 164-178.
47. Dallinger, D.; Irfan, M.; Suljanovic, A.; Kappe, C. O., An Investigation of Wall Effects in Microwave-Assisted Ring-Closing Metathesis and Cyclotrimerization Reactions. *J. Org. Chem.* **2010,** *75*, 5278-5288.
48. Shi, H.; Yin, Y.; Wang, A.; Fang, L.; Jiao, S., Kinetic study of the nonthermal effect of the esterification of octenyl succinic anhydride modified starch treated by microwave radiation. *J. Appl. Polym. Sci.* **2016,** *133*.
49. Obermayer, D.; Gutmann, B.; Kappe, C. O., Microwave Chemistry in Silicon Carbide Reaction Vials: Separating Thermal from Nonthermal Effects. *Angew. Chem. Int. Ed.* **2009,** *48*, 8321-8324.
50. Chernousova, S.; Epple, M., Silver as Antibacterial Agent: Ion, Nanoparticle, and Metal. *Angew. Chem. Int. Ed.* **2013,** *52*, 1636-1653.

51. Bouwmeester, H.; Poortman, J.; Peters, R. J.; Wijma, E.; Kramer, E.; Makama, S.; Puspitaninganindita, K.; Marvin, H. J. P.; Peijnenburg, A. A. C. M.; Hendriksen, P. J. M., Characterization of Translocation of Silver Nanoparticles and Effects on Whole-Genome Gene Expression Using an In Vitro Intestinal Epithelium Coculture Model. *ACS Nano* **2011,** *5*, 4091-4103.
52. Foldbjerg, R.; Jiang, X.; Miclaus, T.; Chen, C.; Autrup, H.; Beer, C., Silver nanoparticles - wolves in sheep's clothing? *Toxicol. Res.* **2015,** *4*, 563-575.
53. Franci, G.; Falanga, A.; Galdiero, S.; Palomba, L.; Rai, M.; Morelli, G.; Galdiero, M., Silver Nanoparticles as Potential Antibacterial Agents. *Molecules* **2015,** *20*, 8856-8874.
54. Gottschalk, F.; Sonderer, T.; Scholz, R. W.; Nowack, B., Modeled Environmental Concentrations of Engineered Nanomaterials (TiO2, ZnO, Ag, CNT, Fullerenes) for Different Regions. *Environ. Sci. Technol.* **2009,** *43*, 9216-9222.
55. Atiyeh, B. S.; Costagliola, M.; Hayek, S. N.; Dibo, S. A., Effect of silver on burn wound infection control and healing: Review of the literature. *Burns* **2007,** *33*, 139-148.
56. Carter, M. J.; Tingley-Kelley, K.; Warriner, R. A., III, Silver treatments and silver-impregnated dressings for the healing of leg wounds and ulcers: A systematic review and meta-analysis. *J. Am. Acad. Dermatol. 63*, 668-679.
57. Kim, T.-H.; Kim, M.; Park, H.-S.; Shin, U. S.; Gong, M.-S.; Kim, H.-W., Size-dependent cellular toxicity of silver nanoparticles. *J. Biomed. Mater. Res. A* **2012,** *100A*, 1033-1043.
58. Panáček, A.; Kvítek, L.; Smékalová, M.; Večeřová, R.; Kolář, M.; Röderová, M.; Dyčka, F.; Šebela, M.; Prucek, R.; Tomanec, O.; Zbořil, R., Bacterial resistance to silver nanoparticles and how to overcome it. *Nat. Nanotech.* **2018,** *13*, 65-71.
59. Rizzello, L.; Pompa, P. P., Nanosilver-based antibacterial drugs and devices: Mechanisms, methodological drawbacks, and guidelines. *Chem. Soc. Rev.* **2014,** *43*, 1501-1518.
60. Bruinink, A.; Wang, J.; Wick, P., Effect of particle agglomeration in nanotoxicology. *Arch. Toxicol.* **2015,** *89*, 659-675.
61. Nel, A.; Xia, T.; Mädler, L.; Li, N., Toxic Potential of Materials at the Nanolevel. *Science* **2006,** *311*, 622-627.
62. Schmid, G., Nanoparticles: From Theory to Application. Wiley-VCH Verlag GmbH & Co. KGaA: Weinheim, 2004.
63. Sperling, R. A.; Parak, W. J., Surface modification, functionalization and bioconjugation of colloidal inorganic nanoparticles. *Philos. Trans. Royal Soc. A* **2010,** *368*, 1333.
64. Pearson, R. G., Hard and soft acids and bases, HSAB, part 1: Fundamental principles. *J. Chem. Educ.* **1968,** *45*, 581.
65. ISO, Particle size analysis -- Dynamic light scattering (DLS). **2017**, International Organization for Standardization, ISO 22412:2017.
66. Hassan, P. A.; Rana, S.; Verma, G., Making Sense of Brownian Motion: Colloid Characterization by Dynamic Light Scattering. *Langmuir* **2015,** *31*, 3-12.
67. Bantz, C.; Koshkina, O.; Lang, T.; Galla, H.-J.; Kirkpatrick, C. J.; Stauber, R. H.; Maskos, M., The surface properties of nanoparticles determine the agglomeration state and the size of the particles under physiological conditions. *Beilstein J. Nanotechnol.* **2014,** *5*, 1774-1786.
68. Glatter, O., Scattering Methods and their Application in Colloid and Interface Science. Elsevier: 2018.
69. Kratky, O.; Stabinger, H., X-Ray Small-Angle Camera with Block-Collimation System an Instrument of Colloid Research. *Colloid. Polym. Sci.* **1984,** *262*, 345-360.

70. Schnablegger, H.; Singh, Y., The SAXS Guide: Getting acquainted with the principles. Anton Paar GmbH: Graz, 2011.
71. Porod, G., Die Röntgenkleinwinkelstreuung Von Dichtgepackten Kolloiden Systemen 1. Teil. *Kolloid-Zeitschrift & Zeitschrift für Polymere* **1951,** *124*, 83-114.
72. Bressler, I.; Kohlbrecher, J.; Thünemann, A. F., SASfit: a tool for small-angle scattering data analysis using a library of analytical expressions. *J. Appl. Cryst.* **2015,** *48*, 1587-1598.
73. Bressler, I.; Pauw, B. R.; Thünemann, A. F., McSAS: software for the retrieval of model parameter distributions from scattering patterns. *J. Appl. Cryst.* **2015,** *48*, 962-969.
74. Glatter, O., Determination of particle-size distribution functions from small-angle scattering data by means of the indirect transformation method. *J. Appl. Cryst.* **1980,** *13*, 7-11.
75. Ilavsky, J.; Jemian, P. R., Irena: tool suite for modeling and analysis of small-angle scattering. *J. Appl. Cryst.* **2009,** *42*, 347-353.
76. Orthaber, D.; Bergmann, A.; Glatter, O., SAXS experiments on absolute scale with Kratky systems using water as a secondary standard. *J. Appl. Cryst.* **2000,** *33*, 218-225.
77. Bressler, I.; Pauw, B. R.; Thünemann, A. F., McSAS: software for the retrieval of model parameter distributions from scattering patterns. *J. Appl. Cryst.* **2015,** *48*, 962-969.
78. Fenger, R.; Fertitta, E.; Kirmse, H.; Thunemann, A. F.; Rademann, K., Size dependent catalysis with CTAB-stabilized gold nanoparticles. *Phys. Chem. Chem. Phys.* **2012,** *14*, 9343-9349.
79. Lichtenstein, D.; Ebmeyer, J.; Knappe, P.; Juling, S.; Böhmert, L.; Selve, S.; Niemann, B.; Braeuning, A.; Thünemann, A. F.; Lampen, A., Impact of food components during in vitro digestion of silver nanoparticles on cellular uptake and cytotoxicity in intestinal cells. *Biol. Chem.* **2015,** *396*, 1255–1264.
80. DIN, Bodenbeschaffenheit - Resorptionsverfügbarkeit von organischen und anorganischen Schadstoffen aus kontaminiertem Bodenmaterial. **2004**, Deutsches Institut für Normung, DIN 19738.
81. Ehlert, S.; Taheri, S. M.; Pirner, D.; Drechsler, M.; Schmidt, H.-W.; Förster, S., Polymer Ligand Exchange to Control Stabilization and Compatibilization of Nanocrystals. *ACS Nano* **2014,** *8*, 6114-6122.
82. Lu, X.; Tan, C. Y.; Xu, J.; He, C., Thermal degradation of electrical conductivity of polyacrylic acid doped polyaniline: effect of molecular weight of the dopants. *Synth. Met.* **2003,** *138*, 429-440.
83. Yin, B.; Ma, H.; Wang, S.; Chen, S., Electrochemical Synthesis of Silver Nanoparticles under Protection of Poly(N-vinylpyrrolidone). *J. Phys. Chem. B* **2003,** *107*, 8898-8904.
84. Kumar, V.; Jolivalt, C.; Pulpytel, J.; Jafari, R.; Arefi-Khonsari, F., Development of silver nanoparticle loaded antibacterial polymer mesh using plasma polymerization process. *J. Biomed. Mater. Res. A* **2013,** *101A*, 1121-1132.
85. Chalal, S.; Haddadine, N.; Bouslah, N.; Benaboura, A., Preparation of Poly(acrylic acid)/silver nanocomposite by simultaneous polymerization–reduction approach for antimicrobial application. *J. Pol. Res.* **2012,** *19*, 24.
86. Cárdenas, G.; Muñoz, C.; Carbacho, H., Thermal properties and TGA–FTIR studies of polyacrylic and polymethacrylic acid doped with metal clusters. *Eur. Polym. J.* **2000,** *36*, 1091-1099.
87. Mulvaney, P., Surface Plasmon Spectroscopy of Nanosized Metal Particles. *Langmuir* **1996,** *12*, 788-800.

88. Selva Sharma, A.; Ilanchelian, M., Comprehensive Multispectroscopic Analysis on the Interaction and Corona Formation of Human Serum Albumin with Gold/Silver Alloy Nanoparticles. *J. Phys. Chem. B* **2015,** *119*, 9461-9476.
89. Alarcon, E.; Bueno-Alejo, C.; Noel, C.; Stamplecoskie, K.; Pacioni, N.; Poblete, H.; Scaiano, J. C., Human serum albumin as protecting agent of silver nanoparticles: role of the protein conformation and amine groups in the nanoparticle stabilization. *J. Nanopart. Res.* **2013,** *15*, 1-14.
90. Li, H.; Cui, Z.; Han, C., Glutathione-stabilized silver nanoparticles as colorimetric sensor for Ni2+ ion. *Sens. Actuators B Chem.* **2009,** *143*, 87-92.
91. Nguyen, N. T.; Nguyen, B. H.; Ba, D. T.; Pham, D. G.; Van Khai, T.; Nguyen, L. T.; Tran, L. D., Microwave-Assisted Synthesis of Silver Nanoparticles Using Chitosan: A Novel Approach. *Mater. Manuf. Processes* **2014,** *29*, 418-421.
92. Dzido, G.; Markowski, P.; Małachowska-Jutsz, A.; Prusik, K.; Jarzębski, A. B., Rapid continuous microwave-assisted synthesis of silver nanoparticles to achieve very high productivity and full yield: from mechanistic study to optimal fabrication strategy. *J. Nanopart. Res.* **2015,** *17*, 27.
93. Soliveri, G.; Ardizzone, S.; Yüksel, S.; Cialla-May, D.; Popp, J.; Schubert, U. S.; Hoeppener, S., Microwave-Assisted Silver Nanoparticle Film Formation for SERS Applications. *J. Phys. Chem. C* **2016,** *120*, 1237-1244.
94. Gedye, R. N.; Wei, J. B., Rate enhancement of organic reactions by microwaves at atmospheric pressure. *Can. J. Chem./Rev. Can. Chim.* **1998,** *76*, 525-532.
95. Kappe, C. O., Unraveling the Mysteries of Microwave Chemistry Using Silicon Carbide Reactor Technology. *Acc. Chem. Res.* **2013,** *46*, 1579-1587.
96. Clark, M. D.; Kumar, S. K.; Owen, J. S.; Chan, E. M., Focusing Nanocrystal Size Distributions via Production Control. *Nano Lett.* **2011,** *11*, 1976-1980.
97. Jiménez, J. A.; Sendova, M., Kinetics of Ag nanoparticle growth in thick SiO2 films: An in situ optical assessment of Ostwald ripening. *Mater. Chem. Phys.* **2012,** *135*, 282-286.
98. Liebig, F.; Thünemann, A. F.; Koetz, J., Ostwald Ripening Growth Mechanism of Gold Nanotriangles in Vesicular Template Phases. *Langmuir* **2016,** *32*, 10928-10935.
99. Jaqaman, K.; Loerke, D.; Mettlen, M.; Kuwata, H.; Grinstein, S.; Schmid, S. L.; Danuser, G., Robust single-particle tracking in live-cell time-lapse sequences. *Nat. Methods* **2008,** *5*, 695.
100. Linsinger, T. P. J.; Peters, R.; Weigel, S., International interlaboratory study for sizing and quantification of Ag nanoparticles in food simulants by single-particle ICPMS. *Anal. Bioanal. Chem.* **2014,** *406*, 3835-3843.
101. Montoro Bustos, A. R.; Petersen, E. J.; Possolo, A.; Winchester, M. R., Post hoc Interlaboratory Comparison of Single Particle ICP-MS Size Measurements of NIST Gold Nanoparticle Reference Materials. *Anal. Chem.* **2015,** *87*, 8809-8817.
102. Rice, S. B.; Chan, C.; Brown, S. C.; Eschbach, P.; Han, L.; Ensor, D. S.; Stefaniak, A. B.; Bonevich, J.; Vladár, A. E.; Walker, A. R. H.; Zheng, J.; Starnes, C.; Stromberg, A.; Ye, J.; Grulke, E. A., Particle size distributions by transmission electron microscopy: an interlaboratory comparison case study. *Metro* **2013,** *50*, 663.
103. Rennie, A. R.; Hellsing, M. S.; Wood, K.; Gilbert, E. P.; Porcar, L.; Schweins, R.; Dewhurst, C. D.; Lindner, P.; Heenan, R. K.; Rogers, S. E.; Butler, P. D.; Krzywon, J. R.; Ghosh, R. E.; Jackson, A. J.; Malfois, M., Learning about SANS instruments and data reduction from round robin measurements on samples of polystyrene latex. *J. Appl. Cryst.* **2013,** *46*, 1289-1297.

104. Borchert, H.; Shevchenko, E. V.; Robert, A.; Mekis, I.; Kornowski, A.; Grübel, G.; Weller, H., Determination of Nanocrystal Sizes: A Comparison of TEM, SAXS, and XRD Studies of Highly Monodisperse CoPt3 Particles. *Langmuir* **2005,** *21*, 1931-1936.
105. Rosalie, J. M.; Pauw, B. R., Form-free size distributions from complementary stereological TEM/SAXS on precipitates in a Mg–Zn alloy. *Acta Mater.* **2014,** *66*, 150-162.
106. Krumrey, M.; Gleber, G.; Scholze, F.; Wernecke, J., Synchrotron radiation-based x-ray reflection and scattering techniques for dimensional nanometrology. *Meas. Sci. Technol.* **2011,** *22*, 094032.
107. Allen, A. J.; Zhang, F.; Kline, R. J.; Guthrie, W. F.; Ilavsky, J., NIST Standard Reference Material 3600: Absolute Intensity Calibration Standard for Small-Angle X-ray Scattering. *J. Appl. Cryst.* **2017,** *50*, 462-474.
108. Brian Richard, P., Everything SAXS: small-angle scattering pattern collection and correction. *J. Phys.: Condens. Matter* **2013,** *25*, 383201.
109. Glatter, O.; Kratky, O., Small Angle X-Ray Scattering. Academic Press: London, 1982.
110. Zhang, F.; Ilavsky, J.; Long, G. G.; Quintana, J. P. G.; Allen, A. J.; Jemian, P. R., Glassy Carbon as an Absolute Intensity Calibration Standard for Small-Angle Scattering. *Metall. Mater. Trans. A* **2010,** *41*, 1151-1158.
111. Fritz, G.; Glatter, O., Structure and interaction in dense colloidal systems: evaluation of scattering data by the generalized indirect Fourier transformation method. *J. Phys.: Condens. Matter* **2006,** *18*, S2403.
112. Zhao, P.; Feng, X.; Huang, D.; Yang, G.; Astruc, D., Basic concepts and recent advances in nitrophenol reduction by gold- and other transition metal nanoparticles. *Coord. Chem. Rev.* **2015,** *287*, 114-136.
113. Gu, S.; Lu, Y.; Kaiser, J.; Albrecht, M.; Ballauff, M., Kinetic analysis of the reduction of 4-nitrophenol catalyzed by Au/Pd nanoalloys immobilized in spherical polyelectrolyte brushes. *Phys. Chem. Chem. Phys.* **2015,** *17*, 28137-28143.
114. Wunder, S.; Polzer, F.; Lu, Y.; Mei, Y.; Ballauff, M., Kinetic Analysis of Catalytic Reduction of 4-Nitrophenol by Metallic Nanoparticles Immobilized in Spherical Polyelectrolyte Brushes. *J. Phys. Chem. C* **2010,** *114*, 8814-8820.
115. Wunder, S.; Lu, Y.; Albrecht, M.; Ballauff, M., Catalytic Activity of Faceted Gold Nanoparticles Studied by a Model Reaction: Evidence for Substrate-Induced Surface Restructuring. *ACS Catal.* **2011,** *1*, 908-916.
116. Walker, J. M.; Zaleski, J. M., A simple route to diverse noble metal-decorated iron oxide nanoparticles for catalysis. *Nanoscale* **2016,** *8*, 1535-1544.
117. Lee, J.; Jang, D.-J., Highly Efficient Catalytic Performances of Eco-Friendly Grown Silver Nanoshells. *J. Phys. Chem. C* **2016,** *120*, 4130-4138.
118. Lara, L. R. S.; Zottis, A. D.; Elias, W. C.; Faggion, D.; Maduro de Campos, C. E.; Acuna, J. J. S.; Domingos, J. B., The catalytic evaluation of in situ grown Pd nanoparticles on the surface of Fe3O4@dextran particles in the p-nitrophenol reduction reaction. *RSC Advances* **2015,** *5*, 8289-8296.
119. Baruah, B.; Gabriel, G. J.; Akbashev, M. J.; Booher, M. E., Facile Synthesis of Silver Nanoparticles Stabilized by Cationic Polynorbornenes and Their Catalytic Activity in 4-Nitrophenol Reduction. *Langmuir* **2013,** *29*, 4225-4234.
120. Zhang, W.; Sun, Y.; Zhang, L., In Situ Synthesis of Monodisperse Silver Nanoparticles on Sulfhydryl-Functionalized Poly(glycidyl methacrylate) Microspheres for Catalytic Reduction of 4-Nitrophenol. *Ind. Eng. Chem. Res.* **2015,** *54*, 6480-6488.

121. Patra, S.; Pandey, A. K.; Sarkar, S. K.; Goswami, A., Wonderful nanoconfinement effect on redox reaction equilibrium. *RSC Advances* **2014,** *4*, 33366-33369.
122. Saha, S.; Pal, A.; Kundu, S.; Basu, S.; Pal, T., Photochemical Green Synthesis of Calcium-Alginate-Stabilized Ag and Au Nanoparticles and Their Catalytic Application to 4-Nitrophenol Reduction. *Langmuir* **2010,** *26*, 2885-2893.
123. Henrich-Noack, P.; Prilloff, S.; Voigt, N.; Jin, J.; Hintz, W.; Tomas, J.; Sabel, B. A., In vivo visualisation of nanoparticle entry into central nervous system tissue. *Arch. Toxicol.* **2012,** *86*, 1099-1105.
124. Kreyling, W. G.; Abdelmonem, A. M.; Ali, Z.; Alves, F.; Geiser, M.; Haberl, N.; Hartmann, R.; Hirn, S.; de Aberasturi, D. J.; Kantner, K.; Khadem-Saba, G.; Montenegro, J.-M.; Rejman, J.; Rojo, T.; de Larramendi, I. R.; Ufartes, R.; Wenk, A.; Parak, W. J., In vivo integrity of polymer-coated gold nanoparticles. *Nat. Nanotech.* **2015,** *10*, 619.
125. Chen, H.; Zou, P.; Connarn, J.; Paholak, H.; Sun, D., Intracellular dissociation of a polymer coating from nanoparticles. *Nano Res.* **2012,** *5*, 815-825.
126. Henriksen-Lacey, M.; Carregal-Romero, S.; Liz-Marzán, L. M., Current Challenges toward In Vitro Cellular Validation of Inorganic Nanoparticles. *Bioconjugate Chem.* **2017,** *28*, 212-221.
127. Saha, K.; Agasti, S. S.; Kim, C.; Li, X.; Rotello, V. M., Gold Nanoparticles in Chemical and Biological Sensing. *Chem. Rev.* **2012,** *112*, 2739-2779.
128. Pauw, B. R.; Kästner, C.; Thünemann, A. F., Nanoparticle size distribution quantification: results of a small-angle X-ray scattering inter-laboratory comparison. *J. Appl. Cryst.* **2017,** *50*, 1280-1288.
129. Ghosh, D.; Chattopadhyay, N., Gold and silver nanoparticles based superquenching of fluorescence: A review. *J. Lumin.* **2015,** *160*, 223-232.
130. Schindler, T.; Schmiele, M.; Schmutzler, T.; Kassar, T.; Segets, D.; Peukert, W.; Radulescu, A.; Kriele, A.; Gilles, R.; Unruh, T., A Combined SAXS/SANS Study for the in Situ Characterization of Ligand Shells on Small Nanoparticles: The Case of ZnO. *Langmuir* **2015,** *31*, 10130-10136.
131. Liu, X.; Guan, Y.; Ma, Z.; Liu, H., Surface Modification and Characterization of Magnetic Polymer Nanospheres Prepared by Miniemulsion Polymerization. *Langmuir* **2004,** *20*, 10278-10282.
132. Gupta, A. K.; Gupta, M., Synthesis and surface engineering of iron oxide nanoparticles for biomedical applications. *Biomaterials* **2005,** *26*, 3995-4021.
133. Thordarson, P., Determining association constants from titration experiments in supramolecular chemistry. *Chem. Soc. Rev.* **2011,** *40*, 1305-1323.
134. Walkey, C. D.; Chan, W. C. W., Understanding and controlling the interaction of nanomaterials with proteins in a physiological environment. *Chem. Soc. Rev.* **2012,** *41*, 2780-2799.
135. Miclăuş, T.; Bochenkov, V. E.; Ogaki, R.; Howard, K. A.; Sutherland, D. S., Spatial Mapping and Quantification of Soft and Hard Protein Coronas at Silver Nanocubes. *Nano Lett.* **2014,** *14*, 2086-2093.
136. Milani, S.; Baldelli Bombelli, F.; Pitek, A. S.; Dawson, K. A.; Rädler, J., Reversible versus Irreversible Binding of Transferrin to Polystyrene Nanoparticles: Soft and Hard Corona. *ACS Nano* **2012,** *6*, 2532-2541.
137. Liu, J.; Hurt, R. H., Ion Release Kinetics and Particle Persistence in Aqueous Nano-Silver Colloids. *Environ. Sci. Technol.* **2010,** *44*, 2169-2175.

138. Böhmert, L.; Girod, M.; Hansen, U.; Maul, R.; Knappe, P.; Niemann, B.; Weidner, S. M.; Thünemann, A. F.; Lampen, A., Analytically monitored digestion of silver nanoparticles and their toxicity on human intestinal cells. *Nanotoxicol.* **2014,** *8*, 631-642.
139. Gaillet, S.; Rouanet, J.-M., Silver nanoparticles: Their potential toxic effects after oral exposure and underlying mechanisms – A review. *Food Chem. Toxicol.* **2015,** *77*, 58-63.
140. Thünemann, A. F.; Rolf, S.; Knappe, P.; Weidner, S., In Situ Analysis of a Bimodal Size Distribution of Superparamagnetic Nanoparticles. *Anal. Chem.* **2009,** *81*, 296-301.
141. Sotiriou, G. A.; Pratsinis, S. E., Engineering nanosilver as an antibacterial, biosensor and bioimaging material. *Curr. Opin. Chem. Eng.* **2011,** *1*, 3-10.
142. Walczak, A. P.; Fokkink, R.; Peters, R.; Tromp, P.; Herrera Rivera, Z. E.; Rietjens, I. M. C. M.; Hendriksen, P. J. M.; Bouwmeester, H., Behaviour of silver nanoparticles and silver ions in an in vitro human gastrointestinal digestion model. *Nanotoxicol.* **2012,** *7*, 1198-1210.
143. Kästner, C.; Lichtenstein, D.; Lampen, A.; Thünemann, A. F., Monitoring the fate of small silver nanoparticles during artificial digestion. *Colloids Surf. Physicochem. Eng. Aspects* **2017,** *526*, 76-81.
144. Zhu, H.-L.; Liu, G.-F.; Meng, F.-J., Refinement of the crystal structure of silver (I) thiocyanate, AgSCN. *Z. Kristallogr. - New Cryst. Struct.* **2003,** *218*, 263-264.
145. Parry, D. B.; Harris, J. M.; Ashley, K., Multiple internal reflection Fourier transform infrared spectroscopic studies of thiocyanate adsorption on silver and gold. *Langmuir* **1990,** *6*, 209-217.
146. Yang, M.; Ma, J., Synthesis and characterizations of AgSCN nanospheres using AgCl as the precursor. *Appl. Surf. Sci.* **2009,** *255*, 9323-9326.
147. Zurmühl, C.; Wolf, S.; Feldmann, C., Microemulsion-based Synthesis of AgSCN Nanoparticles and Its Analogues. *Z. Anorg. Allg. Chem.* **2015,** *641*, 1510-1514.
148. Chen, Y.; Yang, Y.; Miller, M. L.; Shen, D.; Shertzer, H. G.; Stringer, K. F.; Wang, B.; Schneider, S. N.; Nebert, D. W.; Dalton, T. P., Hepatocyte-specific Gclc deletion leads to rapid onset of steatosis with mitochondrial injury and liver failure. *Hepatology* **2007,** *45*, 1118-1128.
149. Le Guével, X.; Spies, C.; Daum, N.; Jung, G.; Schneider, M., Highly fluorescent silver nanoclusters stabilized by glutathione: a promising fluorescent label for bioimaging. *Nano Res.* **2012,** *5*, 379-387.
150. Desireddy, A.; Conn, B. E.; Guo, J.; Yoon, B.; Barnett, R. N.; Monahan, B. M.; Kirschbaum, K.; Griffith, W. P.; Whetten, R. L.; Landman, U.; Bigioni, T. P., Ultrastable silver nanoparticles. *Nature* **2013,** *501*, 399-402.
151. Siriwardana, K.; Suwandaratne, N.; Perera, G. S.; Collier, W. E.; Perez, F.; Zhang, D., Contradictory Dual Effects: Organothiols Can Induce Both Silver Nanoparticle Disintegration and Formation under Ambient Conditions. *J. Phys. Chem. C* **2015,** *119*, 20975-20984.
152. Bartlett, T. R.; Sokolov, S. V.; Plowman, B. J.; Young, N. P.; Compton, R. G., Tracking of photochemical Ostwald ripening of nanoparticles through voltammetric atom counting. *Nanoscale* **2016,** *8*, 16177-16181.
153. Desireddy, A.; Kumar, S.; Guo, J. S.; Bolan, M. D.; Griffith, W. P.; Bigioni, T. P., Temporal stability of magic-number metal clusters: beyond the shell closing model. *Nanoscale* **2013,** *5*, 2036-2044.

154. Baksi, A.; Bootharaju, M. S.; Chen, X.; Häkkinen, H.; Pradeep, T., Ag11(SG)7: A New Cluster Identified by Mass Spectrometry and Optical Spectroscopy. *J. Phys. Chem. C* **2014,** *118*, 21722-21729.
155. Yuan, X.; Setyawati, M. I.; Tan, A. S.; Ong, C. N.; Leong, D. T.; Xie, J., Highly luminescent silver nanoclusters with tunable emissions: cyclic reduction–decomposition synthesis and antimicrobial properties. *NPG Asia Materials* **2013,** *5*, e39.
156. Baksi, A.; Bootharaju, M. S.; Chhotaray, P. K.; Chakraborty, P.; Mondal, B.; Bhat, S.; Gardas, R.; Pradeep, T., Reactivity of Monolayer Protected Silver Clusters toward Excess Ligand: A Calorimetric Study. *J. Phys. Chem. C* **2017,** *121*, 26483-26492.
157. Özkar, S.; Finke, R. G., Silver Nanoparticles Synthesized by Microwave Heating: A Kinetic and Mechanistic Re-Analysis and Re-Interpretation. *J. Phys. Chem. C* **2017,** *121*, 27643-27654.

Appendix

A.1 Catalytic Reduction of 4-Nitrophenol Using Silver Nanoparticles with Adjustable Activity

Claudia Kästner and Andreas F. Thünemann

Langmuir **2016**, 32, 7383−7391.

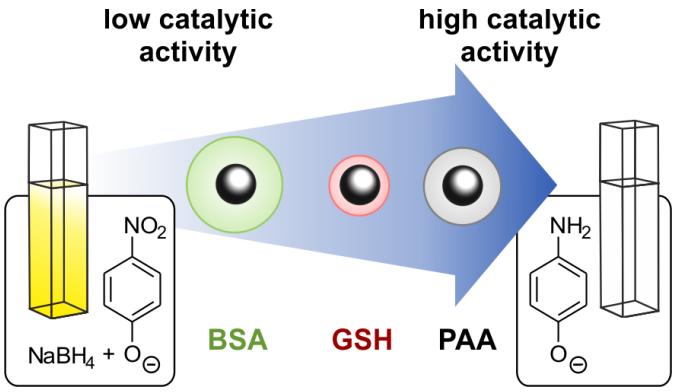

Figure A.1. Graphical abstract.

Submitted on 16 April 2016, first published on 5 July 2016 in the journal Langmuir.

An electronic version of the article is available (DOI: 10.1021/acs.langmuir.6b01477).

A.2 High-Speed but Not Magic: Microwave-Assisted Synthesis of Ultra-Small Silver Nanoparticles

Patrick E. J. Saloga,[1] Claudia Kästner,[1] and Andreas F. Thünemann

Langmuir **2018**, 34, 147−153.

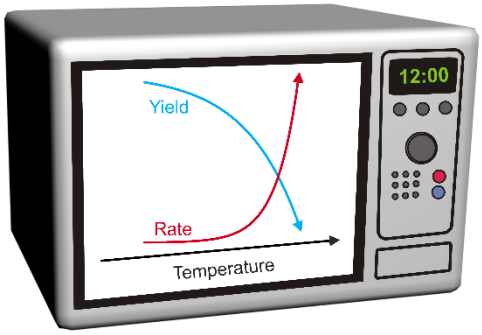

Figure A.2. Graphical abstract.

Submitted on 7 May 2017, first published on 7 December 2017 in the journal Langmuir.

An electronic version of the article is available (DOI: 10.1021/acs.langmuir.7b01541).

[1] These authors contributed equally to this work.

A.3 Nanoparticle size distribution quantification: results of a small-angle X-ray scattering inter-laboratory comparison

Brian R. Pauw, Claudia Kästner and Andreas F. Thünemann

Journal of Applied Crystallography **2017**, 50, 1280–1288.

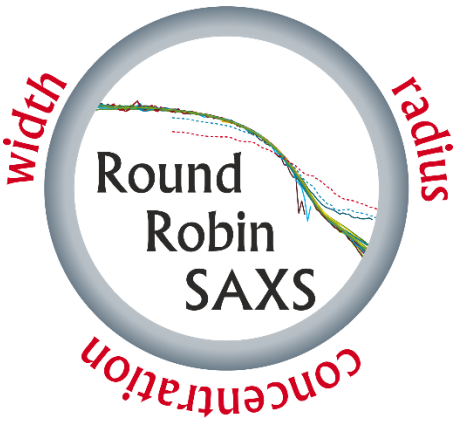

Figure A.3. Graphical abstract.

Submitted on 28 March 2017, first published on 7 July 2017 in Journal of Applied Crystallography.

An electronic version of the article is available (DOI: 10.1107/S160057671701010X).

A.4 Fate of Fluorescence Labels – Their Adsorption and Desorption Kinetics to Silver Nanoparticles

Claudia Kästner, Linda Böhmert, Albert Braeuning, Alfonso Lampen and Andreas F. Thünemann

Manuscript

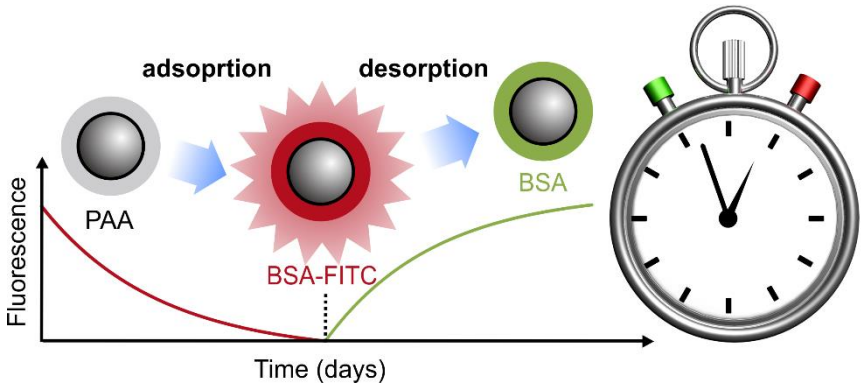

Figure A.4. Graphical abstract.

Submitted on 20 April 2018 to Langmuir (in review).

Fate of Fluorescence Labels – Their Adsorption and Desorption Kinetics to Silver Nanoparticles

Claudia Kästner[a], Linda Böhmert[b], Albert Braeuning[b], Alfonso Lampen[b] and Andreas F. Thünemann[a]*

[a]Bundesanstalt für Materialforschung und –prüfung (BAM), Unter den Eichen 87, 12205 Berlin, Germany

[b]Bundesinstitut für Risikobewertung (BfR), Max-Dohrn-Straße 8-10, 10589 Berlin, Germany

Corresponding Author

*E-mail: andreas.thuenemann@bam.de, phone: +49 3081041610

Abstract

Silver nanoparticles are among the most widely used und produced nanoparticles. Due to their frequent application in consumer products, the assessment of their toxicological potential has seen a renewed importance. A major difficulty is the traceability of nanoparticles in *in vitro* and *in vivo* experiments. Even if the particles are labeled, for example by a fluorescent marker, the dynamic exchange of ligands often prohibits their spatial localization. Our study provides an insight into the adsorption and desorption kinetics of two different fluorescent labels on silver nanoparticles with a core radius of 3 nm by dynamic light scattering (DLS), small-angle X-ray scattering (SAXS) and fluorescence spectroscopy. We used BSA-FITC and tyrosine as examples for common fluorescent ligands. It is shown that the adsorption of BSA-FITC takes at least three days whereas tyrosine adsorbs immediately. The quantitative amount of stabilizer on the particle surface was determined by fluorescence spectroscopy and revealed that the particles are stabilized by a monolayer of BSA-FITC (corresponding to 20 ± 9 molecules) whereas tyrosine forms a multilayered structure consisting of 15900 ± 200 molecules. Desorption experiments show that the BSA-FITC-stabilized particles are ideally suited for application in *in vitro* and *in vivo* experiments because the ligand desorption takes at least three days. For illustration, we provide a first application of the fluorescence-labeled particles in an uptake study with two different commonly used cell lines, the liver cell model HepG2 and human the intestinal cell model of differentiated Caco-2 cells.

Keywords: silver nanoparticles, protein adsorption, protein desorption, bio labeling, cell imaging

Introduction

During the last five years there has been a rapid rise in the use of nanomaterials in consumer products. Especially, silver nanoparticles are frequently used because of their well-known optical and antimicrobial properties.[1] The products cover a wide range from tooth pastes over children's toys to food containers.[2-3] From 2006, when ca. 25 products contained silver nanoparticles, the number of products today increased to 442 which corresponds to an 18-fold multiplication.[4-5] However, studies focusing on the toxicological potential of silver nanoparticles are highly controversial: There are investigations which claim an effect caused by the nano-scaled size of the particles, as well as studies which deny a "nano-specific effect".[6-8] As an example, De Matteis *et al.*[7] analyzed the interaction of silver nanoparticles with HeLa and A549 cells. They found that silver nanoparticles are degraded in the lysosomes and that the cell damage was predominantly caused by released silver ions, not by the nanoparticles. In contrast, Kim *et al.*[9] observed an increased cell death of MC3T3-E1 cells with decreasing size of silver nanoparticles, indicating a nano-specific effect. At the same time, both investigations suggest that the toxicology of silver nanoparticles strongly depends on their physicochemical properties and possible impurities. The main limitation is that often diverse types of nanoparticles, differing in size, surface coating and dispersity, are used. The intensive characterization needed for specific toxicological assessment is often missing and is mostly connected with high costs and effort.

The use of reference materials provides the possibility to overcome this problem. They are thoroughly characterized particles with a narrow size distribution and are available for a variety of different nanomaterials.[10] Regarding biological investigations, a fluorescent marker is often used to monitor their transport and possible degradation.[11] For this purpose, the particles' ligand shell is either exchanged for a fluorescent stabilizer or the ligand is modified to include an emissive

marker. A major challenge of fluorescence-labeled nanoparticles in biological application is: Do we see the fluorescent marker which is attached to the particle or liberated fluorescent marker? Kreyling *et al.*[12] observed for gold nanoparticles which are coated by a thio-functionalized polymer – a ligand which is known for a strong binding – a partial loss of the ligand in physiological environment.[13-14] Knowledge about the binding kinetics is important, because these markers are typically not covalently bound to the particles. Their adsorption and desorption onto the nanoparticles' surface is a dynamic process. Overall, relatively little is known about the binding behavior of fluorescent markers to nanoparticles and it is the aim of this study to contribute to this field.

Hence, we provide an investigation of the binding properties and kinetics of two different fluorescent ligands on small silver nanoparticle (Figure 1). Poly(acrylic acid) (PAA)-stabilized small silver nanoparticles are available as reference candidate material and were thoroughly characterized in a previous study.[15] The PAA ligand was exchanged for tyrosine or fluorescent-marked albumin (BSA-FITC). The adsorption of the ligands was monitored by dynamic light scattering (DLS). The fluorescent particles were characterized by small-angle X-ray scattering (SAXS), UV/Vis, and fluorescence spectroscopy. Afterwards, desorption of the ligands tyrosine and BSA-FITC was monitored by fluorescence spectroscopy showing that the BSA-FITC/particle complex exhibits sufficient stability for laboratory applications. Based on these results, the BSA-FITC-labeled nanoparticles were used in first biological applications, namely cell viability tests, cellular uptake analyses, and *in vitro* imaging.

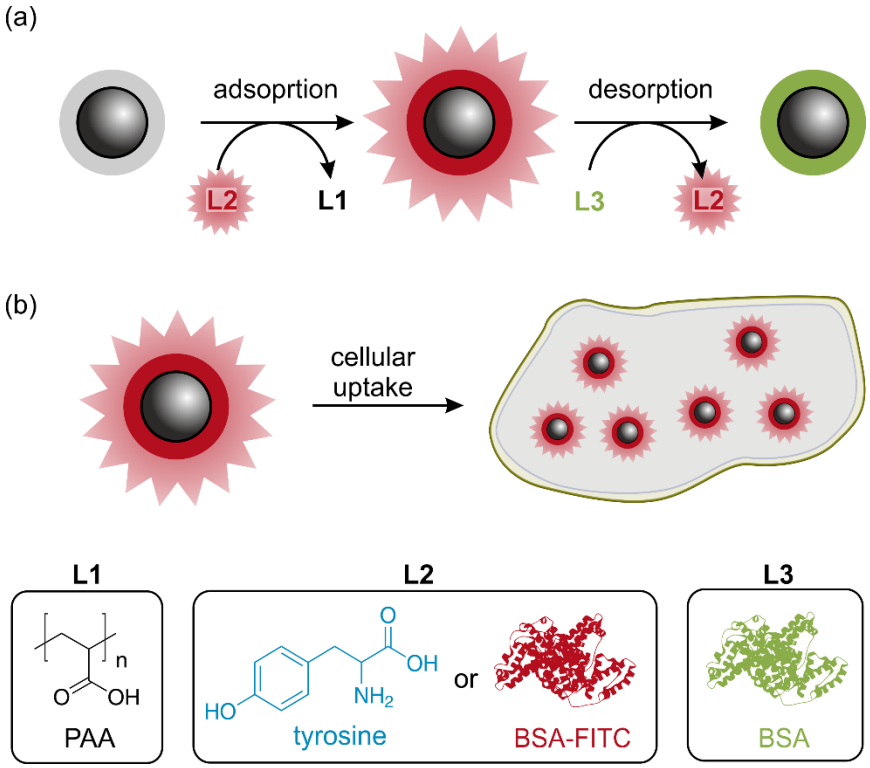

Figure 1. Scheme of adsorption and desorption experiments with the fluorescent labels tyrosine and BSA-FITC to silver nanoparticles.

Results and Discussion

Adsorption Process. The silver nanoparticles were synthesized according to an earlier reported procedure with slight modifications.[15] The particles are stabilized by poly(acrylic acid) (PAA) with an average molecular weight of 1800 g mol^{-1}. For the production of fluorescent-labeled particles, we have chosen two different molecules for ligand exchange: i.) tyrosine and ii.) BSA-FITC. Tyrosine is a non-essential amino acid and disposes a high biocompatibility. Due to the conjugation with the aromatic ring, the side chain is optically active. Typically, tyrosine is excited at wavelengths around 276 nm and emits at 310 nm. BSA-FITC is composed of the protein albumin and the fluorescent marker fluorescein isothiocyanate (FITC). BSA-FITC is excited

between 480 and 500 nm and emits at 519 nm. As depicted in Figure 2, the two fluorescent labels were chosen because they show only a small overlap of their emission spectra with the absorbance band of the silver nanoparticles. Therefore, potential quenching effects caused by the spatial proximity to the silver nanoparticles are reduced. Nevertheless, a variety of conditions and molecular interactions, for example molecular rearrangements, ground state complex formation and collisional quenching can result in fluorescence-quenching effects.[16]

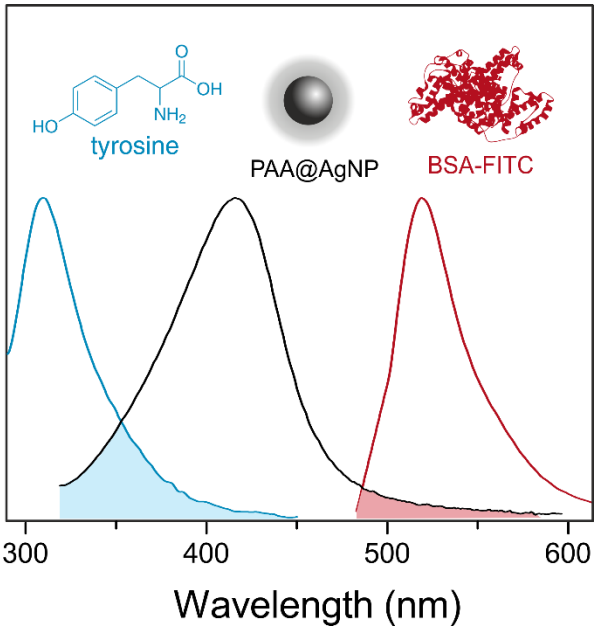

Figure 2. Normalized absorbance spectrum of PAA-stabilized silver nanoparticles (black line) and emission spectra of tyrosine (blue line) and BSA-FITC (red line) in water at 298 K. The areas where absorbance and emission spectra overlapped are marked by brighter colors.

The ligand exchange process was monitored by DLS. After addition of the new ligand the hydrodynamic radius was changing with desorption of PAA and concurrent adsorption of tyrosine or BSA-FITC (Figure 3). The initial particles showed a hydrodynamic radius of R_h = 7.1 ± 0.4 nm (Figure 3b). We observed that for tyrosine the R_h decreased to 5.5 ± 0.3 nm immediately after

addition of tyrosine. This radius did not change significantly over the time range of 196 h. In contrast, for the ligand exchange with BSA-FITC, the hydrodynamic radius increased slowly over time. Since BSA-FITC was added in excess, the reaction can be treated as a pseudo-first order reaction. Therefore, we used the following equation for data evaluation:

$$R_{\mathrm{h}}(t) = R_{\mathrm{h}}(0) + \Delta R_{\mathrm{h}}(1 - e^{-kt}) \quad (1)$$

In this equation $R_{\mathrm{h}}(0)$ is the initial hydrodynamic radius before ligand exchange, ΔR_{h} is the extrapolated increase of $R_{\mathrm{h}}(0)$ for infinite times, k is a formal rate constant and t is the experimental time in hours. The curve fit with its 95 % confidence interval is shown in Figure 3a. With the best fit value for ΔR_{h} of 3.6 ± 0.2 nm, we determined the value for the final hydrodynamic radius R_{h} = 10.7 ± 0.4 nm. This value is close to the experimental finding after three days and later. With equation (2) we calculated the time when half of the ligand on the surface of the particles is exchanged:

$$t_{1/2} = \ln(2) \cdot k^{-1} \quad (2)$$

The value for $t_{1/2}$ amounts to 26 ± 3 h for BSA-FITC. Therefore, the reaction time for a full conversion to can be expected to be around 3 days. These findings show that the rate-determining step of the ligand exchange is the adsorption of the new ligand and that the reaction is mainly independent on desorption of PAA.

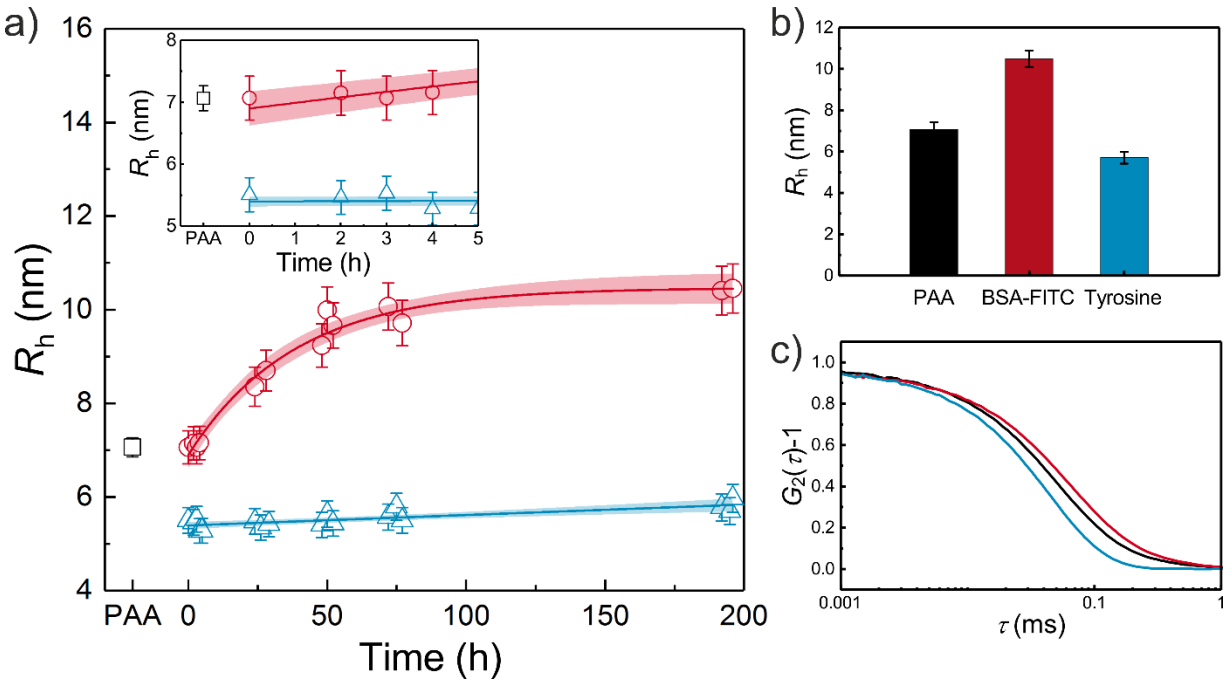

Figure 3. a) DLS results for monitoring of the ligand exchange with BSA-FITC (red), and tyrosine (blue). Time-dependent hydrodynamic radius after addition of the new ligand is marked by symbols (red circles for BSA-FITC and blue triangles for tyrosine). The resulting fit for a first order reaction is given for BSA-FITC (solid red line), whereas for tyrosine a linear fit is displayed (solid blue line). Confidence bands at a 95 % level are included (brighter areas). Inset: Detailed view of the initial hydrodynamic radius and the first 5 hours. b) Final hydrodynamic radii before and after respective ligand exchange. c) Correlation functions of the initial particles and the particles after ligand exchange.

To verify that the observed effects on the hydrodynamic radius originate from the successful ligand exchange and not from agglomeration or aggregation we used SAXS (Figure 4a). With SAXS the size of the silver core can be determined because it scatters X-rays several orders of magnitude stronger than the surrounding shell of organic molecules. An advantage of SAXS is that a statistically relevant number of particles is recorded. From the SAXS curves the volume-

weighted size distribution of the particles was calculated with the help of a Monte Carlo-based evaluation method which was proven suitable for precise size distribution quantification.[17-18] To determine the mean volume-weighted radius and the distribution width, the size distributions were approximated by a Gaussian function (Figure 4b). The mean volume-weighted radius of the initial particles was $R_{v,PAA}$=3.1 ± 0.1 nm, whereas the radii after ligand exchange with tyrosine, and BSA-FITC amounted to $R_{v,tyrosine}$ = $R_{v,BSA\text{-}FITC}$ = 3.3 ±0.1 nm. Thus, the size distribution of the particle cores did not change substantially upon ligand exchange.

The results of the SAXS evaluation are in agreement with the imaging data obtained via scanning transmission electron microscopy (STEM), as depicted in Figure 5. The particles were spherical and showed no sign of aggregation after successful ligand exchange.

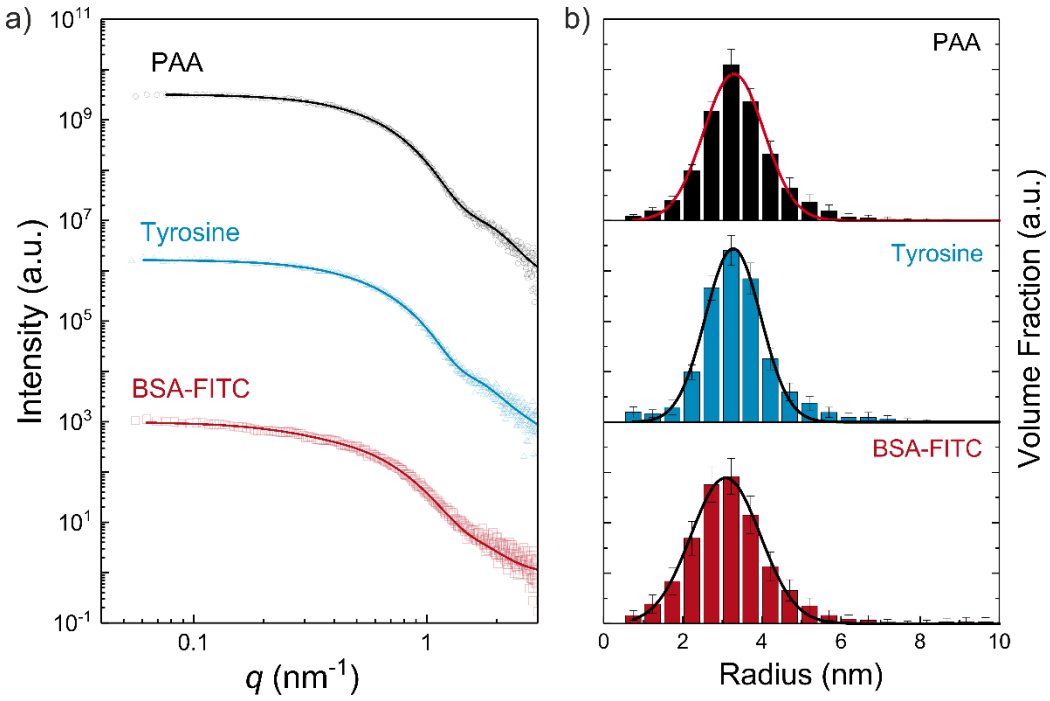

Figure 4. a) SAXS data and corresponding curve fits (symbols and solid lines, respectively) of silver nanoparticles stabilized by PAA (black), tyrosine (blue), and BSA-FITC (red). The curves are shifted vertically for better visibility. b) Volume-weighted size distributions (bars) derived

from curve fits in a). Gaussian fits of the size distributions are marked by solid lines (red for PAA, black for tyrosine and BSA-FITC).

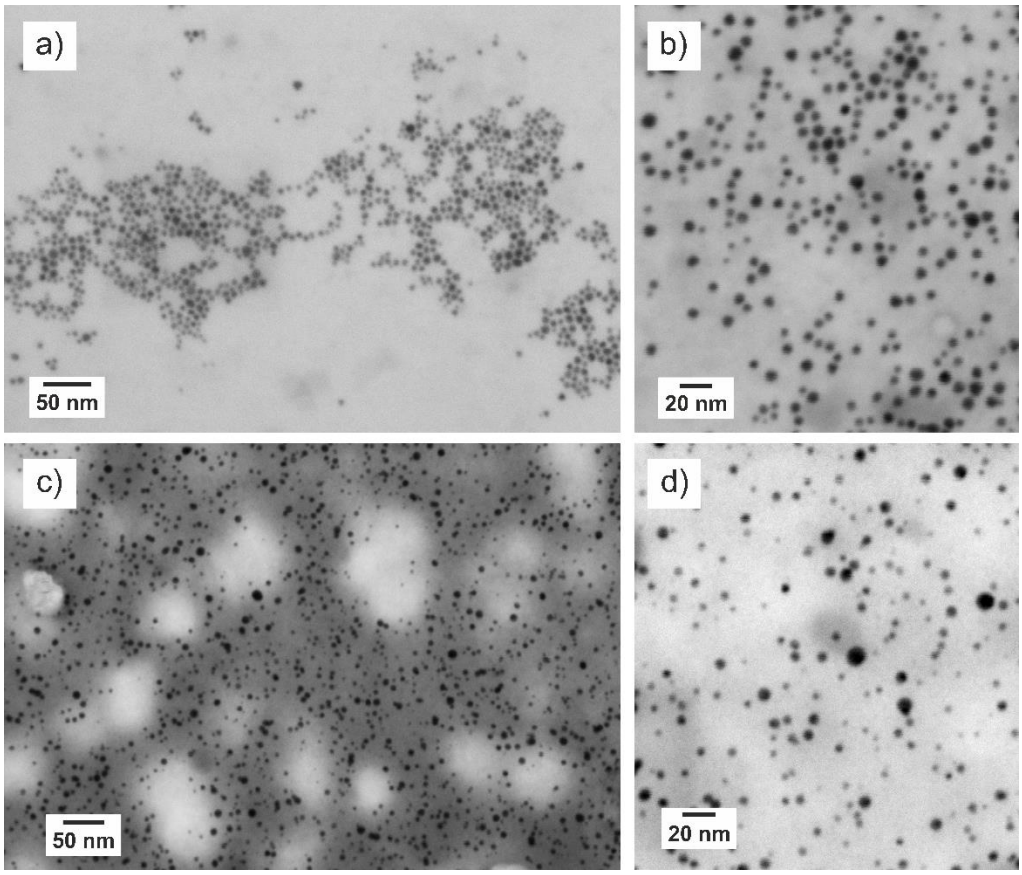

Figure 5. STEM images of the trans-functionalized silver nanoparticles at different magnifications: a) and b) show tyrosine-stabilized nanoparticles (scale bars are 50 nm and 20 nm); c) and d) show BSA-FITC-stabilized nanoparticles (scale bars are 50 nm and 20 nm) after successful ligand exchange.

The fluorescent properties of the trans-functionalized particles were characterized by fluorescence spectroscopy (Figure 6). From the comparison of the fluorescence emission spectra of the particles coated with tyrosine or BSA-FITC with their corresponding free analogs (without particles, same

concentration) we assume that the silver nanoparticles induce fluorescence quenching. This is in accordance with the literature where silver nanoparticles are described as highly efficient quencher for fluorescence.[19] We found that the fluorescence intensity of the BSA-FITC-stabilized particles was 70 % of the intensity of pure BSA-FITC at the fluorescence maximum of 520 nm. For the tyrosine-stabilized particles we observed a stronger fluorescence quenching of 54 % at the emission maximum of 310 nm. However, the remaining fluorescence intensity was intensive enough for the intended application of these particles in biological investigations.

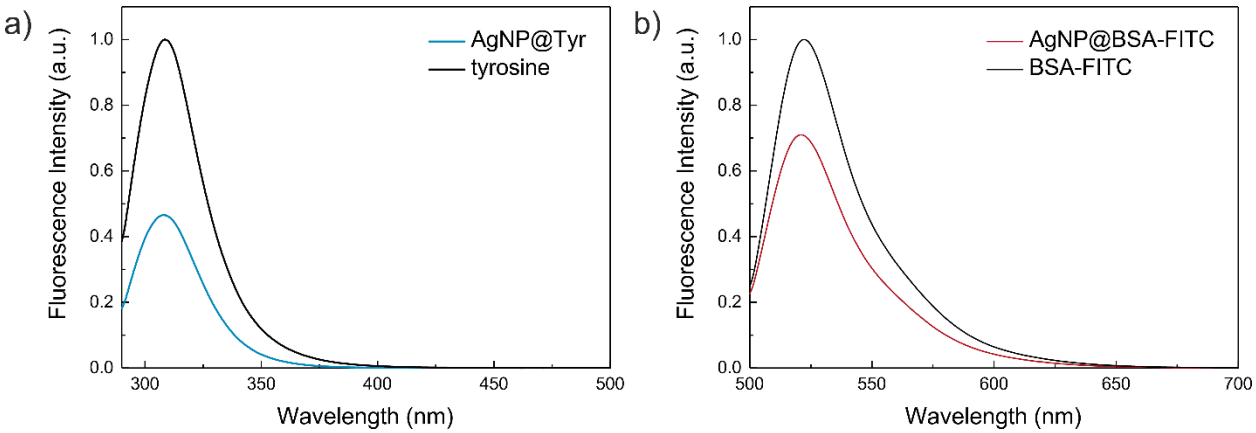

Figure 6. Fluorescence emission spectra of a) tyrosine and b) BSA-FITC (black curves) in comparison with the corresponding stabilized silver nanoparticles (blue and red curve, respectively). Excitation wavelengths were 276 nm for tyrosine and 487 nm for BSA-FITC.

A parameter of high interest is the amount of surface-bound ligand.[20-22] Especially its quantitative determination *in situ* remains challenging. We used a fluorescence titration method to elucidate this issue. With this technique the fluorescent ligand is titrated against the nanoparticles. The increase in the fluorescent signal allows the calculation of the amount of surface-bound ligand. For the adsorption of BSA-FITC, the changes in fluorescence quenching in comparison with the system without nanoparticles is displayed in Figure 7a. The fluorescence intensity reaches a limit

where the fluorescence of further added ligand is not quenched (Figure 7b). Thus, the particle surface coverage by the fluorescent BSA-FITC ligand has reached saturation and additional ligands diffuse "freely" in solution. The point where the curve of Figure 7b reaches the saturation region corresponds to the intersection of two tangents which approximate the linear curve progression in the beginning and at the end. We calculated that the silver nanoparticle surface is covered by 20 ± 9 BSA-FITC molecules.[23] This corresponds in approximation to a monolayer of the ligand (see Supporting Information).

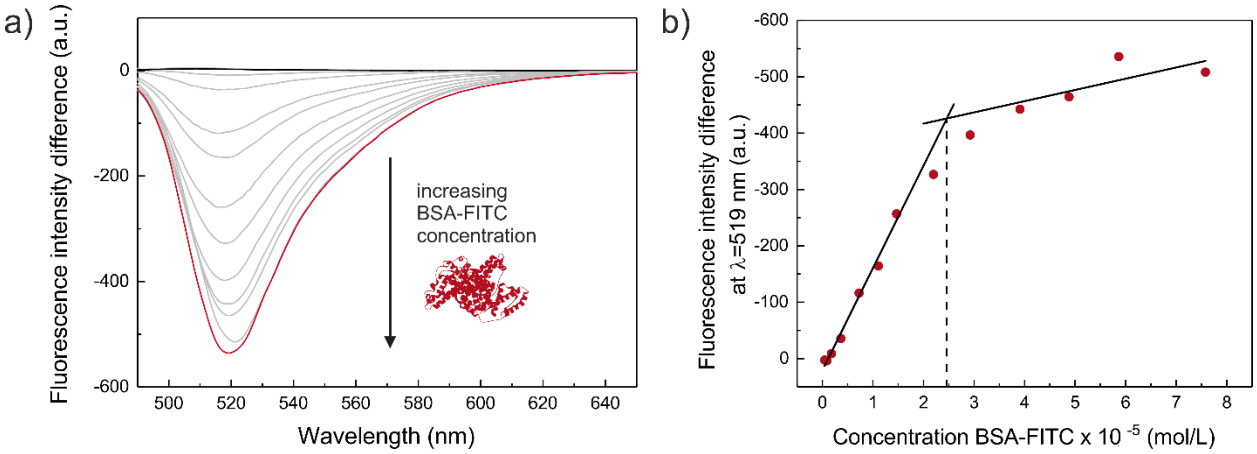

Figure 7. a) Difference of fluorescence spectra of silver nanoparticles stabilized by BSA-FITC ($I_{BSA\text{-}FITC}$) and of the system without nanoparticles (I_{ref}): $I_{BSA\text{-}FITC} - I_{ref}$. Different BSA-FITC concentrations were used, ranging from 0.5 µM (black curve) to 75.8 µM (red curve). b) Displayed are the intensities at 519 nm of a) in dependence of the BSA-FITC concentration (red circles). Crossing of the two tangents (black lines) represents the equivalence point which gives the ratio of BSA-FITC molecules per silver nanoparticle of 20 ± 9.

For the tyrosine-stabilized particles, the silver nanoparticles were titrated against a known amount of tyrosine. By a similar data evaluation as previously described, the amount of surface-bound ligand was determined (Figure 8),. For tyrosine this corresponded to an amount of 15900 ± 200

molecules per nanoparticle which would imply a multi-layered structure on the particle surface. At a first glance, the high number of tyrosine molecules is in contrast with the results of the DLS because the ligand shell should be larger than 2.2 nm (~0.6 nm would correspond to a tyrosine monolayer). A possible explanation for this discrepancy is the formation of a hard and soft corona of tyrosine similar to that reported for many proteins.[24-26] Since the nanoparticles were filtered before DLS measurements, the soft corona can be potentially sheared off during sample preparation. To verify this hypothesis, we again measured DLS of the tyrosine-stabilized nanoparticles without previous filtration. The measured hydrodynamic radius was substantially higher (R_h = 7.8 ± 0.5 nm, 4.5 nm shell thickness) and, thus, affirmed the assumption of a hard and a soft corona.

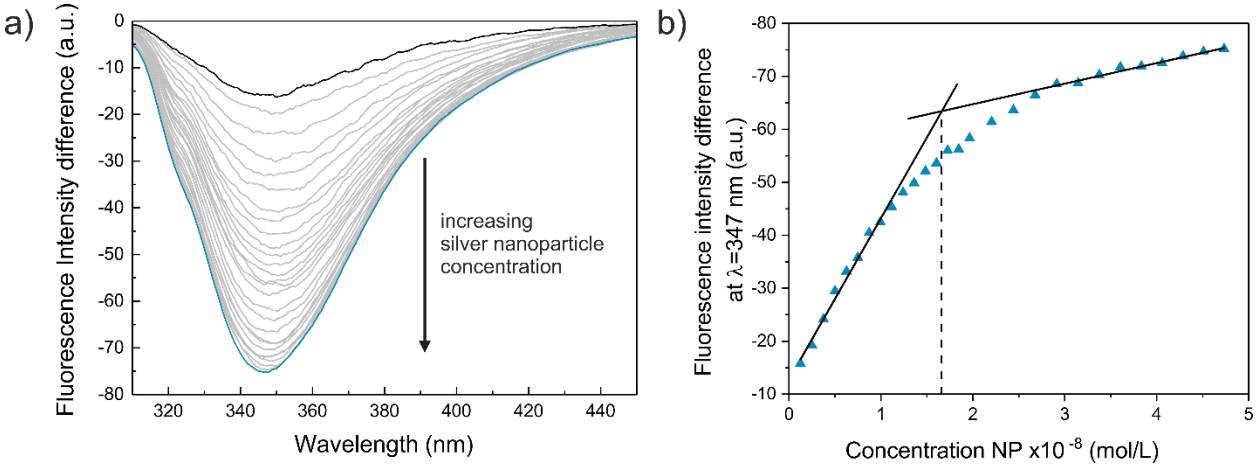

Figure 8. a) Difference of fluorescence spectra of silver nanoparticles stabilized by tyrosine (I_{tyr}) and of the system without nanoparticles (I_{ref}): I_{tyr}- I_{ref}. Silver nanoparticles were titrated against a constant tyrosine solution (silver nanoparticle concentrations ranging from 1.3 nM (black curve) to 47.3 nM (blue curve). b) Displayed are the intensities at 347 nm of a) in dependence of the silver nanoparticle concentration (blue triangles). Crossing of the two tangents (black lines) represents the equivalence point which gives the ratio of tyrosine molecules per silver nanoparticle of 15900 ±200.

Desorption Process. Toxicological studies of nanoparticles often comprise *in vitro* and *in vivo* studies where the transport, uptake, and a possible accumulation of the particles can be observed. The use of a fluorescent maker is, therefore, a common concept to provide traceability. Important information which is often not taken into account is: How long does the fluorescent marker remain on the particle surface in physiological environment? We designed an experiment to give an approximation for this time span: The BSA-FITC-stabilized particles were diluted by a concentrated (20 g/L) solution of not fluorescent-labeled BSA. Fluorescence intensity was expected to increase when BSA-FITC of a population in the vicinity to the silver core is exchanged for BSA and released into the bulk solvent, because due to the exchange, fluorescence is not quenched anymore and increases as long as BSA-FITC is released. For our experiment, we have chosen two different dilutions (1:300 and 1:3000) of the silver nanoparticles to give an insight into desorption time spans (Figure 9). As a control experiment the particles were diluted in phosphate-buffered saline (PBS) which is the matrix for BSA in the exchange experiment. Therein, the fluorescence intensity of the BSA-FITC-stabilized nanoparticles was normalized to 1 after a 1:300 dilution in PBS. The intensity of this mixture was in equilibrium instantaneously and remained constant for 12 days. In contrast, in the same time interval the fluorescence intensity of the mixture of BSA-FITC-stabilized particles with BSA increased from 0.45 to ca. 0.6 for a dilution of 1:300 and from 0.45 to 1.0 for a dilution of 1:3000. Thus, it is obvious that a very high dilution and long incubation times are needed to remove BSA-FITC from the particles.

For the quantification of the release of BSA-FITC we applied a simple model. We utilized, corresponding to the adsorption process, a similarly modified first order reaction kinetic rate equation:

$$I_f(t) = I_f(0) + \Delta I_f(1 - e^{-k\,t}) \quad (3)$$

The $I_f(t)$ is the fluorescence intensity at time *t*, $I_f(0)$ is the fluorescence intensity at $t = 0$, and ΔI_f is the extrapolated value for the increase of the fluorescence intensity for infinite time, *k* is a formal rate constant, and *t* is the experimental time in hours. In order to avoid ambiguous results we used constant values of $I_f(0) = 0.45$, and $\Delta I_f = 0.55$ to fulfill the normalization condition $I_f(0) + \Delta I_f = 1$ at infinite time. Therefore, only *k* remained as free fit parameter. The *k*-values can be utilized to calculate the time τ required to release 50 % of BSA-FITC contained in ΔI_f by

$$\tau = \ln(2) \times k^{-1} \quad (4)$$

The resultant τ-value is 21 ± 3 days for a dilution of 1:300 and 3.4 ± 0.4 days for the 1:3000 dilution. Therefore, we assume that the release of BSA-FITC from the vicinity of the silver cores is in the order of days for the high 1:3000 dilution and in the order of weeks for the lower 1:300 dilution. This shows that the binding of BSA-FITC to the particles is relatively strong. We conclude that there is no indication for a substantial risk that the BSA-FITC-stabilized particles lose their fluorescent corona due to dilution when used, for example in cell experiments for toxicological studies.

The same experiment was conducted with the tyrosine-stabilized nanoparticles where no change in the fluorescence intensity was observed. We conclude that similar to the fast adsorption of tyrosine, it is also quickly released. Additionally the stronger binding of the BSA by thiol groups outranges the adsorption of tyrosine via carbonyl groups. We conclude that the exchange of tyrosine is fully completed in the time range of seconds.

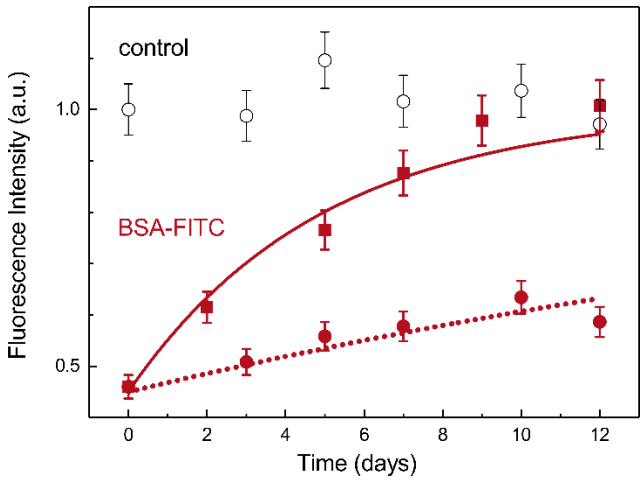

Figure 1. Fluorescence intensity at 519 nm as a function of time after mixing of BSA-FITC-stabilized silver nanoparticles with a solution of native BSA (not fluorescence-labeled) with a dilution of 1:300 (red circles) and 1:3000 (red squares), with respect to the nanoparticles. Curve fits of a pseudo first-order reaction reveal τ-values of 21 ± 3 days (1:300 dilution, dotted red line) and 3.4 ± 0.4 days (1:3000 dilution, solid red line), respectively. The results of the control experiment (mixing of BSA-FITC-stabilized silver nanoparticles with PBS) is marked by black circles.

Biological Application. On the basis of the adsorption and desorption experiments, the BSA-FITC-stabilized silver nanoparticles were proven to be suitable for the investigation of their uptake and cellular localization in *in vitro* experiments. Therefore, we selected two cell models: (1) The liver cell model HepG2, which is a very commonly used hepatocyte *in vitro* model and (2) the most common cell model for the intestinal enterocytes, differentiated Caco-2 cells. Both cell types were incubated with non-cytotoxic concentrations of BSA-FITC marked silver nanoparticles up to 24 h. Representative confocal images are given in Figure 10. They show a time-dependent uptake of silver nanoparticles in HepG2 cells with some nanoparticles having cell contact after 2 h, and numerous particles deep inside the cells after 24 h. In contrast to that, the differentiated

Caco-2 monolayer showed just a few particles in contact with the microvilli brush border on the apical side of the monolayer for all time points, and almost no particles inside the cells. Therefore, the fluorescence labeling-enabled time-dependent uptake studies showed clear differences in particle uptake for cells from different tissues.

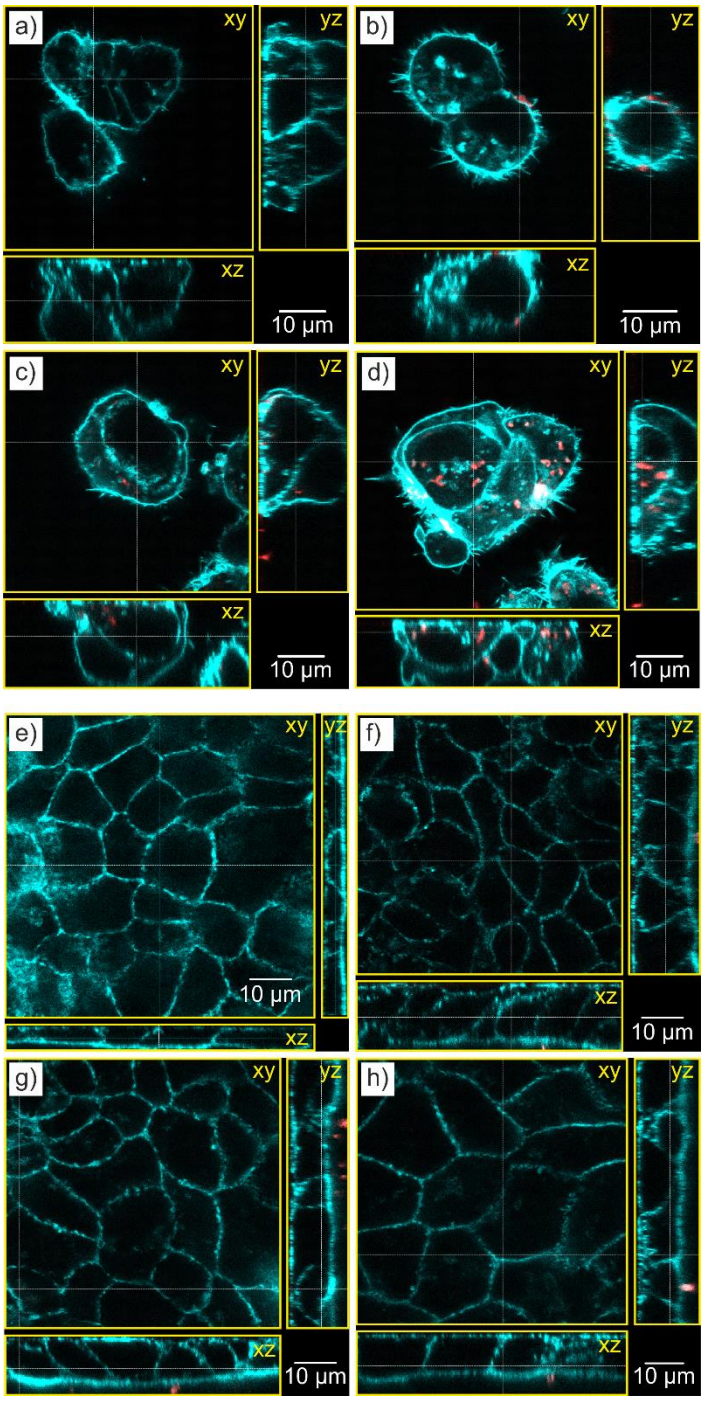

Figure 10. Confocal fluorescence microscopy images of HepG2 (a-d) and differentiated Caco-2 cells (e-h). The cell lines were incubated with BSA-FITC-stabilized particles for 2, 6, and 24 h (b-d for HepG2, and f-h for Caco-2 cells). A control sample for each cell line shows the status without silver nanoparticles (a and e). From preliminary cytotoxicity tests non-cytotoxic silver concentrations of 10 and 25 µg/ml were chosen for HepG2 and Caco-2 cells, respectively. The images show the view in xy, xz and yz direction (yellow boxes), whereas the dotted white lines mark the plane from which the other cutting planes are derived. The cytoskeleton is stained by ActinRed 555 marked with blue color, whereas the BSA-FITC-stabilized particles are marked by red color.

Conclusion

The process of fluorescent ligand adsorption and desorption on silver nanoparticles has been monitored by DLS, SAXS, and fluorescence spectroscopy. The fluorescent ligands BSA-FITC and tyrosine were compared. According to DLS, tyrosine shows substantially faster adsorption kinetics, whereas the ligand exchange with BSA-FITC takes at least three days. For BSA-FITC, the amount of stabilizer corresponds to a monolayer, whereas tyrosine shows the formation of a multi-layered hard and soft corona. In a desorption experiment, it was shown that BSA-FITC exhibits a long residence time in the range of days, in contrast to tyrosine which desorbs as fast as it adsorbs. Therefore, the BSA-FITC-stabilized particles are suitable for application in biological studies. As an example we provided data from human HepG2 and Caco-2 cells. The latter show no substantial uptake, whereas cellular uptake was found for HepG2 cells already after 2 h. The present study on persistently fluorescence-labeled silver nanoparticles opens the pathway for further, comparable biological investigations regarding uptake, excretion, or toxicity. Our

standardized and thoroughly characterized reference candidate material is well-suited for this purpose.

Materials and Methods

Materials. All chemicals were used as received without further purification. Poly(acrylic acid) (M_w = 1800 g/mol), BSA, BSA-FITC and PBS were purchased from Sigma-Aldrich, NaOH, ethylene glycol and (S)-(-)-tyrosine from Merck and silver nitrate from AppliChem. Ultrapure water was used for all preparations (Milli-Q, 18.2 mΩ at 25°C).

Synthesis of silver nanoparticles.

The synthesis of poly(acrylic acid) stabilized particles was performed according to a previous description.[27] We repeated the synthesis several times to ensure reproducibility. It will be briefly described: First, a solution of 1.9 g (11.4 mmol) silver nitrate in 58.5 mL ethylene glycol was prepared at room temperature. In a 500 mL-three-necked flask 15.7 g (217.9 mmol with respect to the monomer units) poly(acrylic acid) with an average molecular weight of M_w = 1800 g/mol were added to 291.5 mL ethylene glycol and heated under stirring to 200 °C. Afterwards, the silver nitrate solution was added within 3 s to the boiling solution under stirring. The mixture was refluxed for 15 min and then cooled to room temperature. For purification of the particles, 800 mL water (pH = 5) were added and the mixture was stored for 24 h. Thereafter, the reddish brown supernatant was decanted. This washing procedure was repeated three times. The resulting residue was suspended in 150 mL water and a 1% (w/v) sodium hydroxide solution was added dropwise until the pH of the dispersion was adjusted to a value of 10. During this procedure the color of the dispersion turned from reddish brown, via olive-green to brownish black. Finally, PAA (0.2 mmol in water) was added to provide a better long term colloidal stability. The concentration of elementary silver was determined by SAXS and amounts to 2.9 g/L.

Ligand exchange with BSA-FITC, and tyrosine.

For the ligand exchange with BSA-FITC, 1 mL of the initial particle dispersion were placed in a glass vial and a mixture of 0.5 mL BSA-FITC (0.15 µmol) and 1 mL NaOH (0.1 M) was added. The mixture was stirred for 3 days.

For the ligand exchange with tyrosine, 2.5 mL of the initial particle dispersion were placed in a vial and 1.2 mL tyrosine (24.3 mg, 0.13 mmol) in NaOH solution (1 wt%) were added under stirring.

DLS measurements. The DLS measurements were performed using a multi-angle ALV Instrument (ALV 7004, ALV Langen) equipped with a He-Ne laser (λ = 632.8 nm). Data were recorded at 23 ± 1 °C at scattering angles of 2θ = 26°-146° (8°-steps). Six measurement cycles were conducted with 60 s for each angle. For measurement the samples were diluted 1:100 with water or NaOH solution (0.1 M). Curve fitting was conducted with the software McDLS (version 1.0.1).

SAXS measurements. SAXS measurements were performed in a flow through capillary with a Kratky-type instrument (SAXSess from Anton Paar, Austria) at 21 ± 1 °C. Samples analyzed with SAXS were used as prepared and measured for 20 minutes (120 measurement frames averaged over 10 s). The measured scattering data was corrected by subtracting the data of a capillary filled with pure water. The measured intensity was converted to absolute scale according to Orthaber *et al.*[28] The scattering vector q depends on the wavelength λ of the radiation (λ = 0.154 nm), thus, $q = 4\pi/\lambda \sin\theta$. Deconvolution (slit length desmearing) of the SAXS curves was performed with the SAXS-Quant software (Anton Paar, Austria). Curve fitting was conducted with the software McSAS[18] (version 1.3).

STEM-Imaging. The STEM images were obtained from a Zeiss Gemini Supra 40 scanning electron microscope operating at transmission mode at 10-20 kV. The TEM grids were prepared by placing 2 µL of the particle dispersion on a carbon grid and drying at room temperature.

Fluorescence spectroscopy. The fluorescence measurements were performed using a Fluorolog spectrofluorometer from Horiba and a spectrofluorometer FB-6500 from Jasco. The emission spectra of tyrosine and tyrosine-stabilized particles were recorded using an excitation wavelength of 276 nm. The emission spectra of BSA-FITC and BSA-FITC-stabilized nanoparticles were recorded using an excitation wavelength of 487 nm. The dispersions were diluted with water (tyrosine), or PBS (BSA-FITC) in a ratio of 1:100. Experimental details of the titration and desorption experiments are described in the supporting information.

Cell culture experiments. The human colon adenocarcinoma cell line Caco-2 and the human liver hepatocellular carcinoma cell line HepG2 were obtained from the European Collection of Cell Cultures (ECACC, Porton Down, UK). Cells were maintained in Dulbecco's modified Eagle's medium (DMEM) supplemented with 10 % fetal calf serum (FCS) and 1 % penicillin and streptomycin at 37 °C in a humidified atmosphere of 5 % CO_2. Cells were maintained in tissue culture flasks (75 cm^2) as a sub confluent monolayer for propagation. For microscopically analysis of particle uptake, 55000 cells were seeded per 12 well on cover slides. HepG2 cells were grown over night and Caco-2 cells were differentiated for 21 days (medium was changed every 2 to 3 days). Cells were incubated with non-cytotoxic concentrations of fluorescence marked silver nanoparticles (for cell viability analysis see supporting information). After 2, 6, and 24 h cells were washed twice with phosphate buffered saline (PBS), fixated for 10 min with 3.7 % formaldehyde, washed tree times with PBS with Tween, permeabilized with 0.2 % Triton X-100 for 10 min, washed again tree times with PBS, stained with ActinRed 555 Ready Probes Reagent

(Invitrogen), and washed a last time. Samples were analyzed with SP5 confocal fluorescence microscopy from Leica Microsystems.

Acknowledgement

We gratefully thank S. Benemann and D. Hodoroaba for the STEM measurements of the nanoparticles. Additionally we also thank AG Schalley and AG Haag for the possibility to use their spectrofluorometers. A great thanks goes also to H. V. Schröder for productive discussion of the manuscript.

Supporting Information

Supporting Information containing experimental details and cell viability tests are available.

References

1. Nowack, B.; Krug, H. F.; Height, M., 120 Years of Nanosilver History: Implications for Policy Makers. *Environ. Sci. Technol.* **2011,** *45*, 1177-1183.
2. Duncan, T. V., Applications of nanotechnology in food packaging and food safety: Barrier materials, antimicrobials and sensors. *J. Colloid Interface Sci.* **2011,** *363*, 1-24.
3. Wijnhoven, S. W. P.; Peijnenburg, W. J. G. M.; Herberts, C. A.; Hagens, W. I.; Oomen, A. G.; Heugens, E. H. W.; Roszek, B.; Bisschops, J.; Gosens, I.; Van De Meent, D.; Dekkers, S.; De Jong, W. H.; van Zijverden, M.; Sips, A. J. A. M.; Geertsma, R. E., Nano-silver – a review of available data and knowledge gaps in human and environmental risk assessment. *Nanotoxicology* **2009,** *3*, 109-138.
4. Vance, M. E.; Kuiken, T.; Vejerano, E. P.; McGinnis, S. P.; Hochella Jr., M. F.; Rejeski, D.; Hull, M. S., Nanotechnology in the real world: Redeveloping the nanomaterial consumer products inventory. *Beilstein J. Nanotechnol.* **2015,** *6*, 1769-1780.
5. Mehboob, S.; Jacob, J.; May, M.; Kotula, L.; Thiyagarajan, P.; Johnson, M. E.; Fung, L. W. M., Structural analysis of the alpha N-terminal region of erythroid and nonerythroid spectrins by small-angle X-ray scattering. *Biochemistry* **2003,** *42*, 14702-14710.
6. Xiu, Z. M.; Zhang, Q. B.; Puppala, H. L.; Colvin, V. L.; Alvarez, P. J. J., Negligible Particle-Specific Antibacterial Activity of Silver Nanoparticles. *Nano Lett.* **2012,** *12*, 4271-4275.
7. De Matteis, V.; Malvindi, M. A.; Galeone, A.; Brunetti, V.; De Luca, E.; Kote, S.; Kshirsagar, P.; Sabella, S.; Bardi, G.; Pompa, P. P., Negligible particle-specific toxicity mechanism of silver nanoparticles: The role of Ag+ ion release in the cytosol. *Nanomedicine-Nanotechnology Biology and Medicine* **2015,** *11*, 731-739.
8. Haase, A.; Rott, S.; Mantion, A.; Graf, P.; Plendl, J.; Thünemann, A. F.; Meier, W. P.; Taubert, A.; Luch, A.; Reiser, G., Effects of Silver Nanoparticles on Primary Mixed Neural Cell

Cultures: Uptake, Oxidative Stress and Acute Calcium Responses. *Toxicol. Sci.* **2012,** *126*, 457-468.
9. Kim, T.-H.; Kim, M.; Park, H.-S.; Shin, U. S.; Gong, M.-S.; Kim, H.-W., Size-dependent cellular toxicity of silver nanoparticles. *J. Biomed. Mater. Res. A* **2012,** *100A*, 1033-1043.
10. Stefaniak, A. B.; Hackley, V. A.; Roebben, G.; Ehara, K.; Hankin, S.; Postek, M. T.; Lynch, I.; Fu, W.-E.; Linsinger, T. P. J.; Thünemann, A. F., Nanoscale reference materials for environmental, health and safety measurements: needs, gaps and opportunities. *Nanotoxicology* **2013,** *7*, 1325-1337.
11. Henrich-Noack, P.; Prilloff, S.; Voigt, N.; Jin, J.; Hintz, W.; Tomas, J.; Sabel, B. A., In vivo visualisation of nanoparticle entry into central nervous system tissue. *Arch. Toxicol.* **2012,** *86*, 1099-105.
12. Kreyling, W. G.; Abdelmonem, A. M.; Ali, Z.; Alves, F.; Geiser, M.; Haberl, N.; Hartmann, R.; Hirn, S.; de Aberasturi, D. J.; Kantner, K.; Khadem-Saba, G.; Montenegro, J.-M.; Rejman, J.; Rojo, T.; de Larramendi, I. R.; Ufartes, R.; Wenk, A.; Parak, W. J., In vivo integrity of polymer-coated gold nanoparticles. *Nat. Nanotech.* **2015,** *10*, 619-23.
13. Chen, H.; Zou, P.; Connarn, J.; Paholak, H.; Sun, D., Intracellular dissociation of a polymer coating from nanoparticles. *Nano Res.* **2012,** *5*, 815-825.
14. Henriksen-Lacey, M.; Carregal-Romero, S.; Liz-Marzán, L. M., Current Challenges toward In Vitro Cellular Validation of Inorganic Nanoparticles. *Bioconjugate Chem.* **2017,** *28*, 212-221.
15. Kästner, C.; Thünemann, A. F., Catalytic Reduction of 4-Nitrophenol Using Silver Nanoparticles with Adjustable Activity. *Langmuir* **2016,** *32*, 7383-7391.
16. Saha, K.; Agasti, S. S.; Kim, C.; Li, X.; Rotello, V. M., Gold Nanoparticles in Chemical and Biological Sensing. *Chem. Rev.* **2012,** *112*, 2739-2779.
17. Pauw, B. R.; Kästner, C.; Thünemann, A. F., Nanoparticle size distribution quantification: results of a small-angle X-ray scattering inter-laboratory comparison. *J. Appl. Cryst.* **2017,** *50*, 1280-1288.
18. Bressler, I.; Pauw, B. R.; Thünemann, A. F., McSAS: software for the retrieval of model parameter distributions from scattering patterns. *J. Appl. Cryst.* **2015,** *48*, 962-969.
19. Ghosh, D.; Chattopadhyay, N., Gold and silver nanoparticles based superquenching of fluorescence: A review. *J. Lumin.* **2015,** *160*, 223-232.
20. Schindler, T.; Schmiele, M.; Schmutzler, T.; Kassar, T.; Segets, D.; Peukert, W.; Radulescu, A.; Kriele, A.; Gilles, R.; Unruh, T., A Combined SAXS/SANS Study for the in Situ Characterization of Ligand Shells on Small Nanoparticles: The Case of ZnO. *Langmuir* **2015,** *31*, 10130-10136.
21. Liu, X. Q.; Guan, Y. P.; Ma, Z. Y.; Liu, H. Z., Surface modification and characterization of magnetic polymer nanospheres prepared by miniemulsion polymerization. *Langmuir* **2004,** *20*, 10278-10282.
22. Gupta, A. K.; Gupta, M., Synthesis and surface engineering of iron oxide nanoparticles for biomedical applications. *Biomaterials* **2005,** *26*, 3995-4021.
23. Thordarson, P., Determining association constants from titration experiments in supramolecular chemistry. *Chem. Soc. Rev.* **2011,** *40*, 1305-1323.
24. Walkey, C. D.; Chan, W. C. W., Understanding and controlling the interaction of nanomaterials with proteins in a physiological environment. *Chem. Soc. Rev.* **2012,** *41*, 2780-2799.

25. Miclăuş, T.; Bochenkov, V. E.; Ogaki, R.; Howard, K. A.; Sutherland, D. S., Spatial Mapping and Quantification of Soft and Hard Protein Coronas at Silver Nanocubes. *Nano Lett.* **2014,** *14*, 2086-2093.
26. Milani, S.; Baldelli Bombelli, F.; Pitek, A. S.; Dawson, K. A.; Rädler, J., Reversible versus Irreversible Binding of Transferrin to Polystyrene Nanoparticles: Soft and Hard Corona. *ACS Nano* **2012,** *6*, 2532-2541.
27. Kästner, C.; Thünemann, A. F., Catalytic Reduction of 4-Nitrophenol Using Silver Nanoparticles with Adjustable Activity. *Langmuir* **2016,** *32*, 7383-91.
28. Orthaber, D.; Bergmann, A.; Glatter, O., SAXS experiments on absolute scale with Kratky systems using water as a secondary standard. *J. Appl. Cryst.* **2000,** *33*, 218-225.

TOC:

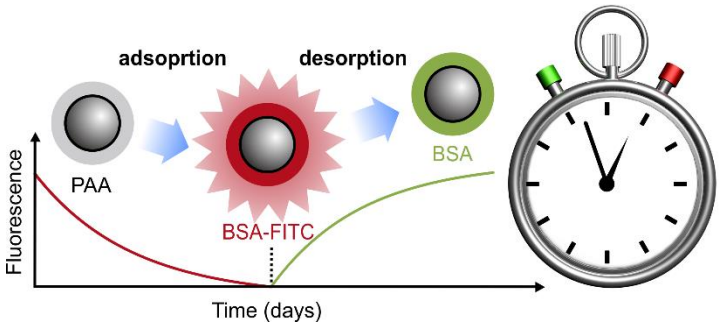
adsoprtion
desorption
PAA
BSA
BSA-FITC
Fluorescence
Time (days)

A.5 Monitoring the fate of small silver nanoparticles during artificial digestion

Claudia Kästner, Dajana Lichtenstein, Alfonso Lampen, Andreas F. Thünemann

Colloids and Surfaces A: Physicochemical and Engineering Aspects **2017**, 526, 76–81.

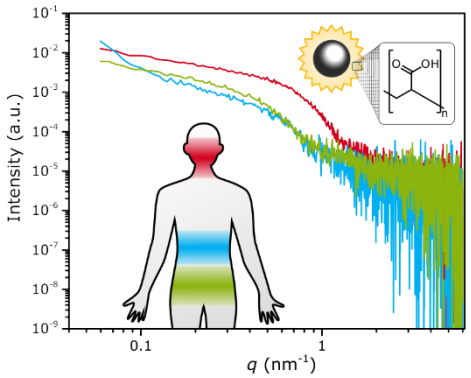

Figure A.2. Graphical abstract.

Submitted on 4 July 2016, first published on 16 August 2016 in Colloids and Surfaces A: Physicochemical and Engineering Aspects.

An electronic version of the article is available (DOI: 10.1016/j.colsurfa.2016.08.013).

A.6 What happens to the silver ions? – Silver thiocyanate nanoparticle formation in an artificial digestion

Claudia Kästner, Alfonso Lampen and Andreas F. Thünemann

Nanoscale **2018**, 10, 3650-3653.

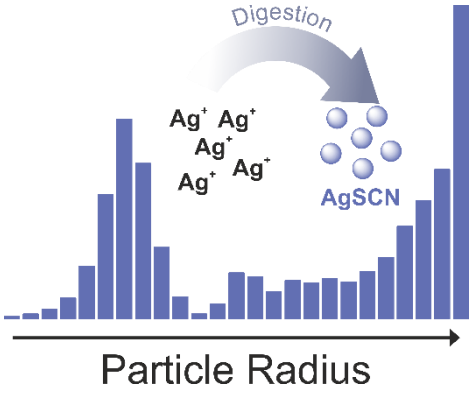

Figure A.3. Graphical abstract.

Submitted on 27 November 2017, first published on 22 January 2018 in Nanoscale.

An electronic version of the article is available (DOI: 10.1039/c7nr08851e).

A.7 Kinetic monitoring of glutathione-induced silver nanoparticle disintegration

Claudia Kästner, Patrick E. J. Saloga and Andreas F. Thünemann

Nanoscale 2018, DOI: 10.1039/c8nr02369g

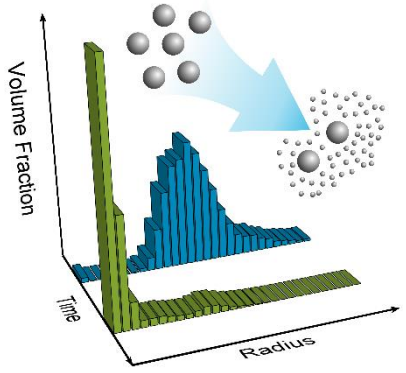

Figure A.4. Graphical abstract.

Submitted on 22 March 2018 to Nanoscale, accepted on 07 May 2018, in publication process.

A.8 Conference Contributions and Awards

Oral Presentations

Claudia Kästner, Andreas Thünemann, **Coating-tuned catalytic activity of silver nanoparticles**, *International summer school "Nanoscience meets Metrology"*, Turin, 2016.

Claudia Kästner, Andreas Thünemann, **Food-dependent aggregation of silver nanoparticles during an artificial digestion**, *Australian Colloid and Interface Symposium 2017*, Coffs Harbour, 2017.

Claudia Kästner, Andreas Thünemann, **Creating the Silver Standard: Development of a Silver Nanoparticle Reference Material using SAXS**, *SAXS Excites - International SAXS Symposium*, Graz, 2017.

Claudia Kästner, Linda Böhmert, Alfonso Lampen, Andreas Thünemann, **What does your gut see? – Silver nanoparticles in an artificial digestion**, *5th Nano Today Conference*, Waikoloa Village, 2017.

Posters

Claudia Kästner, Andreas Thünemann, **The Solution Structure of Essential Proteins in the Presence of Ultra-Small Silver Nanoparticles: Fluorescent Nanosilver**, *SAS 2015 - 16th International Conference on Small Angle Scattering*, Berlin, 2015.

Claudia Kästner, Andreas Thünemann, **Aggregation and deaggregation of silver nanoparticles - what does your gut say?**, *11th International Conference on Biological Barriers*, Saarbrücken, 2016.

Claudia Kästner, Andreas Thünemann, **Artificial Digestion of Colloidal Silver Monitored by Small-Angle X-Ray Scattering**, *6th International Colloids Conference*, Berlin, 2016.

Claudia Kästner, Andreas Thünemann, **Tracking silver nanoparticles: ultra-small silver refunctionalizable with fluorescent biopolymers**, *Polydays 2016*, Potsdam, 2016.

Claudia Kästner, Andreas Thünemann, **Tuning the catalytic activity of silver nanoparticles**, *Australian Colloid and Interface Symposium 2017*, Coffs Harbour, 2017.

Claudia Kästner, Andreas Thünemann, **Highly enhanced catalytic activity of silver**, *5th Nano Today Conference*, Waikoloa Village, 2017.

Awards

Best PhD Student Presentation Award, *International summer school "Nanoscience meets Metrology"*, Turin, 2016.

Nano Today Student Travel Award, *5th Nano Today Conference*, Waikoloa Village, 2017.

A.9 Curriculum Vitae

Der Lebenslauf ist in der Online-Version aus Gründen des Datenschutzes nicht enthalten.

Der Lebenslauf ist in der Online-Version aus Gründen des Datenschutzes nicht enthalten.

A.10 Declaration of Authorship

I hereby declare that the thesis submitted is my own unaided work. All direct or indirect sources used are acknowledged as references. This paper was not previously presented to another examination board and has not been published.

Claudia Kästner